JPL PUBLICATION 81-105

DOE/ER-10614-1
Distribution Category UC-66d, UC-93

Theory and Tests of Two-Phase Turbines

David G. Elliott

March 15, 1982

Prepared for
U.S. Department of Energy
Through an agreement with
National Aeronautics and Space Administration
by
Jet Propulsion Laboratory
California Institute of Technology
Pasadena, California

JPL PUBLICATION 81-105

DOE/ER-10614-1
Distribution Category UC-66d, UC-93

Theory and Tests of Two-Phase Turbines

David G. Elliott

March 15, 1982

Prepared for
U.S. Department of Energy
Through an agreement with
National Aeronautics and Space Administration
by
Jet Propulsion Laboratory
California Institute of Technology
Pasadena, California

Prepared by the Jet Propulsion Laboratory, California Institute of Technology, for the U.S. Department of Energy through an agreement with the National Aeronautics and Space Administration.

ABSTRACT

Two-phase turbines open the possibility of new types of power cycles operating with extremely wet mixtures of steam and water, organic fluids, or immiscible liquids and gases. Possible applications are geothermal power, waste-heat recovery, refrigerant expansion, solar conversion, transportation turbine engines, and engine bottoming cycles.

A theoretical model for two-phase impulse turbines was developed. Apparatus was constructed for testing one- and two-stage turbines (using speed decrease from stage to stage). Turbines were tested with water-and-nitrogen mixtures and Refrigerant 22. Nozzle efficiencies were 0.78 (measured) and 0.72 (theoretical) for water-and-nitrogen mixtures at a water/nitrogen mixture ratio of 68, by mass; and 0.89 (measured) and 0.84 (theoretical) for Refrigerant 22 expanding from 0.02 quality to 0.28 quality. Blade efficiencies (shaft power before windage and bearing loss divided by nozzle jet power) were 0.63 (measured) and 0.71 (theoretical) for water-and-nitrogen mixtures and 0.62 (measured) and 0.63 (theoretical) for Refrigerant 22 with a single-stage turbine, and 0.70 (measured) and 0.85 (theoretical) for water-and-nitrogen mixtures with a two-stage turbine.

ACKNOWLEDGMENT

The two-phase turbine research was supported from May 1977 to September 1980 by the Department of Energy (DOE), Division of Geothermal Energy, Hydrothermal Technology Branch, Clifton B. McFarland, Chief, under Interagency Agreement EG-78-A-30-1026 (NASA Task Order RD 152, Amendment 130), "Analysis Support in Geothermal Cycles and Expanders." The turbine research continued with support from the DOE Division of Advanced Energy Projects, Dr. Ryszard Gajewski, Director, under Interagency Agreement DE-AI01-80ER10614 (NASA Task Order RD 152, Amendment 266), "Two-Phase Turbines for Efficient Waste Recovery."

This report is the final report on the work for the Division of Geothermal Energy and the midterm report on the work for the Division of Advanced Energy Projects.

The turbine research was conducted in the Acoustics, Fluid Dynamics, and Heat Transfer Group (Paul F. Massier, Supervisor) of the Energy and Materials Research Section (Dr. Robert F. Landel, Manager). Support in organizing the project and coordinating with NASA and DOE was provided by G.W. Meisenholder, Manager of Transportation Programs at JPL. Special acknowledgment is due P.R. Miller, Manager of Conservation and Fossil Energy Systems at NASA, for assistance in securing support for the research and handling contractual arrangements.

CONTENTS

Figures

Tables

I. INTRODUCTION

Power conversion using two-phase liquid-gas mixtures has been investigated for use in pumping (Ref. 1), liquid-metal magnetohydrodynamics (Ref. 2), and turbine engines (Ref. 3). This report describes current research on two-phase turbines at JPL.

Two-phase turbines provide a way to operate in the wet region of water-and-steam mixtures or of organic fluids. In addition, two-phase, two-component mixtures such as steam and oil or steam and molten salts can, in principle, be used as working fluids in unusual cycles. Possible applications of two-phase turbines are in geothermal power, waste-heat recovery, refrigerant expansion, solar conversion, transportation turbine engines, and engine bottoming cycles. Potential advantages over conventional vapor cycles in these applications are more effective use of the energy in such hot liquids as geothermal fluids, better matching to sensible-heat sources, lower shaft speeds, and the flexibility of operating without the restriction of dry-vapor expansion.

This report will present theory and test results for two-phase turbines and give examples of applications.

II. BACKGROUND

Earlier, I reported two-phase flow research on jet pumps (Ref. 1) and liquid-metal magnetohydrodynamics (Ref. 2). Those two projects were based on the ability of a two-phase flow to provide pumping without using moving mechanical parts. By expanding a two-phase mixture in a nozzle and then removing the gas phase, a large rise in the dynamic pressure of the fluid can be achieved. The separation of gas from liquid increases the density term ρ in the dynamic pressure $\frac{1}{2}\rho V^2$, enabling the separated liquid to flow through a diffuser to reach a pressure much higher than the inlet pressure of the two-phase nozzle.

Instead of a pressure rise, power can be taken out of the liquid. This effect is the basis of liquid-metal magnetohydrodynamics, or liquid-metal MHD. A liquid metal is circulated in a closed loop, and power is extracted from the liquid metal with a magnetic field. Liquid-metal MHD has been studied at the Jet Propulsion Laboratory (JPL), the Argonne National Laboratory, and elsewhere. Because of the efficiency limitations of two-phase nozzles, separators, diffusers, and generators, liquid-metal MHD cycles have been limited to about half the efficiency of turbine cycles, and applications appear limited to extreme temperature conditions where turbines cannot be used.

During the JPL liquid-metal MHD project in 1973, I suggested, not seriously, that the MHD generator could be replaced by a two-phase liquid-metal turbine to raise the efficiency of the liquid-metal MHD cycle. Lance Hays, an engineer on the project, recognized in this suggestion the germ of a serious possibility and pointed out that a two-phase turbine, coupled with a pump to return the liquid to the nozzle, could use two-phase mixtures other than liquid metals, such mixtures as steam and hydraulic oil, to provide a new type of turbine engine with low shaft speed and other possible advantages.

At the same time, A.L. Austin and his geothermal group at Lawrence Livermore Laboratory (LLL) proposed a two-phase turbine for geothermal power (Ref. 4). The two-phase fluid from geothermal wells (both the water and the steam) would be passed through the turbine. The LLL group pursued this idea experimentally in research on two-phase impulse turbines (Ref. 5). They

hoped that the water drop sizes would be small enough for the steam and water to behave as a homogeneous fluid and give these turbines efficiencies comparable to those of vapor turbines.

Based on calculations of drop sizes and drop trajectories, I concluded that the liquid drops in two-phase turbines would be too large to follow the gas phase, and that the liquid would impinge on the blades and form a thin liquid film. The friction drag of this film would be so high that the efficiency of single-stage impulse turbines would be limited to little more than 50 percent.

To achieve higher efficiency, Hays and I thought it would be necessary to use a "separator turbine" in which the liquid would be separated from the vapor in a rotary separator and then passed through a liquid turbine. This concept was subsequently pursued by Hays' company, Biphase Energy Systems, in seeking to develop commercial applications (Refs. 6 and 7).

In early turbine experiments at JPL during 1978, I studied the flow of water-and-nitrogen mixtures in rotary separators and concluded that the impact and other losses in rotary separators would limit turbine efficiency as severely as the liquid friction in bladed turbines. At the same time, LLL furnished JPL a surplus steam turbine for bladed turbine tests. The second row of blades was cut away to make a single-stage rotor. In water-and-nitrogen tests, this rotor gave as high an efficiency as seemed attainable with a separator turbine. In addition, I found it possible to further improve the efficiency by using two stages, with high speed in the first stage and a lower speed in the second stage. This two-phase turbine is the type discussed in this report.

It is also possible to achieve efficient two-phase expansion using positive-displacement expanders. Helical-screw (Lysholm) expanders have been tested by LLL (Ref. 8) using a two-phase steam-and-water flow, and by Hydrothermal Power Company in cooperation with JPL (Ref. 9). Efficiencies as high as 60 percent have been achieved in geothermal field tests at 500-kW output power (Ref. 9).

III. APPLICATIONS

A. Saturated Water Turbines

One of the simplest applications of two-phase turbines is the open-cycle expansion of saturated water or low-quality steam ("quality" is the steam fraction by mass). An example is the expansion of fluid from a geothermal well.

Figure 1 shows steam-and-water expansion on a temperature-entropy (T-S) diagram. The expansion starts on or near the saturated liquid line and proceeds downward to the steam condenser pressure. This is the process proposed as the "total-flow" concept by LLL (Refs. 4 and 5).

An alternative approach for geothermal use is to replace with two-phase turbines the throttling steps used to provide steam in the conventional geothermal cycle. The output from the two-phase turbines adds to the output of the steam turbines. Hays and Cerini (Refs. 6 and 7) have developed such geothermal expanders, combining flash vaporization, separation, and power output in a single unit.

B. Organic-Fluid Turbines

One of the most promising applications of two-phase turbines is in closed-cycle engines using organic working fluids. The advantages over Rankine vapor cycles are better matching to the cooling curve of sensible-heat sources and elimination of the boiler. Possible applications are geothermal closed-cycle (binary) power plants, engine exhaust heat recovery, industrial waste-heat recovery, and bottoming cycles for steam and gas turbine plants.

Figure 2 shows the equipment arrangement in an organic-fluid two-phase turbine engine. The fluid to be cooled (the "source fluid"), such as geothermal hot water or engine exhaust, flows through the heat exchanger from A to B and is cooled by counterflow heat transfer to the organic working fluid. The working fluid is heated to saturation temperature. The saturated

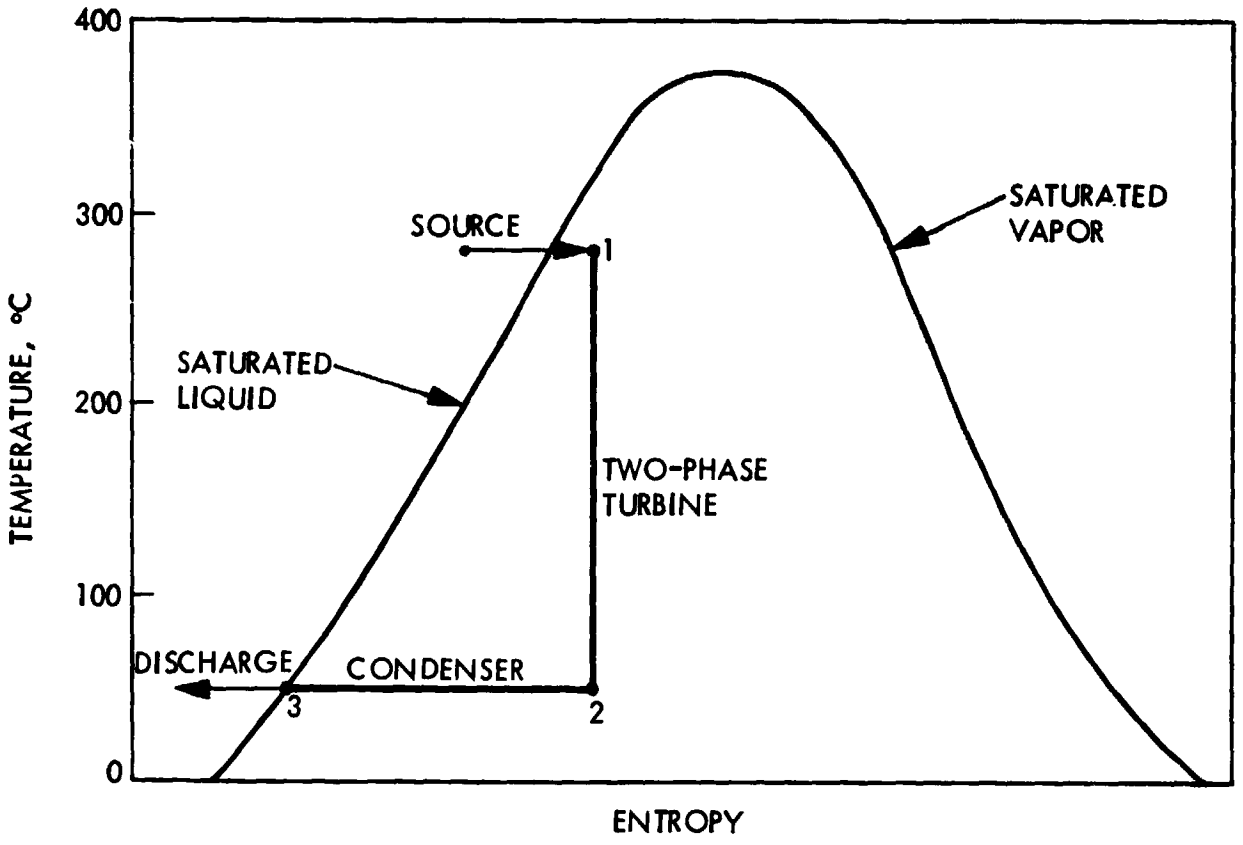

Fig. 1. Steam-and-water cycle

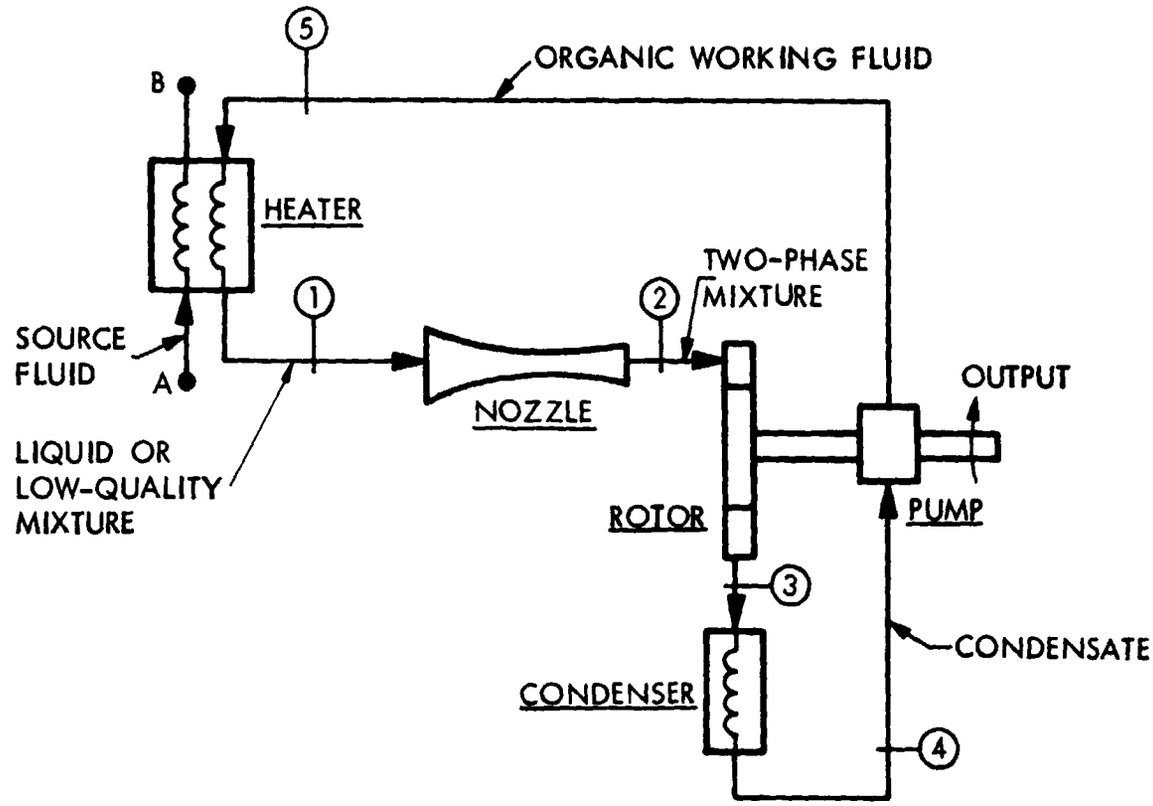

Fig. 2. Organic-fluid two-phase turbine

liquid, with possibly a small amount of vapor, flows to a two-phase nozzle. The liquid expands, partially vaporizes, and accelerates in the nozzle. The two-phase mixture drives the turbine rotor. The vapor is condensed, and the condensate is pumped back to the heater by a pump on the turbine shaft.

The cycle is shown on a T-S diagram in Fig. 3. The state points are numbered to correspond with Fig. 2. The two-phase nozzle expansion takes the fluid from a saturated liquid at 150°C (point 1) to a two-phase flow of 0.6 quality at 40°C (point 2). The flow is decelerated in the rotor, condensed to point 4, and pumped back to nozzle inlet pressure at point 5. The liquid is then reheated by the source fluid to point 1.

The feature of this cycle that makes it ideal for recovery of energy from a sensible-heat source is the straight-line heating of the working fluid from point 5 to point 1 over the full temperature range of the cycle. The heating curve of the working fluid matches the cooling curve of the source fluid. The temperature difference between the source fluid and the working fluid can be kept small at all points in the heat exchanger. By contrast, the heating curve of a Rankine cycle, in which the working fluid must be boiled to dry vapor, is a poor match to the source-fluid cooling curve. Large differences are necessary between the source-fluid temperature and working-fluid temperature over portions of the heat exchanger, and it may not be possible to cool the source fluid all the way to ambient temperature; both effects reduce the available work.

The appropriate efficiency for comparison of waste-heat cycles is the "utilization efficiency," defined as the ratio of power output to heat available. The heat available is the heat that could be extracted by cooling the source fluid all the way to the low-temperature limit set by ambient temperature or other external limitations. If T_C is this low-temperature cooling limit, then the available heat is

$$Q_A = \dot{m} c_p (T_A - T_C) \qquad (1)$$

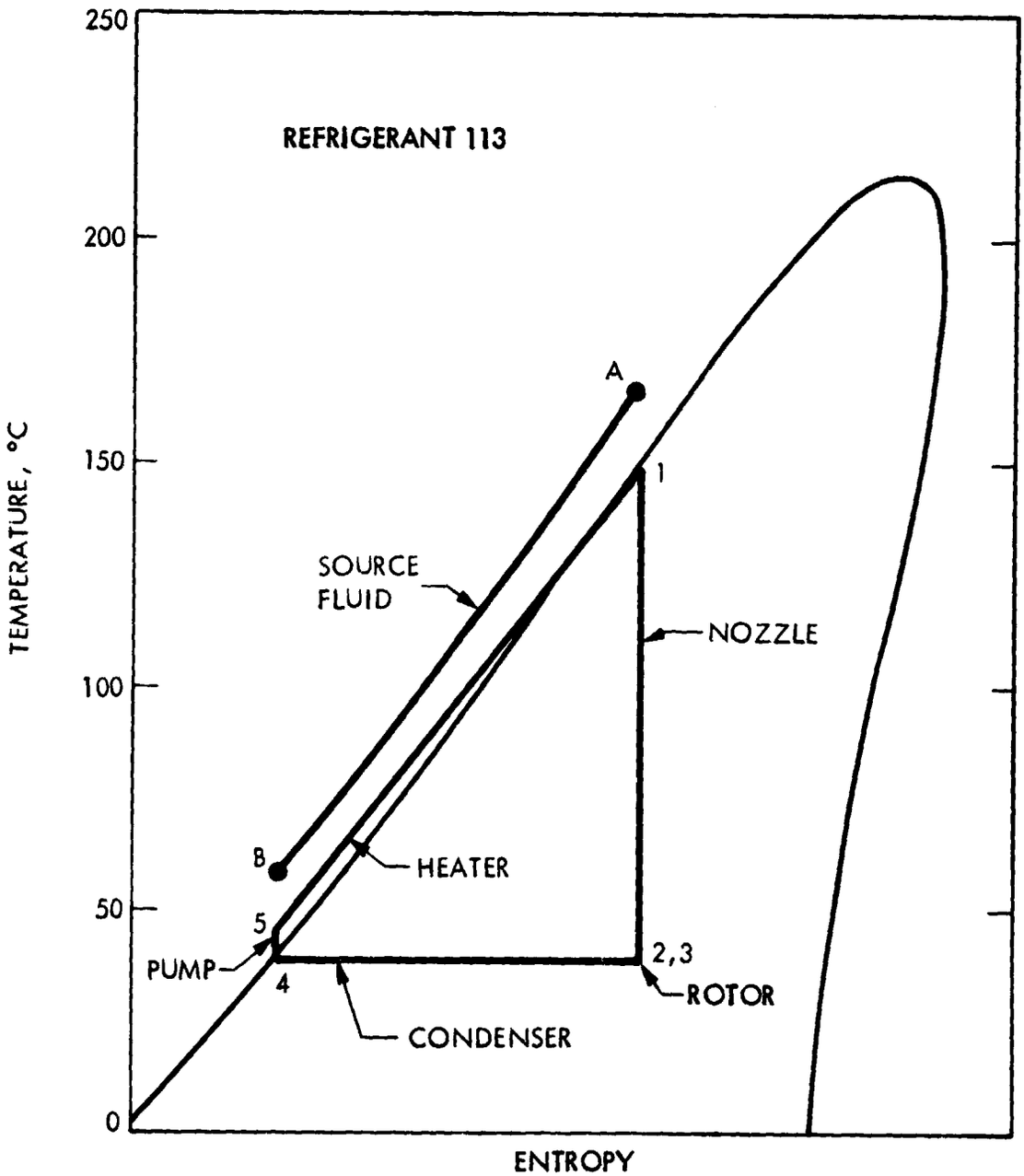

Fig. 3. Organic-fluid two-phase cycle

and the utilization efficiency is

$$\eta_u = \frac{P}{\dot{m}c_p(T_A - T_C)} \tag{2}$$

where P is the power output, and $\dot{m}$ is the flow rate, c_p the specific heat, and T_A the initial temperature of the source fluid.

If, due to cycle limitations, the gas is cooled only part way to the cooling limit and leaves at a temperature T_B higher than T_C, then the heat input to the cycle is $\dot{m}c_p(T_A - T_B)$ and the cycle efficiency, as conventionally defined, is

$$\eta = \frac{P}{\dot{m}c_p(T_A - T_B)} \tag{3}$$

From Eqs. (2) and (3), it can be seen that the utilization efficiency is the cycle efficiency multiplied by the ratio of actual to available source-fluid temperature drop.

$$\eta_u = \eta \frac{T_A - T_B}{T_A - T_C} \tag{4}$$

In Fig. 4, the utilization efficiencies of two-phase and Rankine cycles are compared for the case in which the cooling limit is the same as the condensing, or rejection, temperature $T_R = 38^{\circ}C$, and the turbine and pump efficiencies are 100 percent. The two-phase cycle is 50 percent more efficient than the Rankine cycle for source fluid temperatures of 150 to $200^{\circ}C$. The utilization efficiency of the two-phase cycle is close to the limiting efficiency W_A/Q_A corresponding to the available work W_A given by integration of the Carnot efficiency between T_A and T_R.

In an effort to better match the working fluid heating curve to the source fluid cooling curve, some geothermal studies have proposed supercritical Rankine cycles. Figure 5(a) shows such a cycle using isobutane as

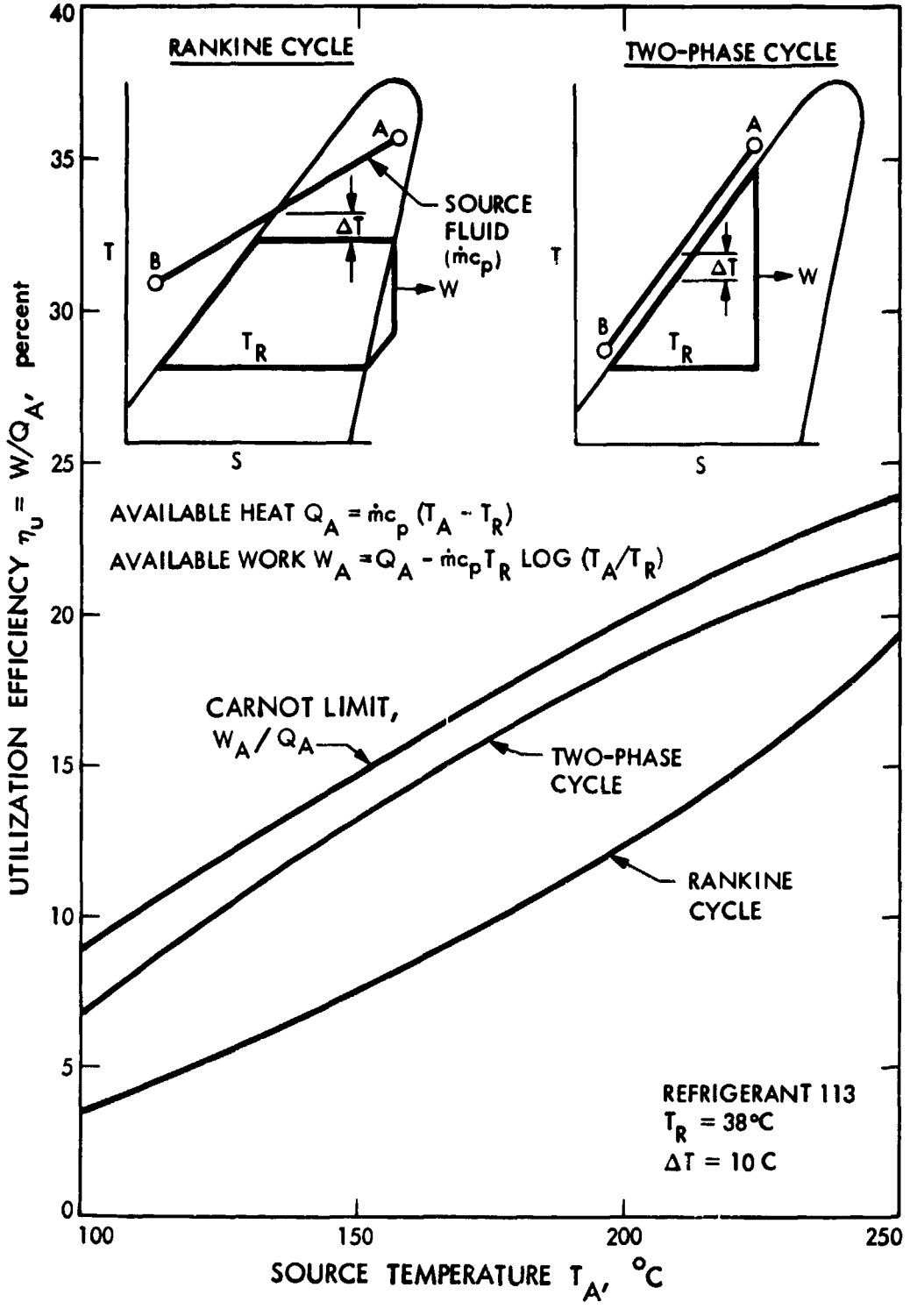

Fig. 4. Comparison of Rankine and two-phase cycles

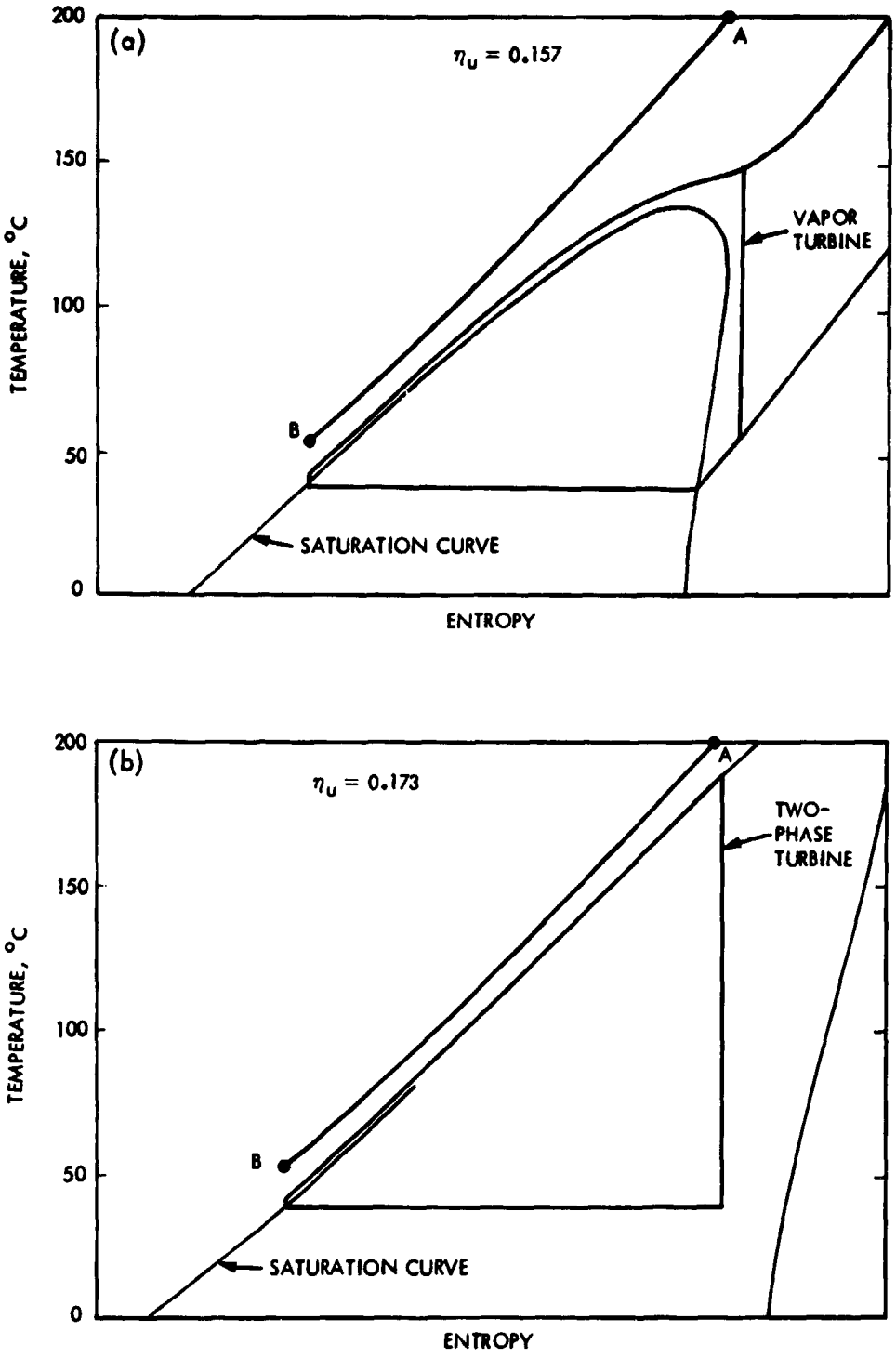

Fig. 5. Comparison of supercritical and two-phase cycles: (a) supercritical cycle (isobutane); (b) two-phase cycle (Refrigerant 113)

the working fluid. The utilization efficiency, with $T_C = T_R = 38^{\circ}C$ and 100-percent turbine and pump efficiencies, is 0.157. A two-phase cycle using Refrigerant 113, Fig. 5(b), has a utilization efficiency of 0.173, a 10-percent gain.

At higher source-fluid temperatures, water could be used as the working fluid. The main problem with water in a two-phase turbine is the large steam volume and high velocity at low exhaust pressures. Figure 6 shows how water could be used at high pressure by expanding only to $150^{\circ}C$ in the two-phase cycle and using an organic bottoming cycle for the remainder of the temperature drop. In this way a good temperature match between the working fluid and the source fluid could be maintained at a source-fluid temperature as high as $350^{\circ}C$.

Another application of two-phase organic turbines is in refrigeration. Instead of throttling a refrigerant to produce cold liquid, the refrigerant could be expanded in a two-phase turbine. The work conventionally lost in the irreversible throttling process would be recovered as shaft power. The shaft power could assist in driving the compressor. The electricity consumption for refrigeration would be reduced by about 10 percent.

C. Wet-to-Dry Cycle

If the initial temperature of the working fluid is sufficiently high and the saturated vapor line has a positive slope on a T-S diagram (a "drying" fluid), the working fluid could be expanded all the way to dry vapor. This phenomenon opens up the possibility of a two-phase cycle that has two-phase flow in the nozzle but not in the rotor. Such a cycle will be called a "wet-to-dry" or WD cycle.

Figure 7 is a T-S diagram of a WD cycle using toluene. The toluene is expanded from saturated liquid at $290^{\circ}C$ (point 1) to saturated vapor at $66^{\circ}C$ (point 2). The vapor drives an impulse rotor and leaves the rotor slightly superheated at point 3. The vapor is condensed to point 4 and pumped back to the nozzle inlet pressure at point 5. There is again an ideal match to the cooling curve of the source fluid, but two-phase rotor flow is not

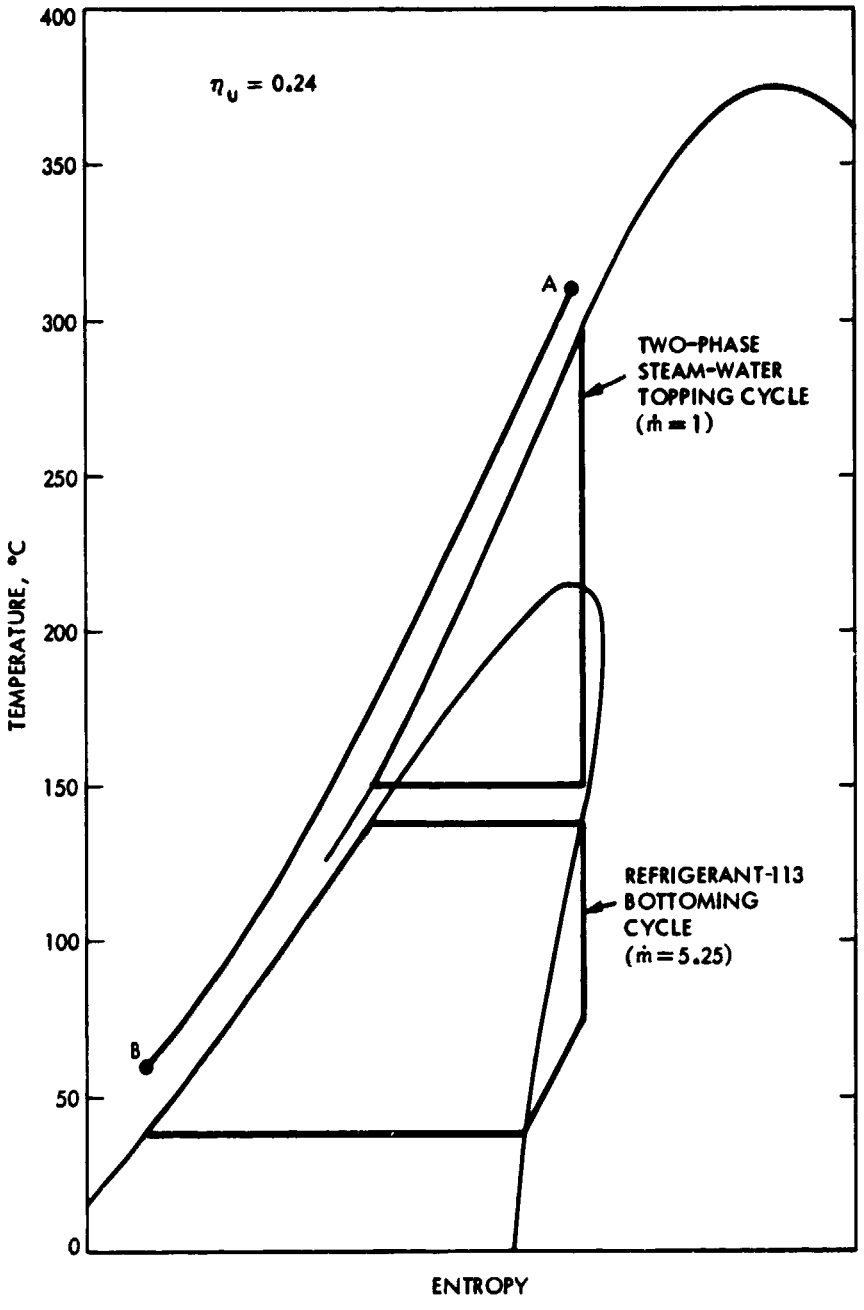

Fig. 6. Steam topping cycle with organic-fluid bottoming cycle

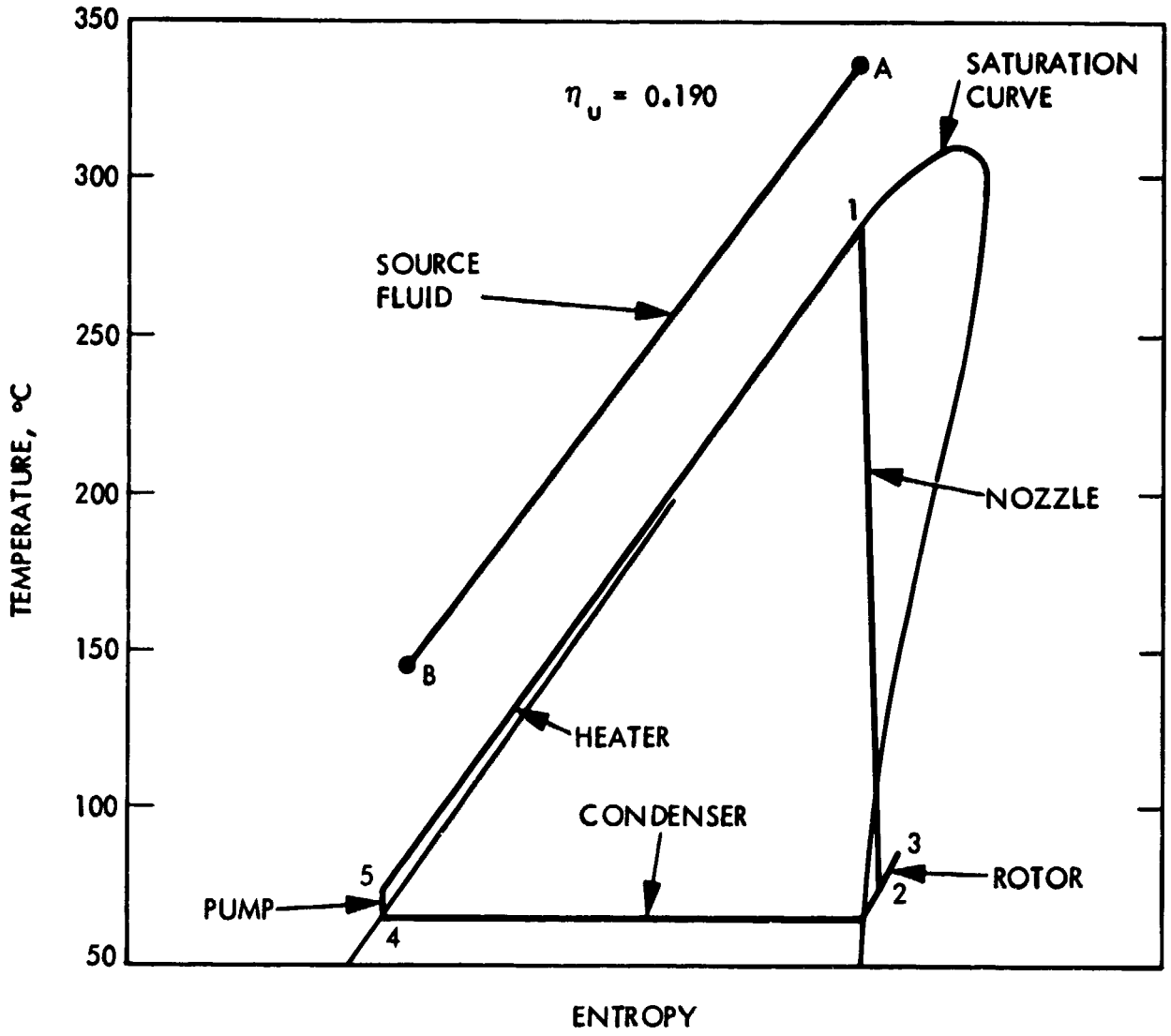

Fig. 7. Wet-to-dry cycle

required. The utilization efficiency for the cycle of Fig. 7 is 0.19 whereas the utilization efficiency of the best toluene Rankine cycle using the same source fluid, and having the same turbine efficiency, would be only 0.14.

D. Two-Component Cycle

Two-phase mixtures in which the vapor and liquid are different chemical compounds are called "two-component" mixtures. An example is steam mixed with an organic liquid or a molten salt. Such mixtures behave quite differently from the one-component mixtures discussed to this point.

Figure 8 shows the equipment arrangement for a two-phase, two-component engine, and Fig. 9 is a T-S diagram for the component that forms the vapor phase, in this case steam. The liquid phase is a molten salt such as lithium carbonate or sodium hydroxide (it is not known if these liquids would actually be compatible with steam). The ratio of liquid to vapor is 30, by mass.

The steam and liquid mixture expands from the nozzle inlet, point 1, to the steam condenser pressure at point 2. Because of the large ratio of liquid to steam, the mixture expands almost isothermally and the nozzle exit velocity is much lower than it would be for steam alone. The two-phase mixture drives the turbine rotor. The steam is separated from the liquid, cooled to saturation temperature in a regenerative heat exchanger (point 4) condensed to point 5, pumped back to the nozzle inlet pressure at point 6, and heated to point 7 in the regenerative heat exchanger. The liquid leaving the turbine is pumped to the heater by a pump on the turbine shaft. The heated liquid is mixed with the condensate (water) in the mixer, and the water is vaporized by direct-contact heat transfer.

Possible applications of this cycle are in turbine engines for solar power or transportation. The advantage of the two-phase, two-component cycle for these applications is the ability to achieve a low shaft speed in a small turbine engine. A steam turbine of 150-kW shaft power, for example, using the temperatures given in Fig. 9, would have a speed of about 60,000 rpm. The two-phase turbine would operate at only about 10,000 rpm. There is also an efficiency advantage. At the Fig. 9 temperatures, a steam Rankine cycle would

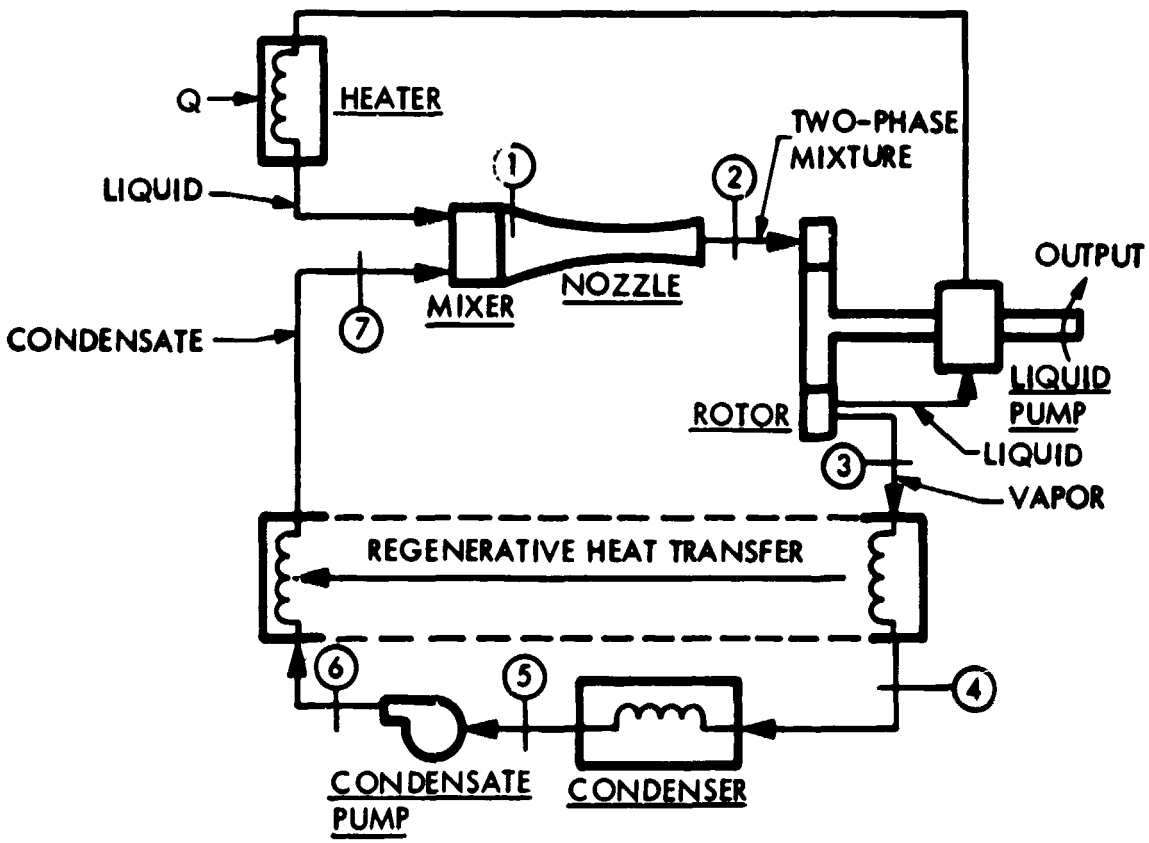

Fig. 8. Two-phase, two-component engine

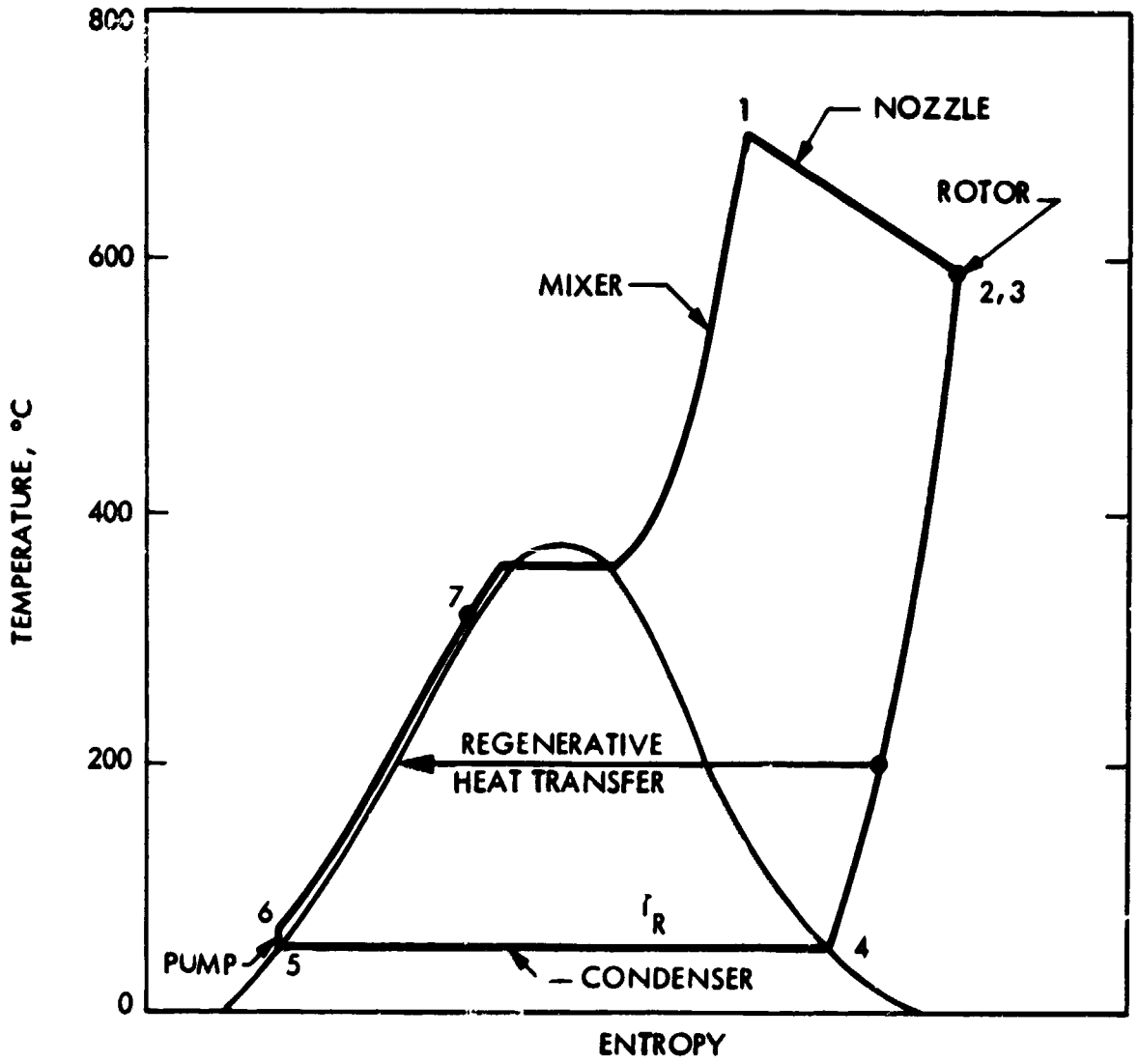

Fig. 9. Two-phase, two-component cycle

have an efficiency of about 0.28, whereas the two-phase cycle would have an efficiency of about 0.37 (for the same turbine efficiency), because the steam is continuously reheated in the two-phase nozzle. In addition, the two-phase cycle allows control of turbine speed because the mixture ratio can be varied to change the nozzle exit velocity, a capability unavailable in steam turbines.

IV. NOZZLES

A. Construction

The nozzle converts the heat energy of the two-phase mixture to the kinetic energy of a jet. The gas is accelerated by pressure, and the liquid is partly accelerated by pressure, but mainly by drag. The gas moves faster than the liquid to produce the drag. The velocity difference, or "slip", also causes breakup of the liquid into small drops.

The nozzle design used in the turbine tests is shown in Figs. 10 and 11. The liquid enters the inlet fitting, flows around a baffle, and enters a hexagonal array of 61 tubes of 6.35-mm outside diameter and 4.57-mm inside diameter. The tubes are aimed toward the nozzle throat. The tubes are clamped together at their exits by a tube cage and are held 1.4 mm apart at the inlets by a tube sheet. The liquid enters the nozzle through the tubes at a velocity of about 4 m/s.

The gas enters the mixer housing, flows through openings in the tube cage, enters the spaces between the liquid-injection tubes, and flows into the nozzle through the cusp-shaped gaps between the tube exits. The gas enters at about 30 m/s.

The multiple injection tubes and gas orifices provide a uniform distribution of flow rate and mixture ratio across the nozzle inlet. Where the inlet flow is saturated liquid, the multiple jets also provide an initial separation of the liquid streams so that vapor forms uniformly across the nozzle; a small amount of vapor is fed to the gas inlet to give a starting quality of 1 to 2 percent.

The nozzle has a converging-diverging shape. The inlet section has a 10-deg wall angle and the exit section a 2.5-deg angle. The throat section has a very gradual area change with distance to minimize slip.

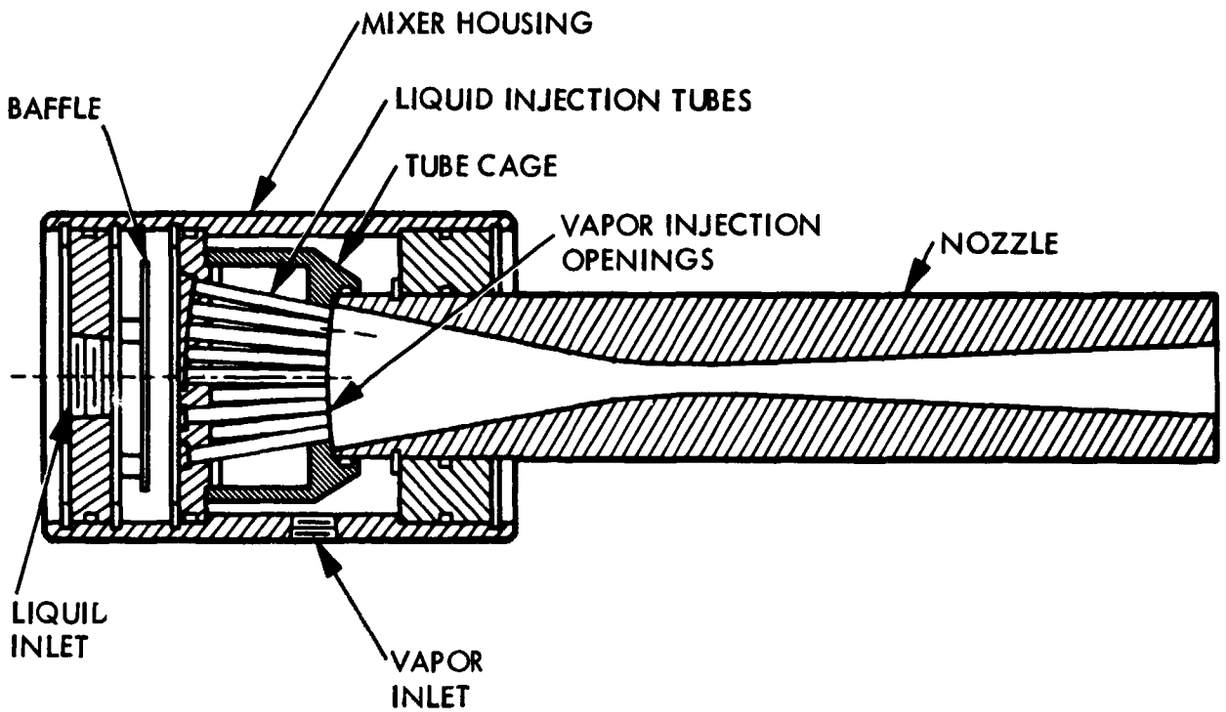

Fig. 10. Two-phase nozzle

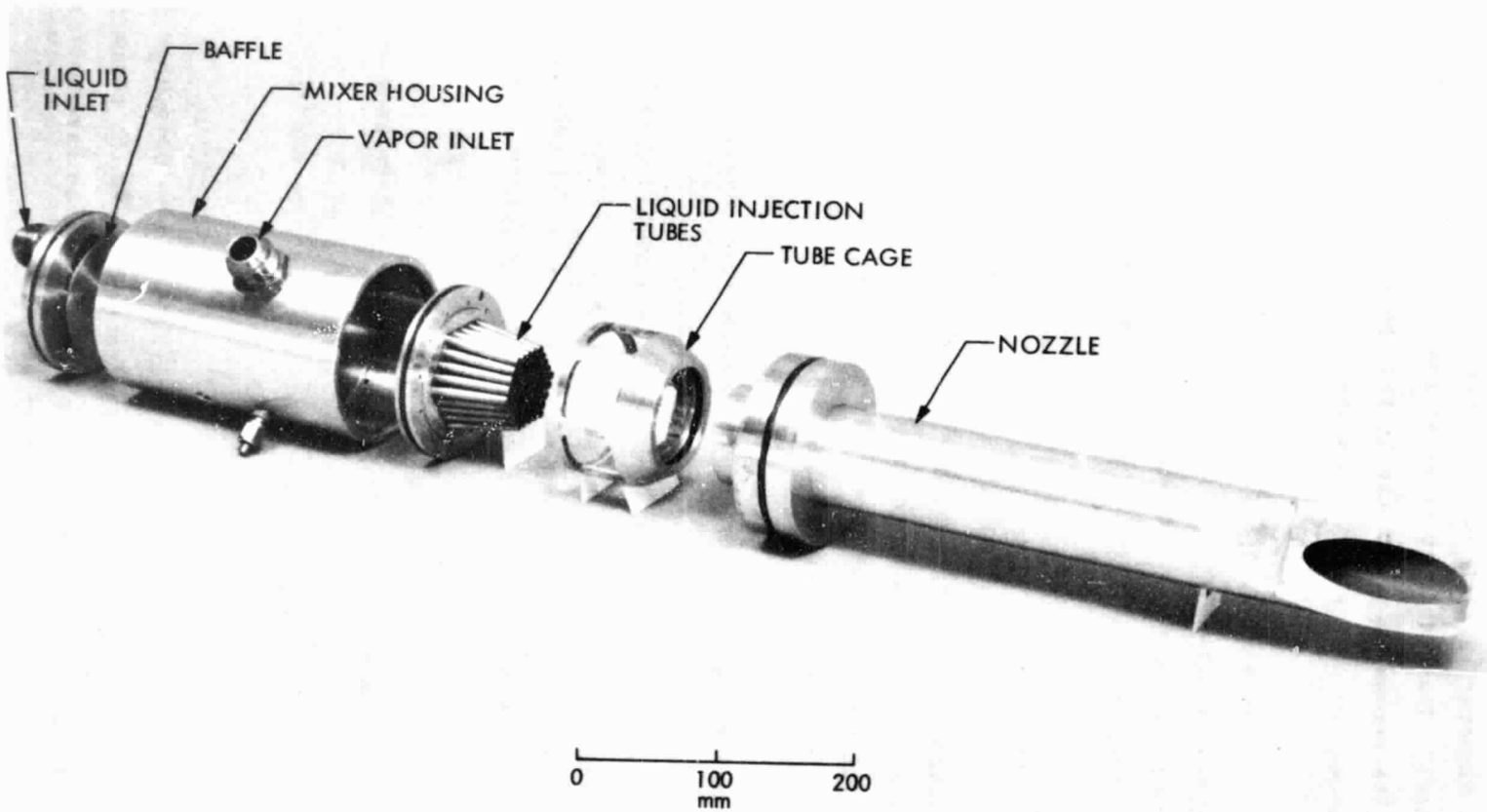

Fig. 11. Experimental two-phase nozzle

The nozzle is designed for operation with Refrigerant 22 expanding from saturated liquid conditions at 20°C and 0.9 MPa to atmospheric pressure. The throat diameter is 13.1 mm. The exit is cut off at a 20-deg angle for turbine tests. The nozzle diameter at the upstream end of the exit ellipse is 27.6 mm. The expansion area ratio to that point is 4.4, the value calculated to be required for expansion to atmospheric pressure.

The nozzle is also used for water-and-nitrogen tests with expansion from 2.0 MPa to atmospheric pressure. Figure 12 is a 1-μs flash photograph of the water-and-nitrogen jet leaving the nozzle. The velocity is 80 m/s. Faint striations from the liquid injection tubes are still visible in the jet.

B. Nozzle Program

Reference 10 presents the theory for two-phase nozzle flow. The theory is incorporated in two computer programs, one for single-component flow and the other for two-component flow. The programs, test cases, and operating instructions are available from JPL.

To use the computer program, the nozzle inlet conditions are specified (pressure, temperature, flow rate, and velocity). The variation of pressure with distance and the fluid properties are entered in tabular form. The program calculates the liquid and gas flow rates, liquid and gas velocities, nozzle area, and other quantities at successive, small pressure steps. The results are printed at the exit pressure and any desired intermediate pressures.

To match a given nozzle shape, rather than a given pressure profile, the specified pressure profile can be modified in two or three successive computer runs to make the calculated area variation agree with the desired nozzle contour.

The liquid drop diameter is calculated from a Weber number criterion. The Weber number is proportional to the ratio between the pressure force tending to break up the drops and the surface tension force holding the drops together. The Weber number is defined as

ORIGINAL PAGE
BLACK AND WHITE PHOTOGRAPH

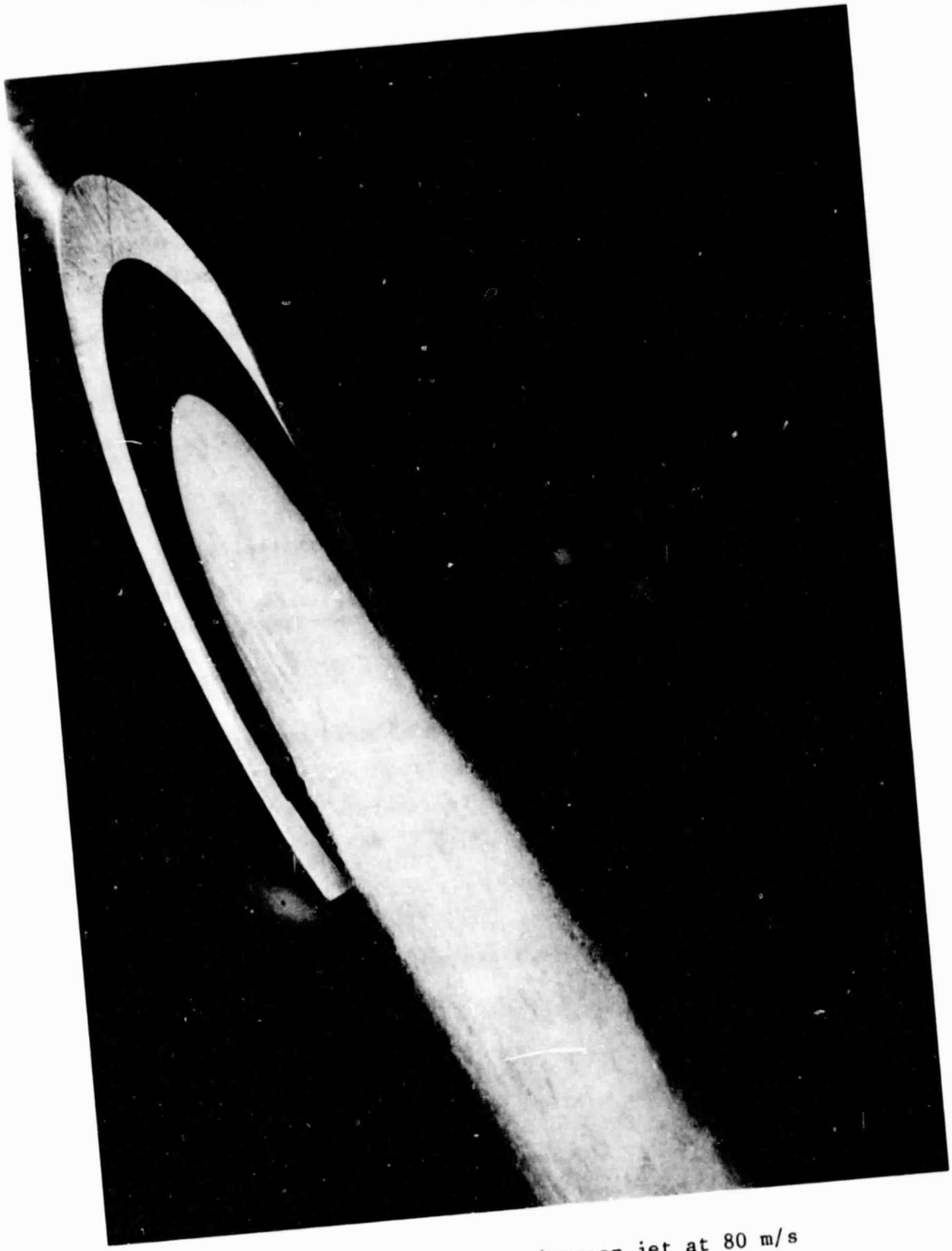

Fig. 12. Water-and-nitrogen jet at 80 m/s

$$We = \frac{\rho_g (V_g - V_\ell)^2 D}{2\sigma} \tag{5}$$

where ρ_g is the gas density, V_g is the gas velocity, V_ℓ is the liquid velocity, D is the drop diameter, and σ is the surface tension.

Based on the drop breakup data reviewed in Ref. 10, the maximum stable drop diameter is the diameter for which the Weber number is 6. From Eq. (5), the corresponding maximum drop diameter is

$$D_{max} = \frac{12\sigma}{\rho_g (V_g - V_\ell)^2} \tag{6}$$

In the nozzle program, the drop diameter D is initially set to a large value, and the diameter is reduced to D_{max} whenever D_{max} falls below D. Typically, breakup takes place over a short distance immediately upstream of the throat.

In the one-component nozzle program, the liquid and vapor are both assumed to have a temperature equal to the saturation temperature at the local pressure. In the two-component program, the temperature difference is calculated from drop heat transfer relations.

Wall friction is calculated using nozzle friction relations for single-phase flow evaluated at the two-phase mixture density.

C. Performance Definitions

In a two-phase nozzle, the mixture ratio R is defined as the ratio of liquid mass flow rate $\dot{m}_\ell$ to gas flow range $\dot{m}_g$.

$$R = \frac{\dot{m}_\ell}{\dot{m}_g} \tag{7}$$

The quality x is the ratio of gas flow rate to total flow rate

$$x = \frac{\dot{m}_g}{\dot{m}_t} = \frac{1}{1 + R} \tag{8}$$

where $\dot{m}_t$ is the total flow rate $\dot{m}_\ell + \dot{m}_g$.

The maximum velocity thermodynamically possible for expansion from the inlet conditions to the exit pressure is the isentropic velocity V_i. The mass weighted mean velocity of the actual flow with differing liquid and gas velocities is

$$\bar{V} = \frac{\dot{m}_\ell V_\ell + \dot{m}_g V_g}{\dot{m}_t} \tag{9}$$

where V_ℓ is the liquid velocity and V_g is the gas velocity. The mean velocity $\bar{V}$ is also equal to the jet momentum per unit mass.

In this report, $\bar{V}$ will be used for the mean velocity with wall friction included, and $\bar{V}_0$ will be used for the mean velocity without wall friction.*

The thrust of a two phase nozzle, by the definition of $\bar{V}$, is

$$F = \dot{m}_t \bar{V} \tag{10}$$

Equation (10) is used to calculate the experimental value of the mean jet velocity $\bar{V}$; the thrust and flow rates are measured, and the thrust is divided by the total flow rate to give $\bar{V}$.

---

* In Ref. 10, $\bar{V}$ and $\bar{V}_0$ are denoted $\bar{V}_\delta$ and $\bar{V}$, respectively.

The velocity coefficient of a nozzle is the ratio of mean velocity to isentropic velocity

$$K_v = \frac{\bar{V}}{V_i} \tag{11}$$

The kinetic power in the jet is

$$P_{jet} = \tfrac{1}{2}(\dot{m}_\ell V_\ell^2 + \dot{m}_g V_g^2) \tag{12}$$

The isentropic jet power is

$$P_i = \tfrac{1}{2}\dot{m}_t V_i^2 \tag{13}$$

The nozzle efficiency is

$$\eta_n = \frac{P_{jet}}{P_i} \tag{14}$$

D. LLL Steam-and-Water Data

T. W. Alger at LLL measured velocities for steam-and-water nozzles, and the results are presented in Ref. 11. Nozzle 2 of Ref. 11 will be analyzed here. Nozzle 2 had a throat diameter of 6.4 mm, an exit diameter of 31.8 mm, a diverging length of 60.5 mm, and a divergence half-angle of 12 deg. The convergence half-angle was 45 deg and the throat had a sharp corner. In nozzle tests at an inlet pressure of 2.41 MPa, an inlet quality of 0.129, and an exit pressure of 30 kPa, the measured velocity coefficient K_v was between 0.90 and 0.95 (Fig. 10 of Ref. 11).

In Ref. 12 Alger presents measurements of drop diameters for steam-and-water nozzles. He used a light-scattering technique. The nozzles had thin rectangular cross sections with side-wall contours similar to the nozzles of Ref. 11, but the inlet pressure was reduced to 1.0 MPa and the exit pressure

to 20 kPa to provide greater jet transparency. The measured mass-median drop diameter (which is about the right diameter to use for nozzle performance calculations) was found to be about 2.4 μm (Ref. 12, p. 107).

Using the measured pressure profile for Nozzle 2 from Fig. 7 of Ref. 11 as input, Fig. 13 compares the data from Refs. 11 and 12 with predictions of the JPL nozzle program. The nozzle program, using Eq. (6) to calculate the drop diameter, predicts that the drops will break up to a 5.5-μm diameter. The highest measured velocity coefficient of 0.95 corresponds to a drop diameter of 2.8 μm, in good agreement with the measured drop diameter of 2.4 μm from Ref. 12. Thus the drop diameter predicted by the nozzle program is perhaps as much as a factor of 2 too large.

E. Water-and-Nitrogen Data

Figure 14 compares the theoretical and experimental exit velocities for water-and-nitrogen flow in the nozzle of Fig. 11. The theoretical mean velocity $\bar{V}$ is 4 percent below the measured velocities, again indicating overestimation of drop size in the program.

The comparison given in Table 1 is at the mixture ratio of 68 used in the turbine tests. The column headed "Fitted" shows the program results fitted to the measured data to give the best estimates of the quantities that could not be measured.

The actual throat area is 9 percent higher than the throat area calculated by the nozzle program; this means that the measured flow rate is 9 percent below theoretical for a given throat area. During expansion, the water has a slight reduction in flow rate to 3.603 kg/s because of evaporation, and the flow rate of the gas phase increases correspondingly.

The theoretical velocity ratio of gas to liquid is 1.46. It is reasonable to assume that the velocity ratio in the experimental nozzle is the same. The "fitted" velocities that have that ratio and agree with the measured mean velocity $\bar{V}$ of 94.3 m/s are V_ℓ = 93.7 m/s and V_g = 137.0 m/s. The fitted nozzle efficiency is 0.782, which is 8 percent higher than that predicted by the nozzle program.

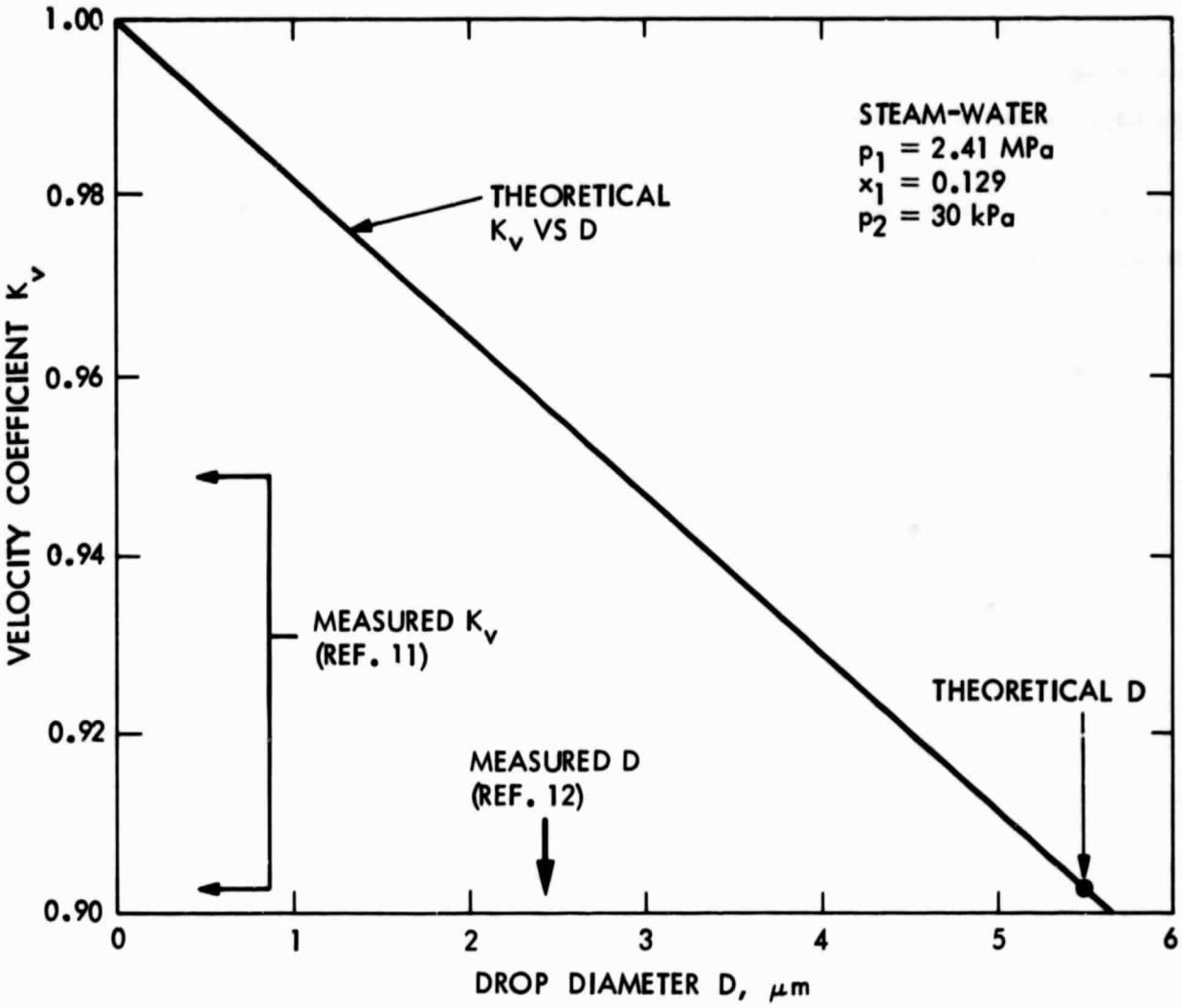

Fig. 13. Comparison of theoretical and experimental drop diameters and velocity coefficients for the LLL steam-and-water nozzle

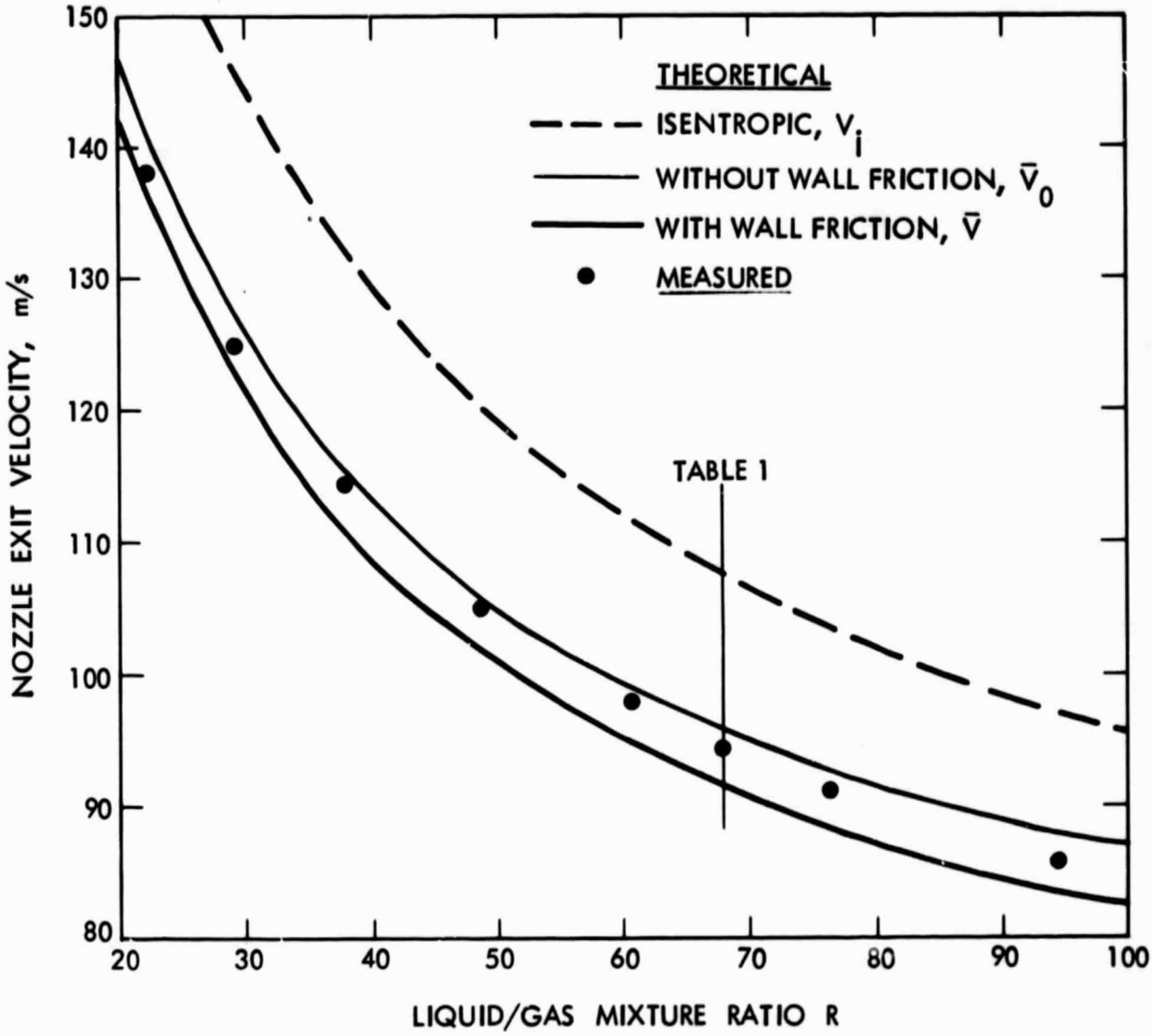

Fig. 14. Comparison of theoretical and experimental exit velocities

Table 1. Comparison of theoretical and experimental nozzle performance using water and nitrogen

Item	Value		
	Measured	Nozzle program	Fitted
Inlet			
Temperature, T_1, ^{o}C	22	22	
Pressure, p_1, kPa	2000	2000	
Total flow rate, $\dot{m}_t$, kg/s	3.657	3.657	
Liquid (water) flow rate, $\dot{m}_\ell$, kg/s	3.604	3.604	
Gas (nitrogen) flow rate, $\dot{m}_g$, kg/s	0.053	0.053	
Mixture ratio, R	68.0	68.0	
Velocity, V_1, m/s	3.6	3.6	
Throat			
Pressure, p_t, kPa		920	
Mean velocity, $\bar{V}_t$, m/s		57.8	
Area, A_t, mm^2	135	124	
Exit			
Pressure, p_2, kPa	98.6	98.6	
Liquid temperature, T_ℓ, ^{o}C		21.3	
Gas temperature, T_g, ^{o}C		15.3	
Drop diameter, d_2, μm		130	
Area, A_2, mm^2	597	403	
Liquid flow rate, $\dot{m}_\ell$, kg/s		3.603	3.603
Gas flow rate, $\dot{m}_g$, kg/s		3.054	0.054
Mixture ratio R_2		66.7	

Table 1 (contd)

Item	Value		
	Measured	Nozzle program	Fitted
Mean free-stream velocity, $\bar{V}_0$, m/s		95.1	
Mean velocity, $\bar{V}$, m/s	94.3	90.5	94.3
Liquid velocity, V_ℓ, m/s		89.9	93.7
Gas velocity, V_g, m/s		131.5	137.0
Jet power, P_{jet}, kW		15.03	16.32
Isentropic velocity, V_i, m/s		106.8	
Isentropic power, P_i, kW		20.86	
Velocity coefficient, K_v	0.883	0.847	0.883
Efficiency, η_n		0.721	0.782
Flow area ratio, R_a		8.9	

The quantity that chiefly influences turbine rotor efficiency is the ratio R_a of gas flow area to liquid flow area; the larger the ratio the lower the rotor efficiency. The value of R_a for this nozzle is 8.9, a smaller value than in practical turbines, but useful for research purposes in making liquid effects predominate.

F. Refrigerant-22 Data

The nozzle of Fig. 11 was tested with saturated liquid Refrigerant 22. The results are presented in Table 2.

A small amount of superheated Refrigerant-22 vapor was fed into the gas inlet to give a starting quality of 2 percent. For the measured total flow rate, the nozzle program calculated a throat area 4 percent less than actual. The measured exit velocity is 2 percent higher than theoretical. The fitted nozzle efficiency shows a 14-percent improvement over the water-and-nitrogen nozzle efficiency of 0.78. The efficiency is higher because the higher molecular weight of Refrigerant-22 vapor gives lower slip velocity, and the lower surface tension of Refrigerant-22 liquid gives smaller drop diameter.

G. LLL Turbine Nozzle

The nozzle used in the Lawrence Livermore Laboratory (LLL) turbine tests (Refs. 13 and 14) was analyzed by the nozzle program, and the results are presented in Table 3.

The theoretical nozzle efficiency is 0.865. The theoretical velocity coefficient is 0.90. The measured velocity coefficient (Table 16 of Ref. 13) was 0.94 when the nozzle was tested without the exit duct used in turbine tests and 0.91 with the exit duct. The velocity coefficient was only 0.83 based on thrust measurements during turbine tests. Because of the uncertainty in the nozzle performance, the theoretical performance values given in Table 3 will be the ones used in analyzing the turbine tests.

Table 2. Comparison of theoretical and experimental nozzle performance using Refrigerant 22

Item	Value		
	Measured	Nozzle program	Fitted
Inlet			
Temperature, T_1, ^{o}C	18.6	18.6	
Pressure, p_1, kPa	875	875	
Total flow rate, $\dot{m}_t$, kg/s	1.339	1.339	
Liquid flow rate, $\dot{m}_\ell$, kg/s	1.312	1.312	
Gas flow rate, $\dot{m}_g$, kg/s	0.027	0.027	
Quality, x_1	0.02	0.02	
Velocity, V_1, m/s	1.7	1.7	
Throat			
Pressure, p_t, kPa		726	
Mean velocity, $\bar{V}_t$, m/s		22.6	
Area, A_t, mm^2	135	129	
Quality, x_t		0.059	
Exit			
Pressure, p_2, kPa	98.6	98.6	
Temperature, T_2, ^{o}C		-41	
Drop diameter, d_2, μm		33	
Area, A_2, mm^2	685	599	
Liquid flow rate, $\dot{m}_\ell$, kg/s		0.969	0.969
Gas flow rate, $\dot{m}_g$, kg/s		0.370	0.370
Quality, x_2		0.276	
Mixture ratio R_2		2.6	

Table 2 (contd)

Item	Value		
	Measured	Nozzle program	Fitted
Mean free-stream velocity, $\bar{V}_0$, m/s		125.3	
Mean velocity, $\bar{V}$, m/s	126	123.1	126
Liquid velocity, V_ℓ, m/s		118.0	121
Gas velocity, V_g, m/s		136.6	140
Jet power, P_{jet}, kW		10.20	10.72
Isentropic velocity, V_i, m/s		134.4	
Isentropic power, P_i, kW		12.09	
Velocity coefficient, K_v	0.938	0.916	0.938
Efficiency, η_n		0.844	0.886
Flow area ratio, R_a		102	

Table 3. Theoretical performance of LLL turbine nozzle

Item	Value
Inlet	
Temperature, T_1, ^{o}C	224.6
Pressure, p_1, kPa	2528
Total flow rate, $\dot{m}_t$, kg/s	0.596
Liquid (water) flow rate, $\dot{m}_\ell$, kg/s	0.512
Gas (steam) flow rate, $\dot{m}_g$, kg/s	0.084
Quality, x_1	0.141
Velocity, V_1, m/s	15.0
Throat	
Pressure, p_t, kPa	1787
Mean velocity, $\bar{V}_t$, m/s	131.9
Area, A_t, mm^2	72.5
Quality, x_t	0.174
Exit	
Pressure, p_2, kPa	13.2
Temperature, T_2, ^{o}C	51.3
Drop diameter, d_2, μm	22
Area, A_2, mm^2	2615
Liquid flow rate, $\dot{m}_\ell$, kg/s	0.397
Gas flow rate, $\dot{m}_g$, kg/s	0.199
Quality, x_2	0.334
Mean free-stream velocity, $\bar{V}_0$, m/s	633.6
Mean velocity, $\bar{V}$, m/s	627.0
Liquid velocity, V_ℓ, m/s	508.7

Table 3 (contd)

Item	Value
Gas velocity, V_g, m/s	863.0
Jet power, P_{jet}, kW	125.5
Isentropic velocity, V_i, m/s	697.7
Isentropic power, P_i, kW	145.1
Velocity coefficient, K_v	0.899
Efficiency, η_n	0.865
Flow area ratio, R_a	3300

The drop diameter of 22 μm calculated for the LLL turbine nozzle is several times larger than that for the small nozzles of Refs. 11 and 12, because the turbine nozzle is longer and the pressure gradient is smaller, resulting in less shear to break up the drops.

H. Wet-to-Dry Nozzle

A toluene wet-to-dry (WD) nozzle was analyzed to determine the theoretical effect of expanding to dry vapor. The calculated efficiency is very high. For toluene expanding from 289°C and 0.01 quality to 70°C, the exit quality is 1.0 and the efficiency is 0.98.

Figure 15 shows how the nozzle diameter, quality, and phase velocities vary from inlet to exit for a toluene WD nozzle of 1.0-kg/s flow rate. The specified pressure profile is shown in the upper curve. The large nozzle length of 0.76 m is chosen to give a 2.5-deg divergence half-angle. The throat diameter is 9.8 mm, the exit diameter is 53 mm, and the expansion area ratio is 29. The area ratio is large because the quality at the throat is only 0.24 and most of the vapor remains to be formed. The vapor exit velocity (representing the entire mass flow at the exit) is 503 m/s. The isentropic velocity is 508 m/s.

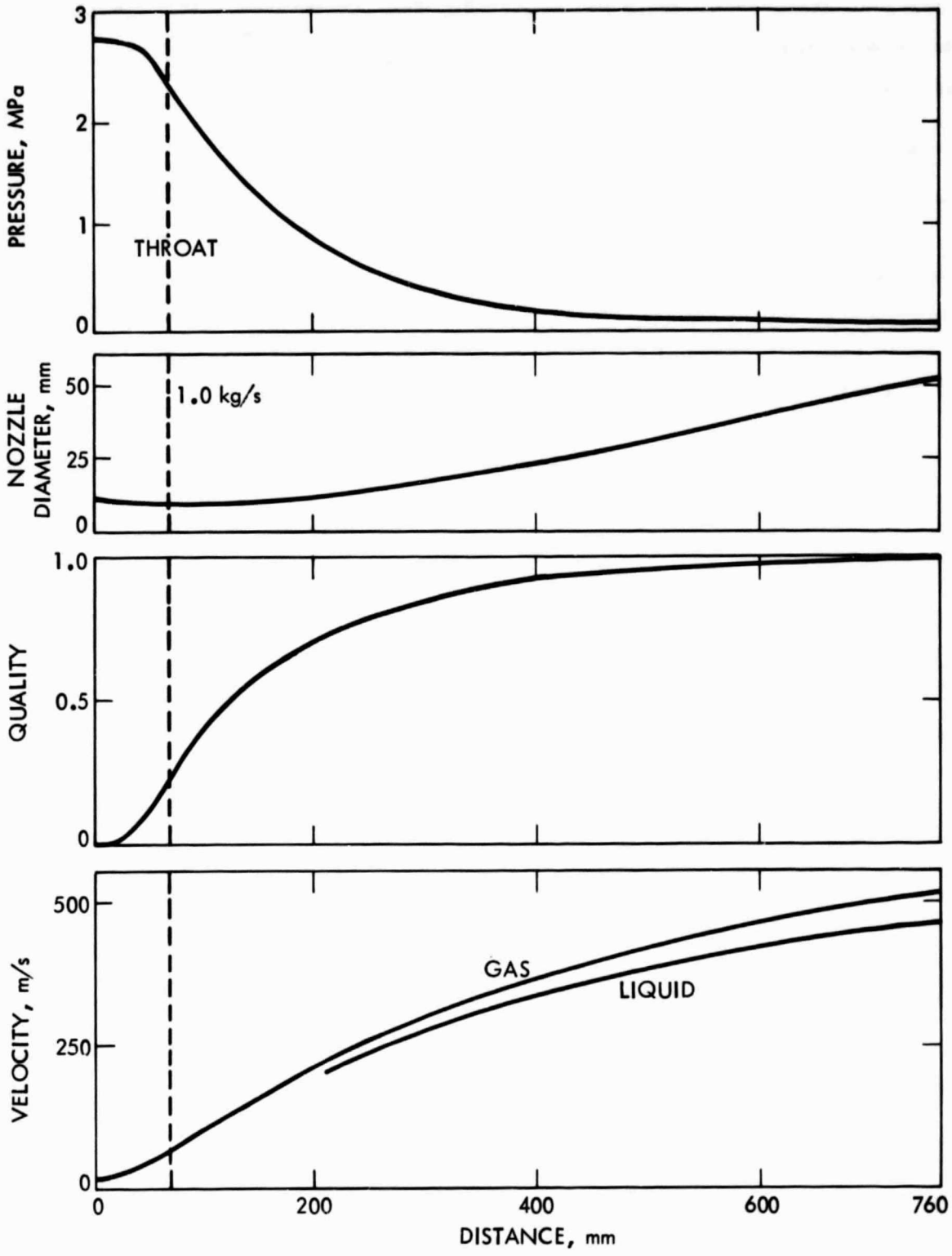

Fig. 15. Wet-to-dry expansion of toluene from 289°C to 70°C

SECTION V
ROTORS

A. Erosion

One of the uncertainties in two-phase turbines is blade erosion. Even if performance problems are overcome, will satisfactory lifetime be possible? There should be no problem at the low velocities of organic working fluids, but there may be a problem with steam-and-water mixtures. Blade erosion measurements in steam turbines have been correlated by the following relation (Ref. 15):

$$\frac{\text{mass loss per unit area}}{\text{mass of liquid impinging per unit area}} = K(V - V_c)^{2.6} \qquad (15)$$

where V is the speed of the impinging liquid drops and V_c is a threshold velocity below which little or no erosion occurs.

The threshold velocity given in Ref. 15 for 12-percent chrome steel is 120 m/s. The turbine blades in a two-stage, two-phase turbine travel at about two-thirds the speed of the jet. The jet velocity can, therefore, be 360 m/s without erosion, by this criterion. However, the velocity for steam-and-water mixtures is higher than this at many conditions of interest; the liquid velocity for the LLL turbine, for example (Table 3), is 509 m/s. Therefore, rapid erosion is a possibility in steam-and-water two-phase turbines.

For organic working fluids, the velocity is much lower. Refrigerant 113 expanding from 150°C to 46°C and 0.64 quality in a waste-heat cycle, for example, reaches only 158 m/s.

Erosion was also of concern in the liquid-metal MHD project (Ref. 2). Erosion tests were made with a water-and-nitrogen jet at 137 m/s. A blunt-tipped aluminum cone placed in the jet eroded back 1.8 mm in 1100 hours, but 304

stainless steel eroded at only a tenth of that rate. These results indicate that erosion rates of reasonably hard alloys at relative speeds below about 120 m/s should not be a problem.

A WD-cycle turbine would, in principle, escape erosion entirely because only dry vapor enters the rotor.

B. Liquid Path

The key fact about the flow leaving the nozzle and entering the rotor in a two-phase turbine is that the drops are large, the gas density is low, and the drops travel in a straight line like bullets until they hit something.

Figure 16 shows the results of trajectory calculations for water drops in a water-and-nitrogen jet at atmospheric pressure. The mixture travels through a 90-degree bend. Small drops follow the gas with only a small outward drift, and only the drops starting near the outer wall impinge. Large drops travel straight into the wall. The fraction of entering liquid that impinges on the outer wall is plotted against drop diameter for various channel curvatures and flow velocities. Even for the largest channel radius (50 mm) and smallest velocity (75 m/s) there is complete impingement of drops larger than 13 μm in diameter; a 13-μm drop entering at the inner wall would just strike the outer wall at the end of the turn. Even 2.5-μm drops would suffer 50-percent impingement (those drops entering the outer half of the channel) at 150- to 250-m/s velocity and a 25-mm channel radius. Thus, drop diameters can be only 1 to 2 μm for small impingement fractions at practical conditions. Such diameters are below the range produced by two-phase nozzles.

Liquid flow behavior was studied photographically in the turbine rotor obtained from LLL, which will be referred to as Rotor 1. The blade shape is shown in Fig. 17. Figure 18 is a 1-μs flash photograph of the flow leaving the rotor in water-and-nitrogen tests. The total flow rate is 3.6 kg/s, the mixture ratio of water to nitrogen is 45, the jet velocity (mean velocity $\bar{V}$) is 80 m/s, the rotor speed is 1540 rpm (the speed for maximum efficiency), the blade speed is 42 m/s (downward in the photograph), and the shaft output power is 8.1 kW. The drop diameter calculated by the nozzle program is 150 μm.

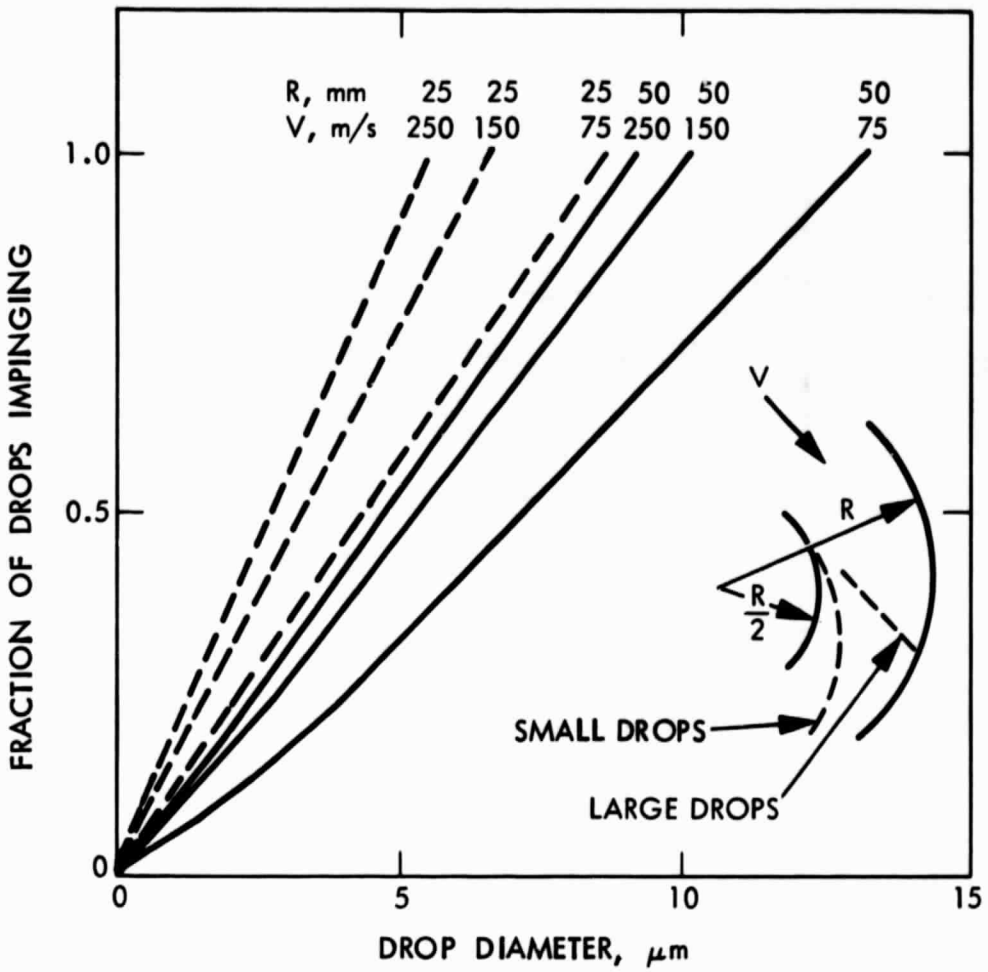

Fig. 16. Effect of drop diameter on liquid impingement

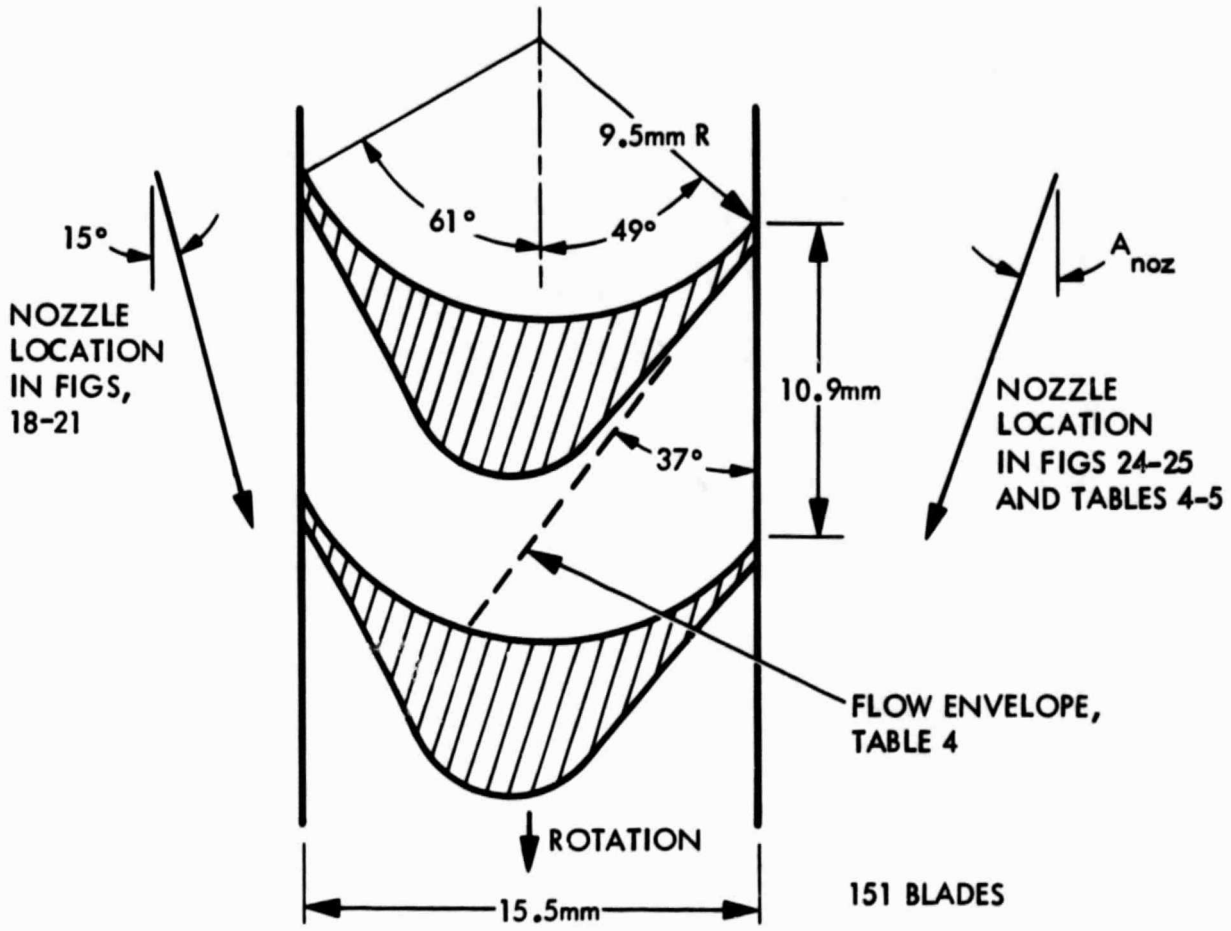

Fig. 17. Rotor 1 blade shape

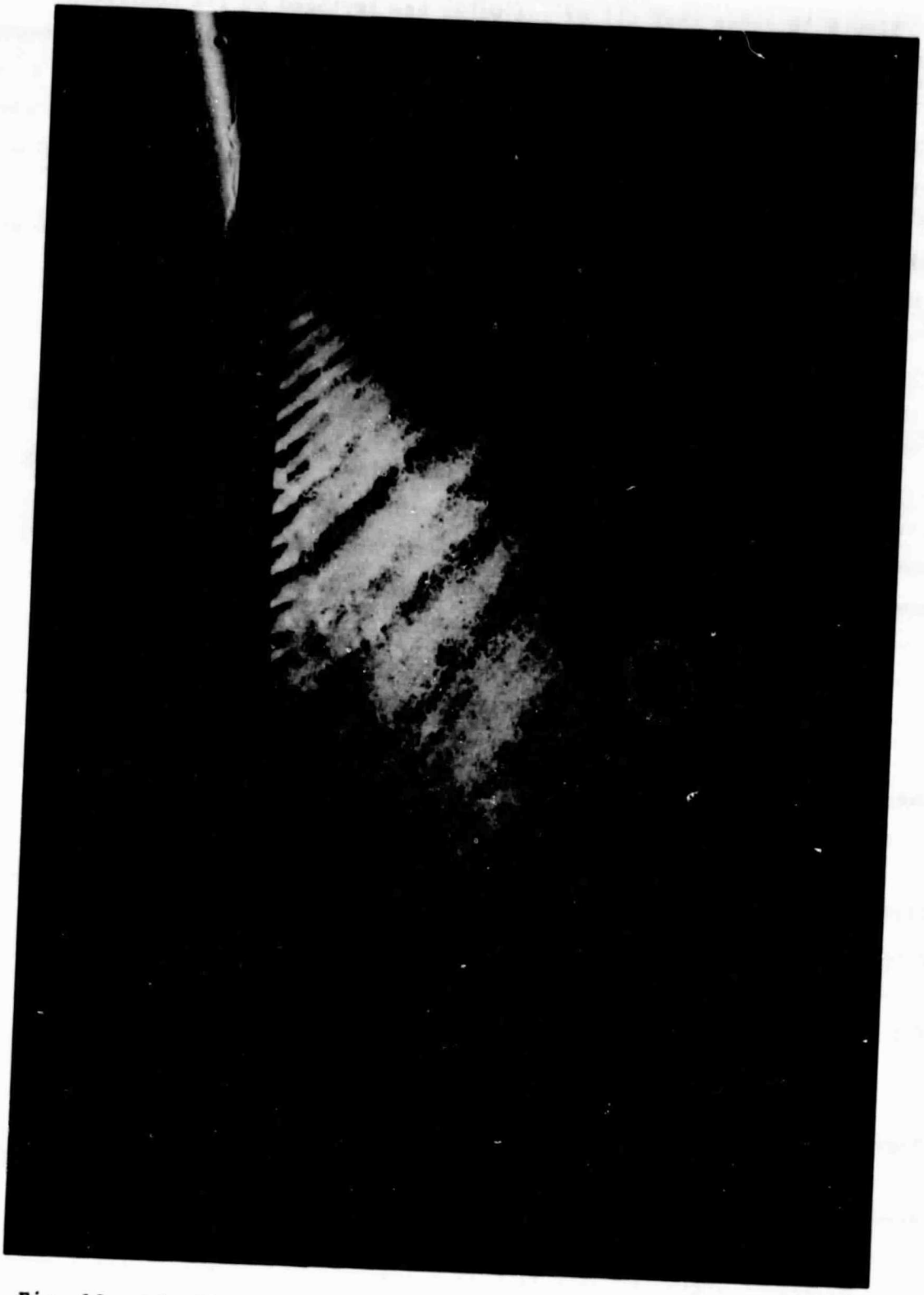

Fig. 18. Liquid exit flow at high liquid/gas mixture ratio (R = 45)

Figure 18 shows that all of the water has impinged on the concave (upward-facing) sides of the blades and formed thin liquid sheets. The sheets are only about 0.5-mm thick, 5 percent of the blade spacing. The leading edge of each sheet emerges from a blade when the blade has traveled about half way down across the nozzle exit; at that position the first liquid intercepted by the blade has had time to cross the blade. Similarly, the trailing edge of each liquid sheet leaves when the blade has traveled about a half nozzle width beyond the end of the nozzle.

To the eye, the flow has the same appearance as the jet leaving a nozzle. The rotor has merely slowed and deflected the nozzle jet.

Figure 19 is an axial view of the same flow. The first sheet of exit flow appears opposite the middle of the nozzle exit. About three leading edges can be seen before the emerging sheets are hidden behind the foreground flow. The liquid leaves in a direction tangent to the rotor but deflected slightly outward from the original direction of nozzle flow.

The vector velocities, both relative and absolute, of the liquid leaving the rotor can be measured from the photographs. The exit velocity relative to the rotor is in the plane of the liquid sheets, and is at the speed of the advancing leading edges. The absolute exit velocity is in the direction of the envelope of the sheets at the velocity of advance of the sheets in that direction. The relative exit velocity measured from Fig. 18 is 27 m/s (66 percent of the relative inlet velocity) at 43 deg above horizontal (the water does not follow the blade contour to the full 49-deg exit angle). The absolute exit velocity is 27 m/s at 46 deg below horizontal.

Two undesirable flow effects can be seen in Fig. 18. Some of the water leaves the rotor on the nozzle side, and the trailing edges of the liquid sheets do not detach cleanly. These effects, which reduce efficiency, will be discussed in a later section.

Figure 20 shows the exit flow at a lower liquid flow rate and higher velocity. The liquid flow rate is 1.9 kg/s, the mixture ratio is 11, the jet velocity is 141 m/s, the rotor speed is 2770 rpm, the blade speed is 76 m/s,

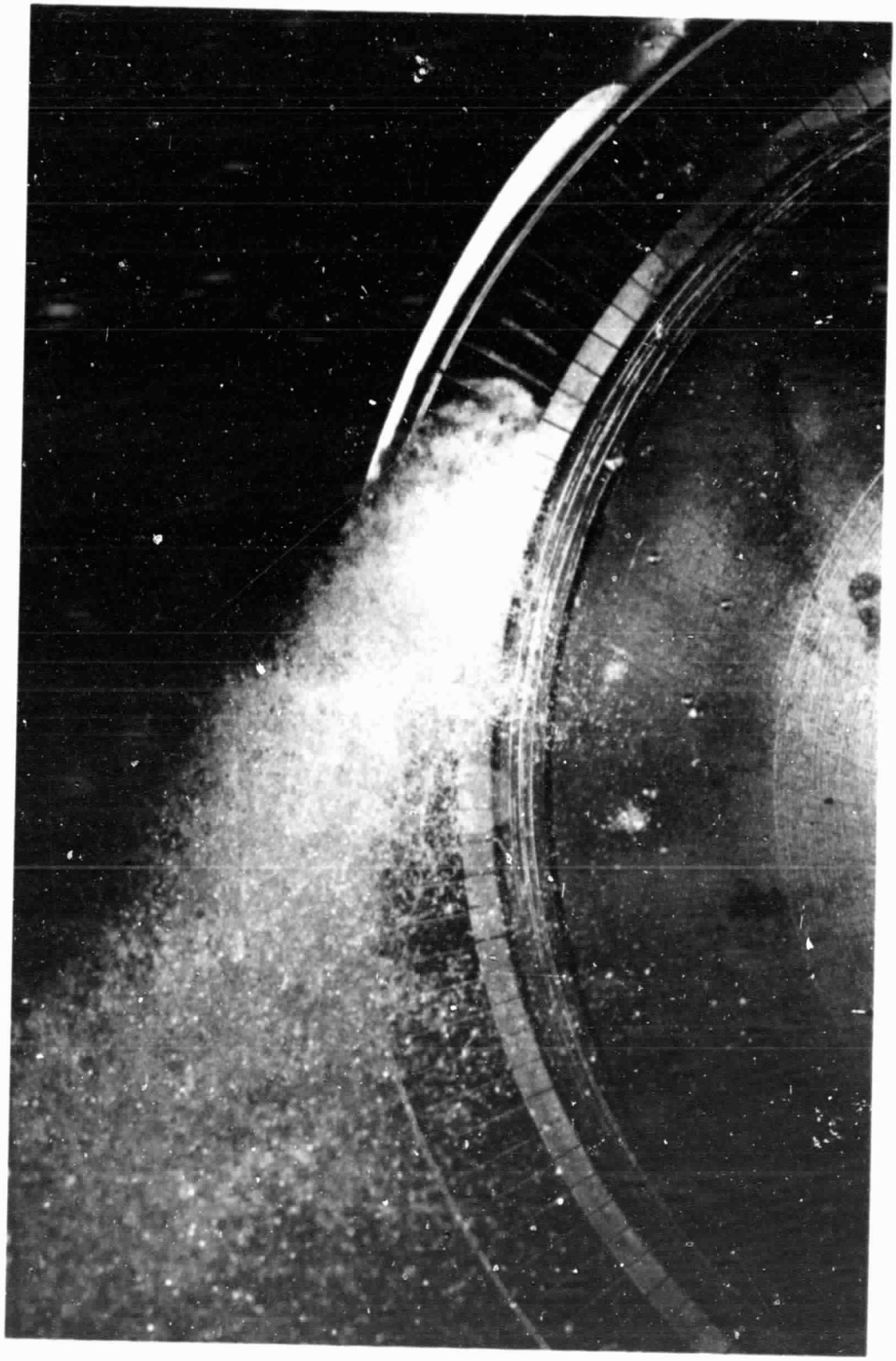

Fig. 19. Axial view of exit flow at R = 45

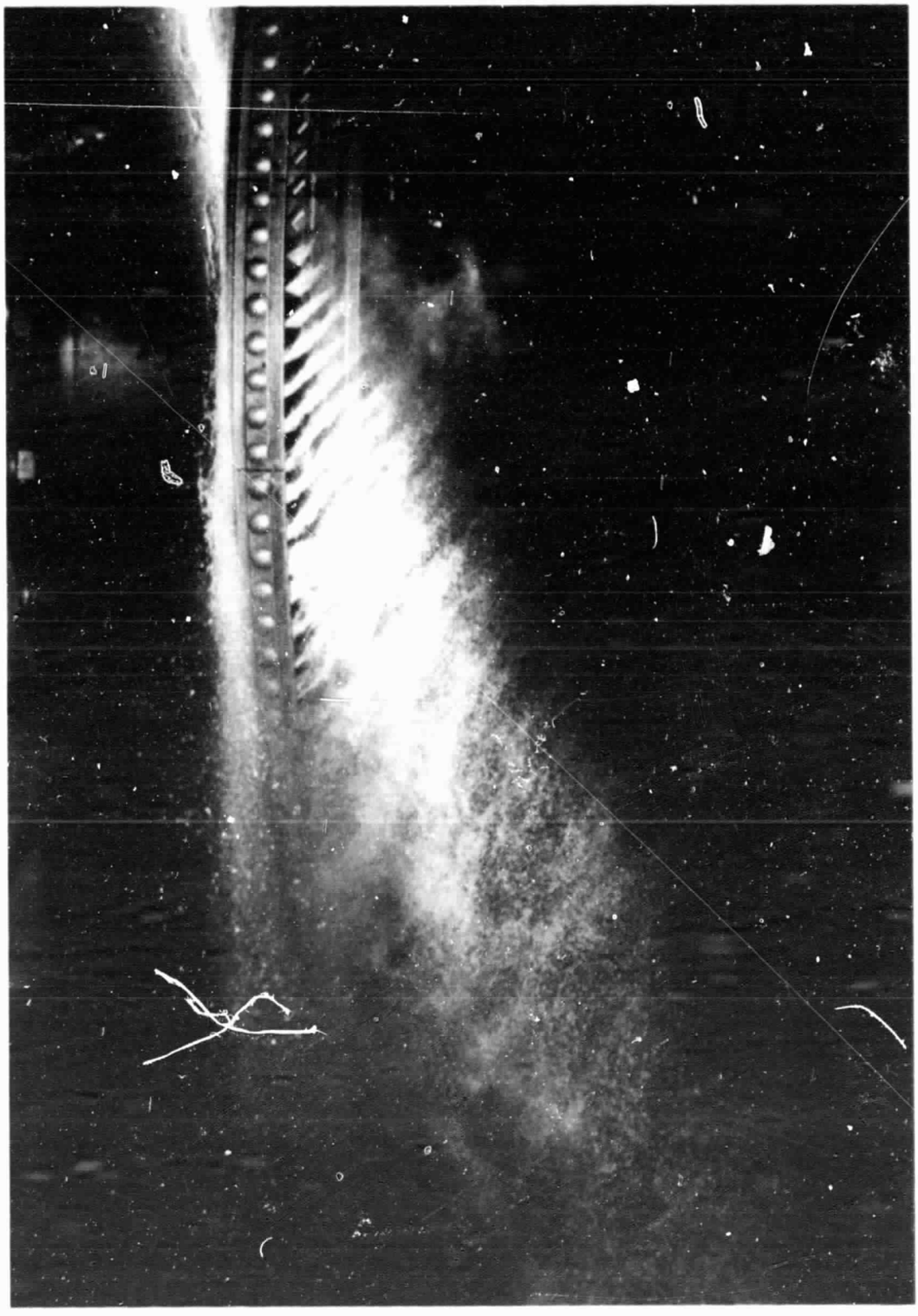

Fig. 20. Exit flow at R = 11

and the shaft power is 13.8 kW. The drop diameter from the nozzle program is 75 μm. Figure 20 shows again that the water leaves as thin sheets, but some mist is also visible above the sheets. Evidently, some of the drops from the nozzle are small enough to remain entrained in the nitrogen flow. The mist leaves the rotor in a more nearly horizontal direction than the liquid, showing that the nitrogen and entrained small drops suffer less velocity loss in the rotor than the liquid, and are ejected at a higher speed. The water velocity loss is greater than that in Fig. 18, as evidenced by the steeper downward angle of the exit flow. The relative exit velocity of the water sheets, as measured from the photograph, is 36 m/s (51 percent of the relative inlet velocity), and the absolute exit velocity is 56 m/s at 63 deg below horizontal.

Figure 21 shows the exit flow at a still lower mixture ratio. The liquid flow rate is 0.54 kg/s, the mixture ratio is 4, the jet velocity is 152 m/s, the rotor speed is 3260 rpm, the blade speed is 89 m/s, and the shaft power is 5.7 kW. The drop diameter from the nozzle program is 64 μm. More mist is visible than in the previous photograph. The relative exit velocity of the water sheets is 40 m/s (57 percent of the relative inlet velocity), and the absolute exit velocity is 66 m/s at 66 deg below horizontal.

C. Rotor Program

The picture that emerges from drop trajectory calculations and flow photographs is that the bulk of the liquid entering a two-phase turbine travels straight into the blades while the gas travels through as though the liquid were not present. Therefore, to calculate the performance of a two-phase turbine rotor, it should be sufficient to model the liquid flow as straight-in impingement, unaffected by the gas, followed by film flow along the blade surface. The gas flow can be modeled as conventional gas turbine flow, unaffected by the liquid.

Such a model is derived in Appendix A. The liquid flow is modeled in detail, but the gas is merely assumed to exert a known fraction η_g of the ideal gas-phase torque at any given speed. The ideal gas-phase force on the blades at zero turbine speed is $2 \dot{m}_g V_g$, because the gas flow is ideally

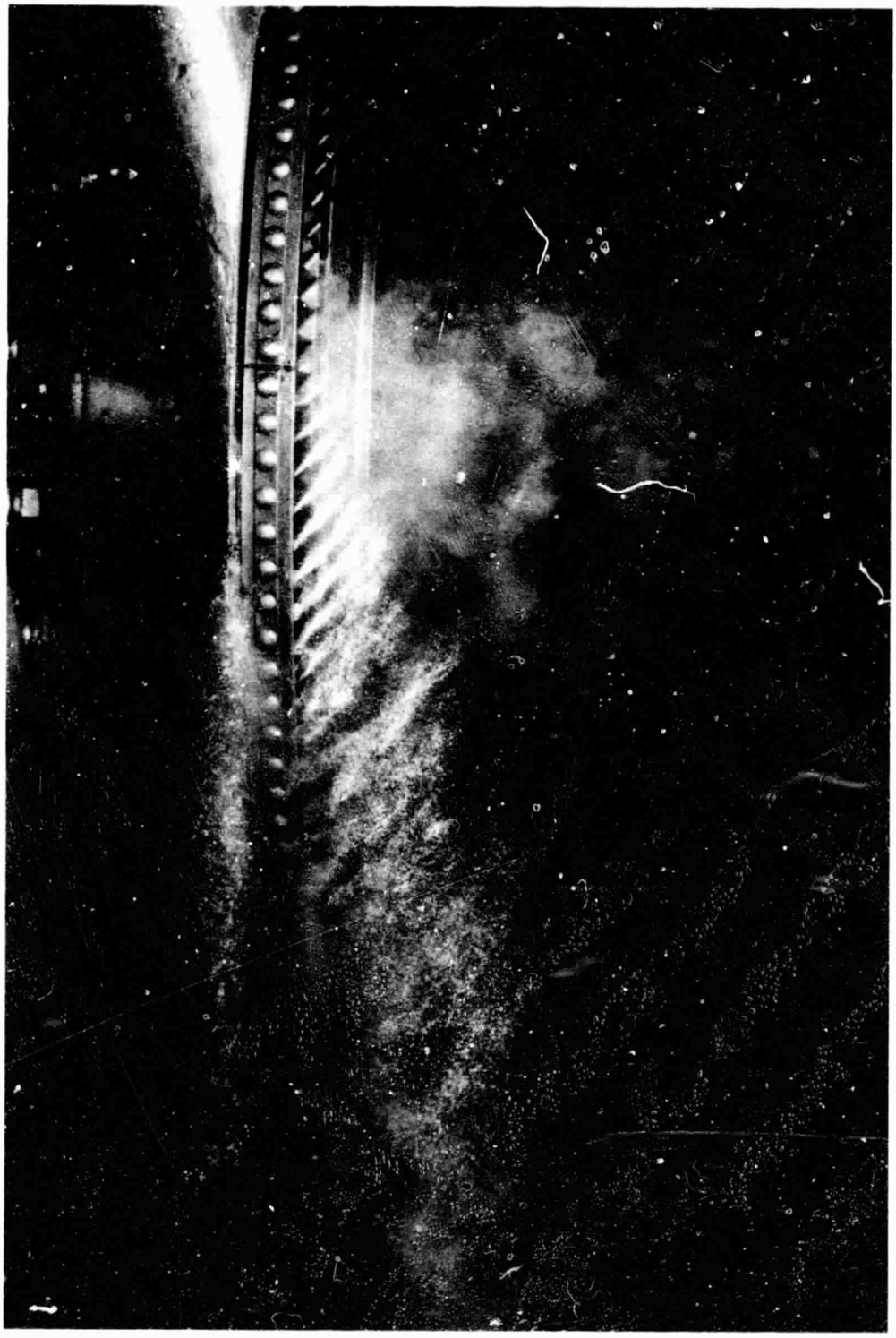

Fig. 21. Exit flow at R = 4

reversed without velocity loss. The force ideally decreases with speed in proportion to $(1 - V_b/V_g)$, where V_b is the blade speed. Thus, the gas-phase force is

$$F_g = 2 \eta_g \dot{m}_g V_g (1 - V_b/V_g) \tag{16}$$

The gas-phase efficiency $F_g V_b/(\frac{1}{2}\dot{m}_g V_g^2)$ has a peak value of η_g at a blade speed of half the gas speed. Thus, the specified gas torque factor η_g is also the peak gas-phase efficiency.

The rotor flow model of Appendix A is incorporated in a computer program that was used for the theoretical calculations presented in this report. The inputs to the program are the nozzle exit dimensions; nozzle angle relative to the rotor; rotor speed; liquid and gas flow rates; liquid and gas velocities; blade shape; rotor diameter; liquid density and viscosity; gas torque fraction (peak gas-phase efficiency) η_g; and (for windage torque calculation) gas density and viscosity.

Several different torques, powers, and efficiencies are calculated. First, the program calculates the total force F_b exerted on the blades by the two-phase flow. Multiplying this force by the rotor radius R_b to the center of the blades gives the "blade torque" L_b. Multiplying this torque by the angular speed ω gives the "blade power" P_b.

$$P_b = L_b \omega \tag{17}$$

The windage, or disc friction, torque L_w is calculated from the Mann and Marston correlations (Ref. 16). Subtracting windage torque from the blade torque gives the theoretical "rotor torque" L_r.

$$L_r = L_b - L_w \tag{18}$$

The product of rotor torque and rotor angular speed is the "rotor power" P_r.

$$P_r = L_r \omega \tag{19}$$

The ratio of the blade power to the jet power is the "blade efficiency" η_b.

$$\eta_b = \frac{P_b}{P_{jet}} \tag{20}$$

where P_{jet} is the jet power given by Eq. (12). This is the most useful efficiency for the comparison of experiment with theory.

The ratio of rotor power to jet power is the "rotor efficiency" η_r.

$$\eta_r = \frac{P_r}{P_{jet}} \tag{21}$$

The ratio of blade power P_b to isentropic power P_i will be called the "nozzle-blade efficiency" η_{nb}

$$\eta_{nb} = \frac{P_b}{P_i} = \eta_n \eta_b \tag{22}$$

where η_n is the nozzle efficiency defined in Eq. (14). The nozzle-blade efficiency is the efficiency that would be attained with a large number of nozzles so that windage loss is negligible relative to output power.

The ratio of rotor power to isentropic power is the "turbine efficiency" η_t.

$$\eta_t = \frac{P_r}{P_i} \tag{23}$$

The turbine efficiency is also equal to the product of nozzle efficiency and rotor efficiency.

$$\eta_t = \eta_n \eta_r \tag{24}$$

The turbine efficiency is the only efficiency that counts in practical applications. The other efficiencies are useful for analysis purposes.

D. Rotor Test Apparatus

Figures 22 and 23 show the apparatus used in the two-phase turbine experiments. The test rotor is driven by a 60-kW electric motor through a variable-speed belt drive and a gear box. The gear box is an automobile transmission driven from the drive-shaft side. Rotor speeds can be adjusted from 700 rpm to 6000 rpm, but the highest used in flow tests was 3500 rpm. The rotor shaft can also be locked for zero-speed tests. The gear box is connected to the rotor through a rotating strain-gage torque transducer.

The nozzle used in the turbine tests is the one shown in Fig. 11. Various throat diameters, exit diameters, and cut-off angles have been used. In some of the tests, as shown in Figs. 22 and 23, the nozzle was pivoted on bearings and restrained by a load cell for nozzle thrust measurement.

The nozzle is fed through flexible hoses. In Fig. 22, the nozzle is connected for Refrigerant 22 tests. Liquid Refrigerant 22 is fed from a nitrogen-pressurized tank through a hand-operated valve to the liquid inlet of the nozzle. Vapor is fed from a heated Refrigerant 22 cylinder (not shown).

For water-and-nitrogen tests, the liquid line is connected to water pumps, and the hand valve is used for controlling the water flow rate. In those tests, the nitrogen line is connected to the gas inlet of the nozzle, and the nitrogen flow rate is controlled by a pressure regulator.

A water sump is located under the deck plates beneath the turbine. During turbine tests, the deck plates are removed and the flow leaving the rotor discharges into the sump. In the Refrigerant-22 tests, the liquid vaporizes on contact with the water and is exhausted from the building by blowers.

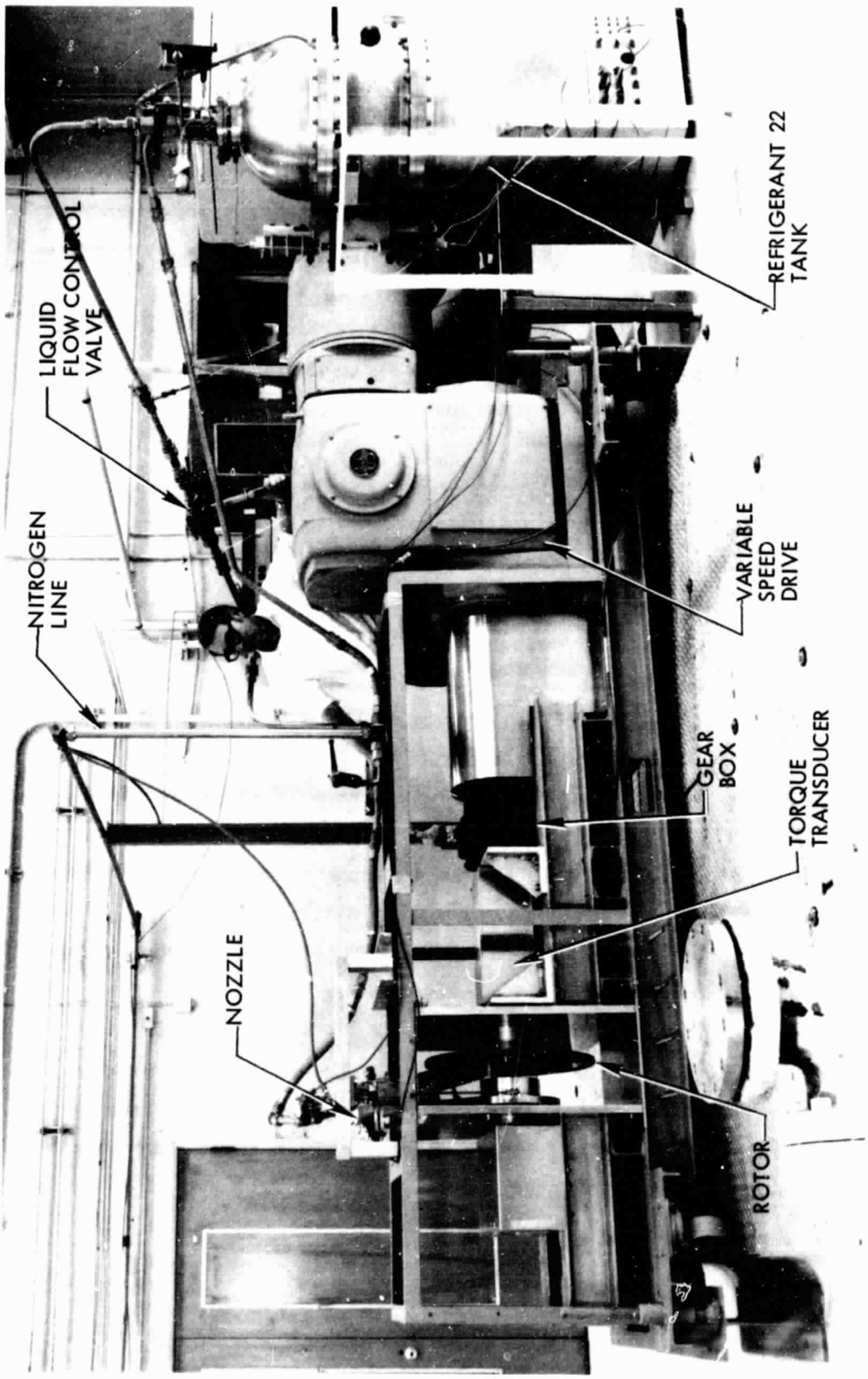

Fig. 22. Two-phase turbine experiment

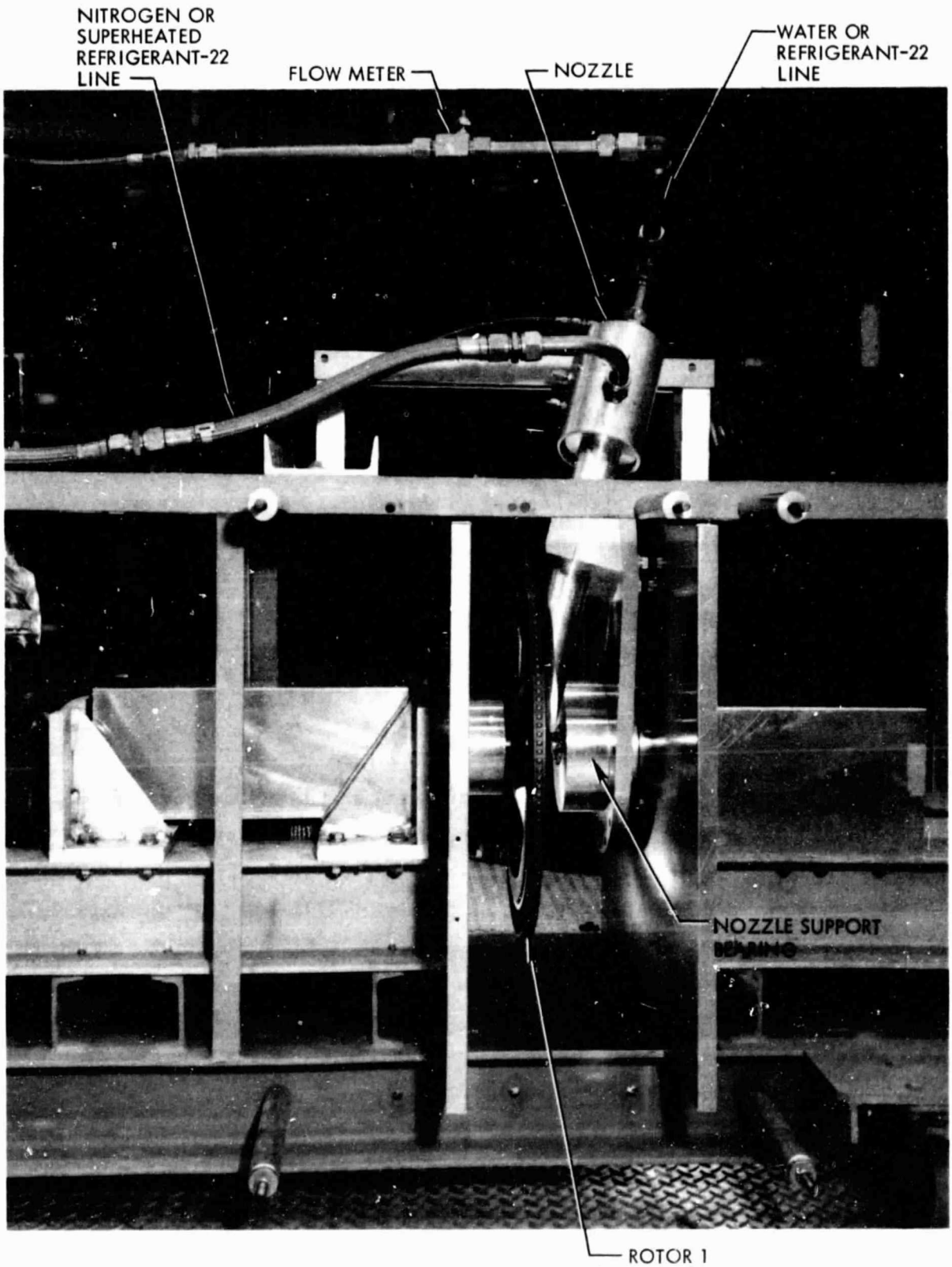

Fig. 23. Single-stage turbine

E. Measurement Procedure

The main quantity of interest for comparison with theory is the blade torque L_b. Blade torque is measured by setting the rotor speed at a desired value, with nozzle flow off, and recording the torque required to drive the rotor. Then the nozzle flow is turned on, the variable-speed drive is adjusted slightly to reduce the speed to the no-flow value, and the torque is recorded again. The torque without flow is the windage torque L_w. The torque with flow, which is a torque exerted by the rotor on the drive system (causing the electric motor to act as a generator and feed power back into the power line) is the rotor torque L_r. The sum of the two torques (measured in practice as the change in the recorder pen deflection between flow off and flow on) is the blade torque L_b.

Blade power is calculated from Eq. (17), $P_b = L_b\omega$, and the blade efficiency is calculated from Eq. (20), $\eta_b = P_b/P_{jet}$. The value used for the jet power P_{jet} is the "fitted" value obtained from the measured nozzle thrust, the calculated exit mixture ratio, and the calculated exit velocity ratio from the nozzle program, as illustrated in Table 1.

F. Water-and-Nitrogen Turbine Data

Rotor 1 was tested with water and nitrogen at the nozzle conditions given in Table 1. The nozzle was mounted at an angle A_{noz} of 20 deg on the right side of the rotor as drawn in Fig. 17.

Figure 24 presents the measured blade torque L_b as a function of rotor speed. The torque varies from 125 N-m at zero speed to 40 N-m at 2250 rpm, and the torque follows a straight line. The speed at which the torque extrapolates to zero is 3300 rpm, corresponding to a blade speed of 91 m/s, which is close to the nozzle exit velocity.

Figure 24 also presents the theoretical torque calculated by the rotor program (Appendix A). The gas torque factor η_g (equal to the peak gas-phase efficiency) is specified as 0.8; the true value of η_g is probably in the range 0.6 to 0.9, but the nitrogen flow rate is so small compared with the water flow rate in these tests that the uncertainty in η_g has negligible effect on the theoretical torque.

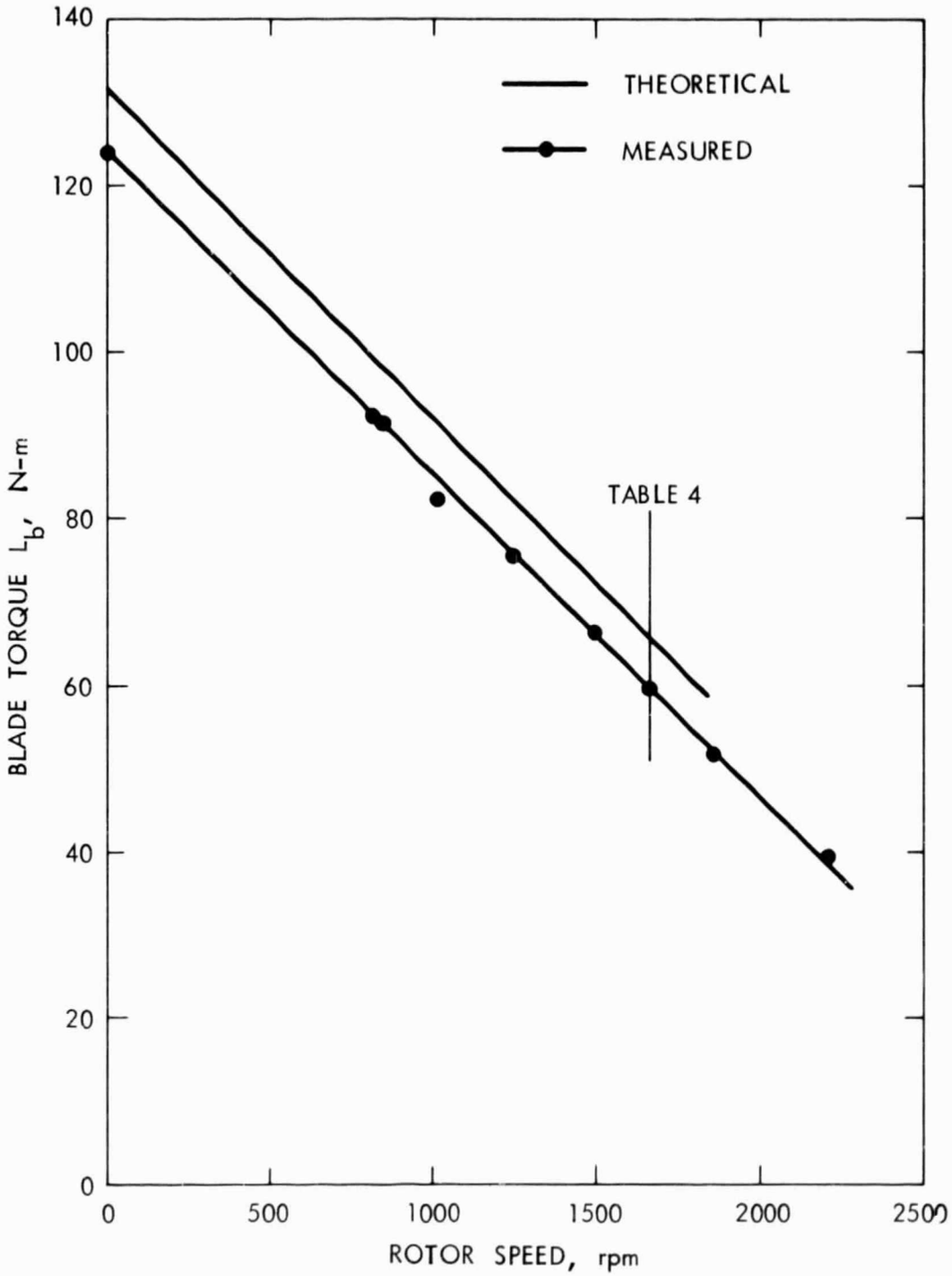

Fig. 24. Comparison of theoretical and experimental torques of water-and-nitrogen turbine

The theoretical blade torque varies from 132 N-m at zero speed to 59 N-m at 1850 rpm. Beyond this speed, the rotor program calculates that the flow impinges on the backs of the blades. This effect is not modeled in the theory, and therefore the theoretical calculations are only carried to 1850 rpm.

Figure 25 compares the theoretical and experimental blade efficiencies η_b. The peak experimental efficiency is 0.631 at 1650 rpm. The peak theoretical efficiency is 0.709. The agreement between theoretical and experimental efficiencies is sufficiently close to show that the theory accounts for the major losses, but that there are additional losses amounting to about 10 percent. The possible additional losses are discussed in a later section.

Table 4 compares the theoretical and experimental performance at the peak-efficiency speed of 1650 rpm. The windage torque is six times greater than theoretical, but the theoretical windage torque from the Mann and Marston correlations is for a tightly-fitting housing, which gives lower windage torque than that for an unenclosed rotor. The theoretical values of relative inlet velocity V_1 and relative exit velocity V_3 (using the notation of Appendix A) show that there is a substantial liquid velocity loss even at the favorable operating conditions (low gas/liquid area ratio R_a) of this turbine.

G. Refrigerant-22 Turbine Data

Rotor 1 was tested with Refrigerant 22 at the nozzle conditions of Table 2. Because only a few runs of about 10 seconds duration could be made due to cost and tank-size limitations, the tests were made only at the theoretical peak-efficiency speed of 1880 rpm.

The results for the run with the steadiest conditions and most reliable data are presented in Table 5. The measured blade efficiency is essentially the same as in the water-and-nitrogen tests. However, this efficiency is only 2 percent less than the theoretical blade efficiency using an assumed gas torque

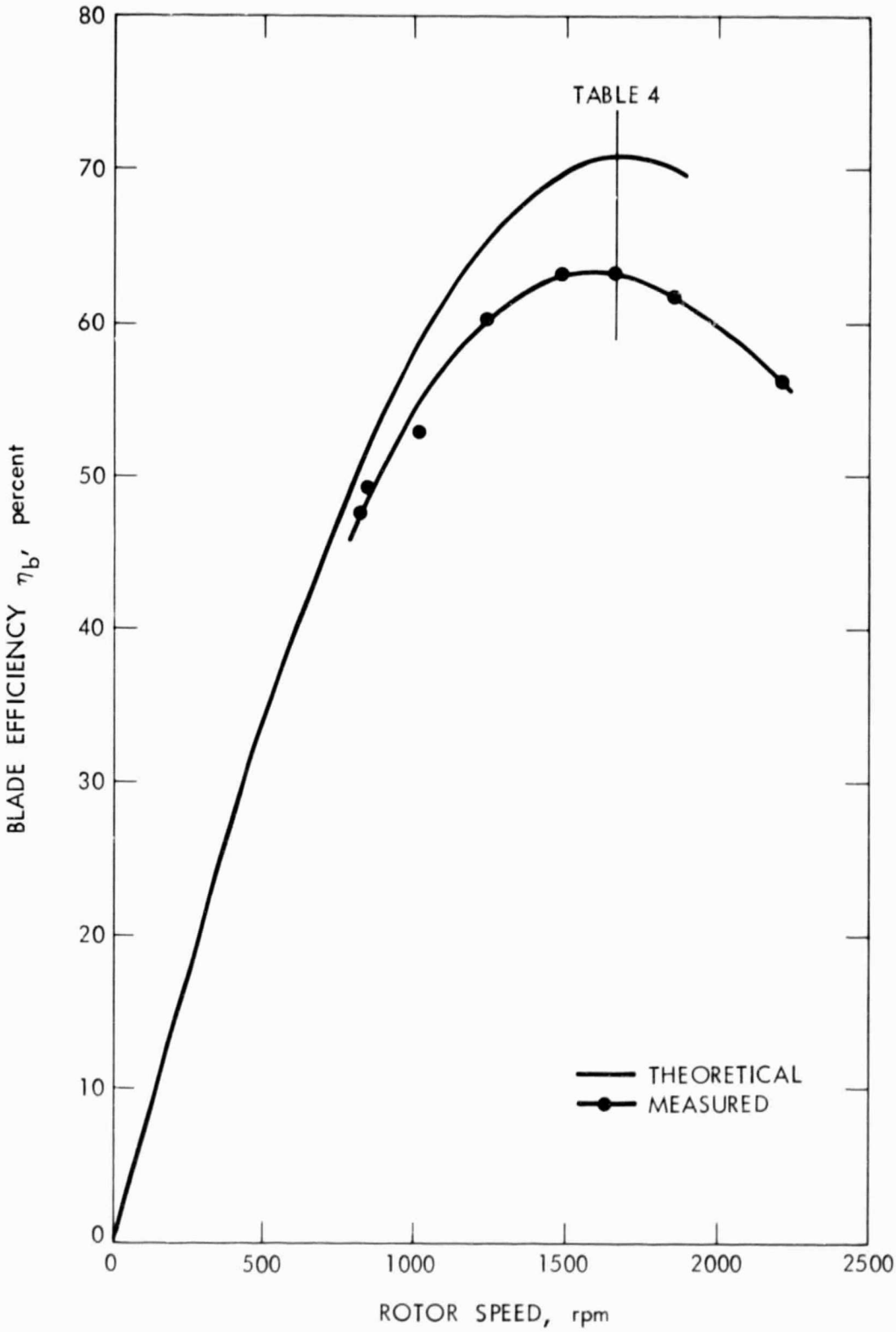

Fig. 25. Comparison of theoretical and experimental efficiencies of water-and-nitrogen turbine

Table 4. Comparison of theoretical and experimental turbine performance using water and nitrogen (Table 1 nozzle conditions)

Item	Value	
	Measured	Rotor program
Nozzle angle, A_n, deg	20	20
Rotor radius, R_b, mm	263	263
Rotor speed, N, rpm	1652	1652
Rotor torque, L_r, N-m	57.2	66.5
Windage torque, L_w, N-m	2.3	0.4
Blade torque, L_b, N-m	59.5	66.9
Rotor power, P_r, kW	9.90	11.50
Blade power, P_b, kW	10.29	11.57
Rotor efficiency, η_r	0.607	0.704
Blade efficiency, η_b	0.631	0.709
Nozzle-blade efficiency, η_{nb}	0.494	0.555
Turbine efficiency, η_t	0.475	0.551
Relative inlet velocity, V_1, m/s		53.3
Relative exit velocity, V_3, m/s		29.6

Table 5. Comparison of theoretical and experimental turbine performance using Refrigerant 22 (Table 2 nozzle conditions)

Item	Value	
	Measured	Rotor program
Nozzle angle, A_n, deg	15	15
Rotor radius, R_b, mm	261	261
Rotor speed, N, rpm	1880	1880
Rotor torque, L_r, N-m	32.2	34.0
Windage torque, L_w, N-m	1.7	0.5
Blade torque, L_b, N-m	33.9	34.5
Rotor power, P_r, kW	6.34	6.69
Blade power, P_b, kW	6.67	6.79
Rotor efficiency, η_r	0.591	0.624
Blade efficiency, η_b	0.622	0.633
Nozzle-blade efficiency, η_{nb}	0.551	0.561
Turbine efficiency, η_t	0.524	0.553
Relative inlet velocity, V_1, m/s		72.6
Relative exit velocity, V_3, m/s		19.2

factor (gas phase efficiency) η_g of 0.8. The uncertainty in the gas-phase efficiency introduces perhaps a 5-percent uncertainty in the theoretical torque because the liquid/gas mixture ratio is only 2.6.

The measured turbine efficiency of 0.52 is the highest efficiency achieved with a two-phase turbine to date.

H. LLL Steam-and-Water Turbine Data

A two-phase turbine was tested by Lawrence Livermore Laboratory with a water-and-steam mixture at the nozzle conditions of Table 3. The results are reported in Refs. 13 and 14.

The measured turbine efficiency η_t of the LLL turbine is plotted in Fig. 30 of Ref. 13. Blade torque is recovered from those measurements as follows: The η_t values are multiplied by the isentropic jet power P_i = 145.1 kW (Table 3); the resulting rotor power values P_r are divided by the rotor speed ω at each data point to recover the rotor torque values L_r; the experimental windage torque L_w at each data point is then calculated from the measured moment coefficients given in Fig. 29 of Ref. 13; adding L_r to L_w gives the measured blade torque L_b; multiplying L_b by rotor speed ω gives the measured blade power P_b.

The windage torque in the LLL tests was very large — 30 percent of the blade torque and six times the torque calculated from the Mann and Marston correlations for a closely fitting housing. Because it cannot be expected that the windage torque measured in motoring tests is exactly the same as the torque that should be added to rotor torque to obtain blade torque, there is an uncertainty of perhaps 5 to 10 percent in the recovered blade torque values for the LLL turbine.

The theoretical blade torque of the LLL turbine is calculated using a gas torque factor η_g of 0.8, which introduces an uncertainty of several percent since the steam flow is 33 percent of the total. An even larger uncertainty is introduced by using the theoretical nozzle velocities from Table 3 as inputs to the rotor program since reliable nozzle measurements were not available.

Figure 26 compares the theoretical and experimental blade torques of the LLL turbine. The theoretical torque curve ends at 1700 rpm, which is the speed at which liquid theoretically starts striking the backs of the blades. The torque results are similar to those obtained with the JPL water-and-nitrogen turbine, with the measured blade torques 10 to 20 percent below theoretical.

Figure 27 compares the theoretical and experimental blade efficiencies. The highest measured efficiency is 0.47 at 1815 rpm, 10 percent below theoretical. With a slightly lower blade angle to avoid impingement on the back, the rotor program predicts that the blade efficiency would reach 0.62 at 3200 rpm.

Table 6 compares the theoretical and experimental performance in more detail at the highest test speed for which the water theoretically cleared the backs of the blades, 1575 rpm. This was also the speed at which the measured turbine efficiency η_t reached its maximum value of 0.233; because of the large windage torque, the efficiency decreased again at higher speeds.

A significant theoretical result shown in Table 6 is that the relative velocity of the liquid leaving the blades is only 17 m/s, 5 percent of the relative inlet velocity. This means that the torque could be calculated simply by assuming that the liquid stops on the blades and is thrown off at rotor speed. This approximation reduces the theoretical torque of the liquid by only 4 percent. The large velocity loss of the liquid is a consequence of the very high gas/liquid area ratio $R_a = 3300$ (Table 3) which forces the liquid to spread over a large area in a very thin film. If the relative liquid velocity on the blade stayed at half the impinging velocity, the liquid film thickness would be only 22 μm.

I. Staging Method

Higher turbine efficiencies can be obtained by using two or more rotor stages. The approach is to reduce the velocity difference between the liquid and the blades and thereby reduce the energy dissipation due to friction.

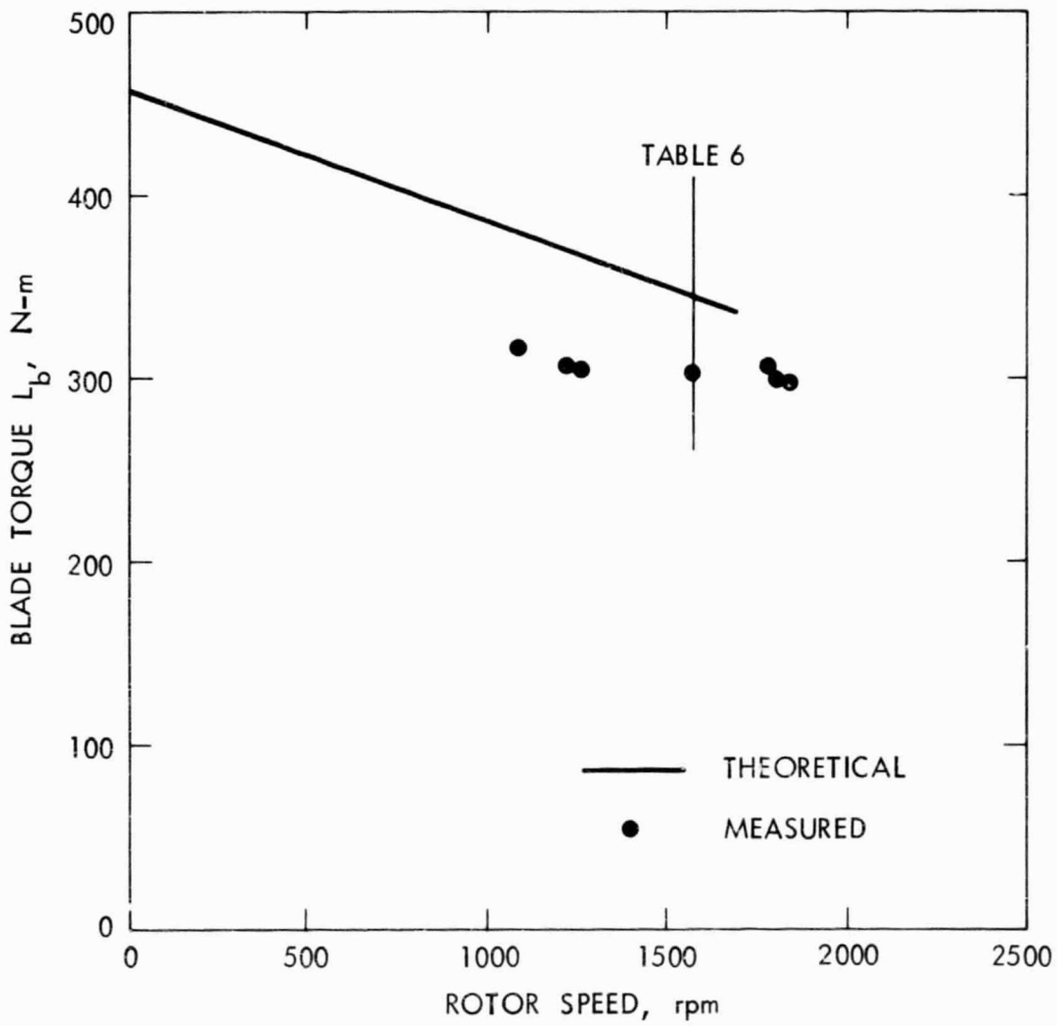

Fig. 26. Comparison of theoretical and experimental torques of LLL steam-and-water turbine

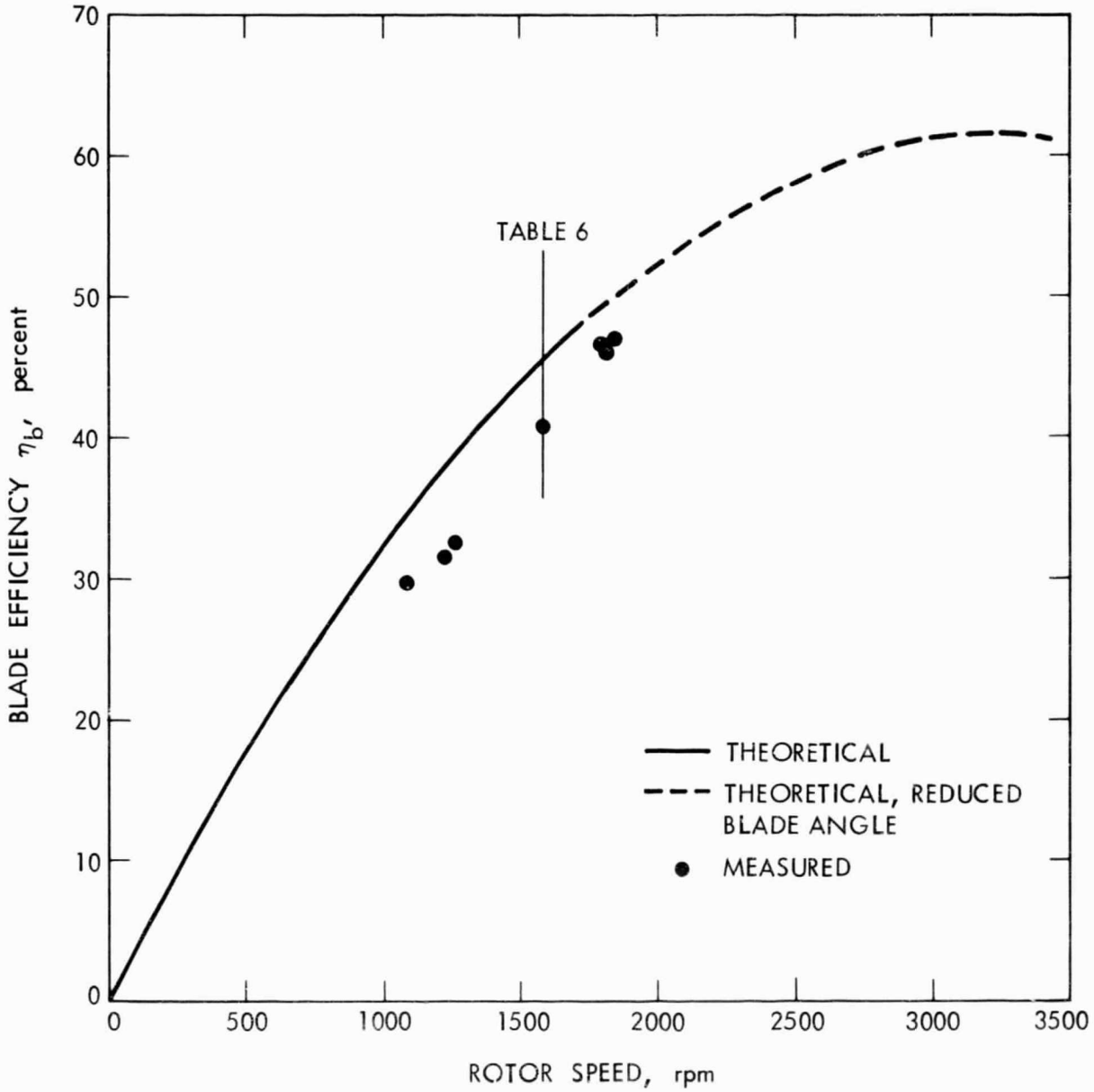

Fig. 27. Comparison of theoretical and experimental efficiencies of LLL steam-and-water turbine

Table 6. Comparison of theoretical and experimental performance of LLL steam-and-water turbine (Table 3 nozzle conditions)

Item	Value	
	Measured	Rotor program
Nozzle angle, A_n, deg	20	20
Rotor radius, R_b, mm	973	973
Rotor speed, N, rpm	1575	1575
Rotor torque, L_r, N-m	205	329
Windage torque, L_w, N-m	99	17
Blade torque, L_b, N-m	304	346
Rotor power, P_r, kW	33.8	54.3
Blade power, P_b, kW	50.1	57.1
Rotor efficiency, η_r	0.269	0.433
Blade efficiency, η_b	0.399	0.455
Nozzle-blade efficiency, η_{nb}	0.345	0.394
Turbine efficiency, η_t	0.233	0.374
Relative inlet velocity, V_1, m/s		362
Relative exit velocity, V_3, m/s		17

Figure 28 illustrates the principle. The upper diagram shows a single-stage turbine blade in which the friction loss is so large that the flow is brought to a complete halt relative to the blade. The flow rate is unity, the jet velocity is 3, in arbitrary units, and the blade is traveling at the peak-efficiency speed of 1.5, in the same units. The flow is slowed from 3 to 1.5, exerting a force of 1.5. The blade power, equal to force times velocity, is 2.25. The jet power is $3^2/2$ or 4.5. Thus, the blade efficiency is 0.5.

In the lower diagram, two stages are arranged in series so that the flow leaving the first stage enters the second. The flow is still brought to a halt relative to the blades in each stage. The first stage has a blade speed of 2. The flow is slowed from 3 to 2 in the first stage, exerting a force of 1 and providing a power of 2. The first-stage exit flow enters the second stage at the velocity of 2 and is slowed to 1, exerting a force of 1 and providing a power of 1. The total power of the two stages is 3, giving an efficiency of 0.66.

With N stages, the efficiency is $N/(N + 1)$. Thus, even with large friction and complete velocity loss in each stage, the efficiency can, in principle, approach unity with a large number of stages.

This same principle is used in drag-disc, or Tesla turbines, where the flow spirals inward between parallel discs, slowing due to the friction of the discs but always moving slightly faster than the disc speed. The efficiency can approach unity if the velocity difference between the fluid and the discs can be kept small throughout the inward spiral path.

J. First-Stage Rotor Data

To investigate staging experimentally, a second rotor was built, designated "Rotor 2," for use as the first stage with Rotor 1 as the second stage. Figure 29 shows the blade shape of Rotor 2. The blade angle is much shallower than in Rotor 1, because Rotor 2 runs at high speed, and the flow enters at a shallow angle. Before the final curved contour was machined into the blades, the rotor was tested with the flat blade shape indicated by the dashed line on the upper blade in Fig. 29.

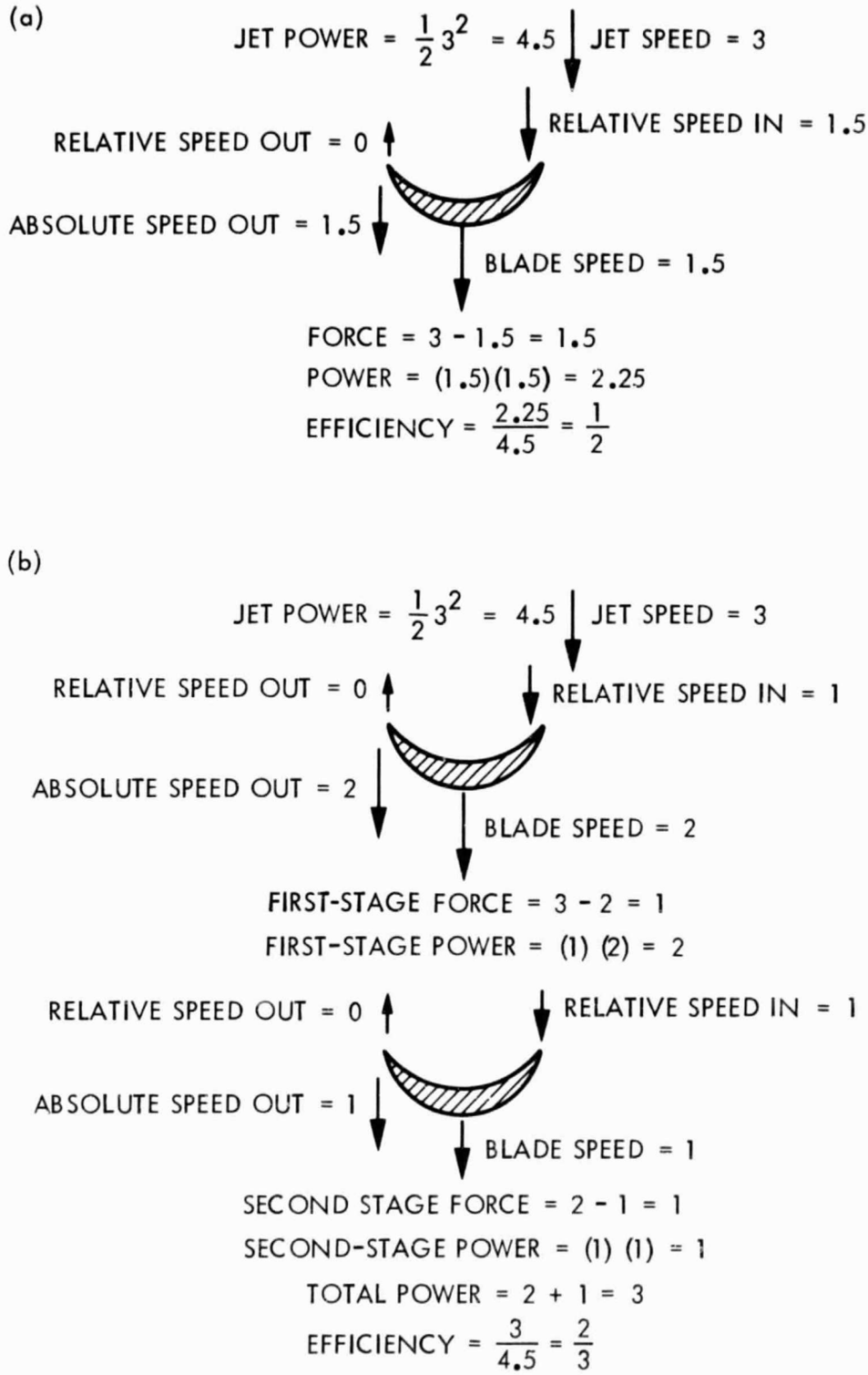

Fig. 28. Staging method: (a) single-stage turbine; (b) two-stage turbine

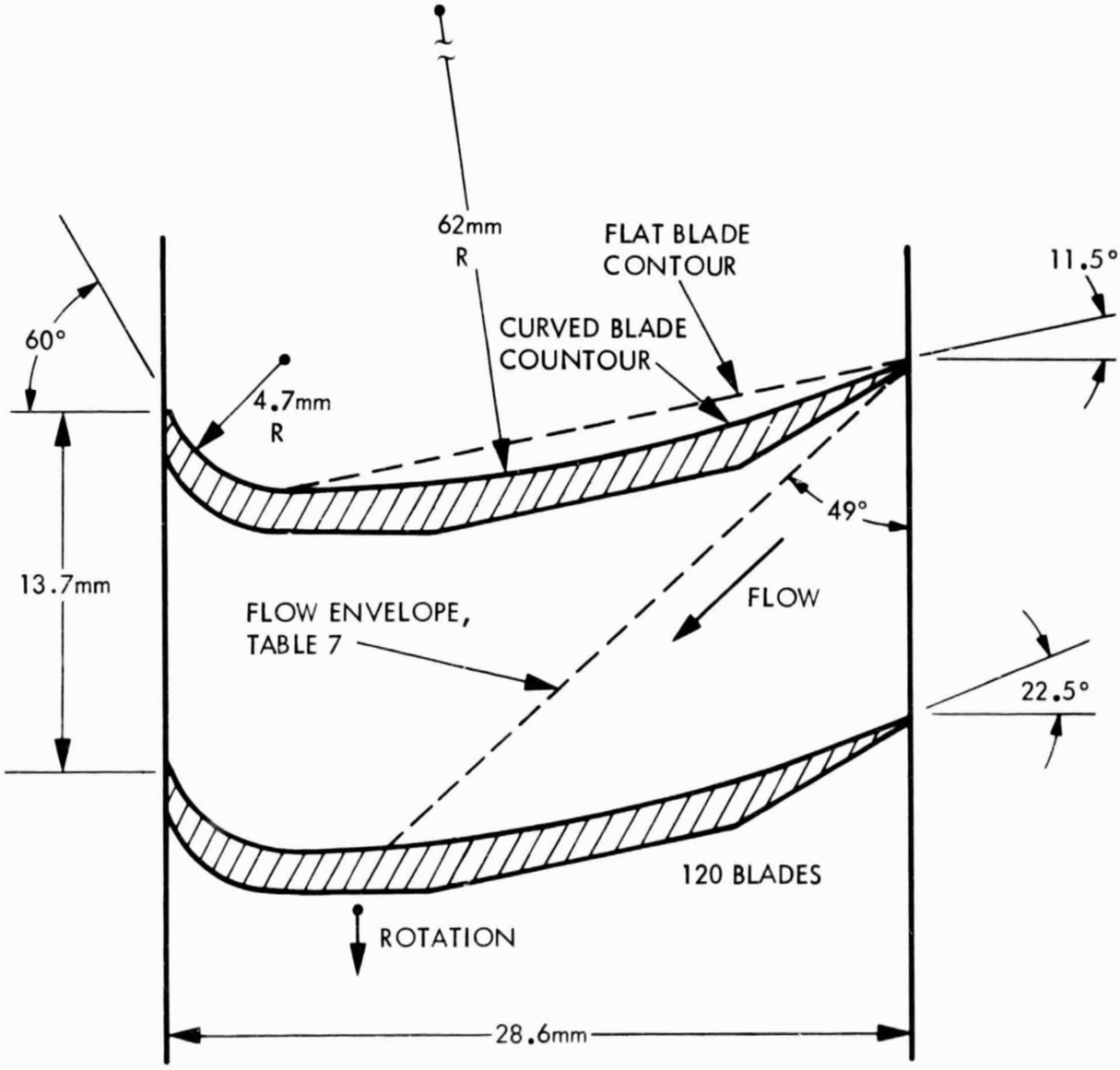

Fig. 29. Rotor 2 blade shape

Figure 30 is a 1-μs flash photograph of the water-and-nitrogen flow leaving Rotor 2 at 2200 rpm. The rotor has the flat blade contour in this photograph. The liquid leaves as thin sheets, as with Rotor 1. The downward angle of the exit flow is large because of the high rotor speed. Figure 31 shows the same flow from the axial direction. The liquid can be seen reaching the blade exit on the near side after the blade has traveled about four blade spacings from the initial point of interception of the nozzle flow.

The improvement in the flow pattern after the flat blades were remachined to the curved contour can be seen in Fig. 32. With the flat blades, the flow leaves at angles ranging from 57 deg above horizontal at the top of the jet to only 30 deg above horizontal at the bottom. With the curved blades, the flow leaves at angles between 60 and 45 deg. Evidently the curved blades provide needed centrifugal force during impingement to keep the liquid from bouncing back from the blade surface.

A comparison between theoretical and experimental blade torques is made in Fig. 33 at the nozzle conditions of Table 1. Above 2300 rpm, the liquid starts impinging on the backs of the blades, and the theoretical curve ends at that point. The assumed gas torque factor η_g is again 0.8, which may be optimistic for this rotor, but the uncertainty has little effect because of the small gas flow.

The difference between theoretical and experimental torques is greater than that for Rotor 1. At 2200 rpm, the theoretical blade torque is 54 N-m and the measured blade torque is only 40 N-m, 25 percent less. The possible reasons will be discussed in a later section. The higher torque of the curved contour, especially at low speeds, is probably the result of the higher angle of the exit flow as shown in Fig. 32.

K. Two-Stage Turbine Data

The two rotors were assembled as a two-stage turbine. As shown in Fig. 34, the first stage (Rotor 2) is connected to the variable-speed electric

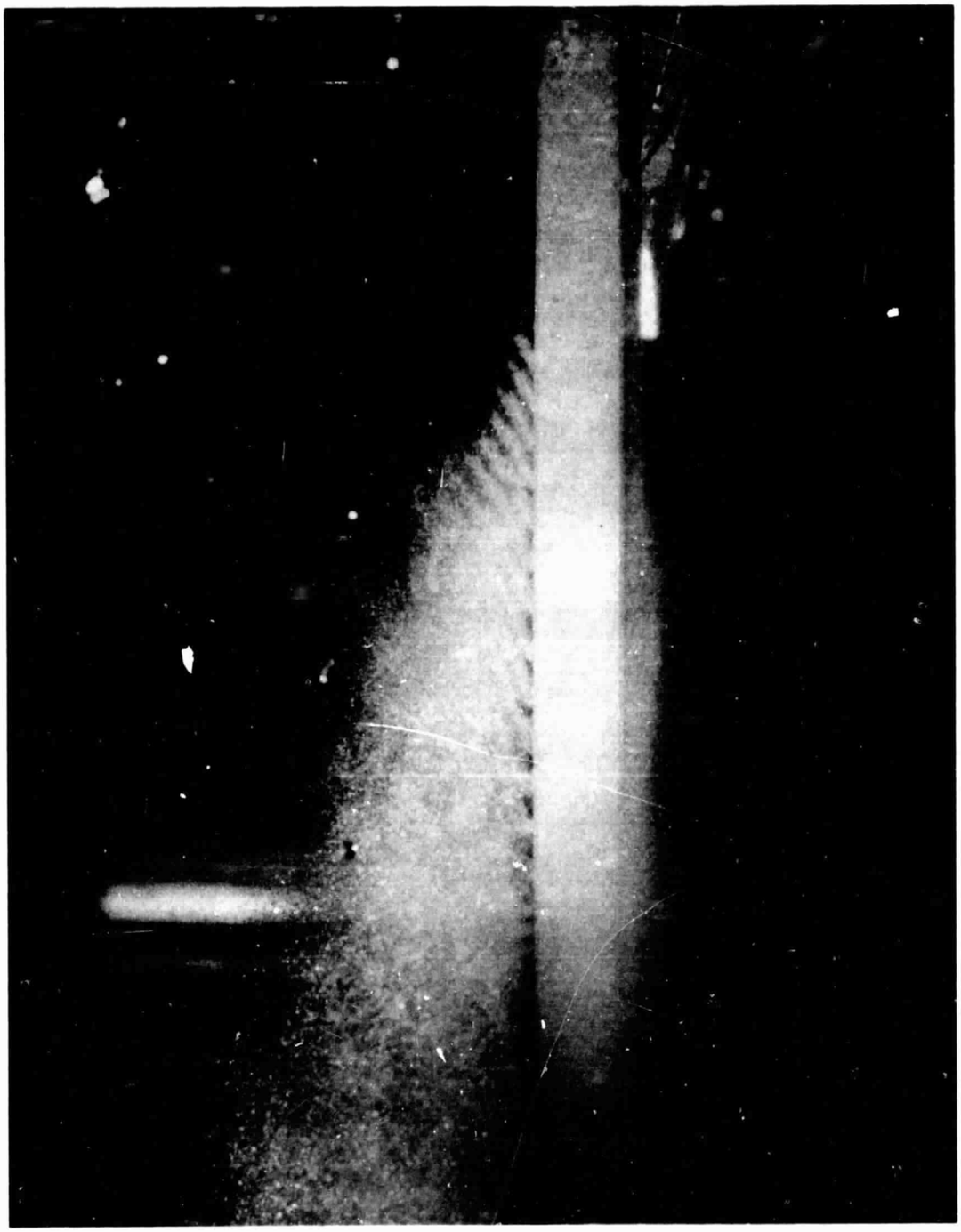

Fig. 30. Exit flow from Rotor 2

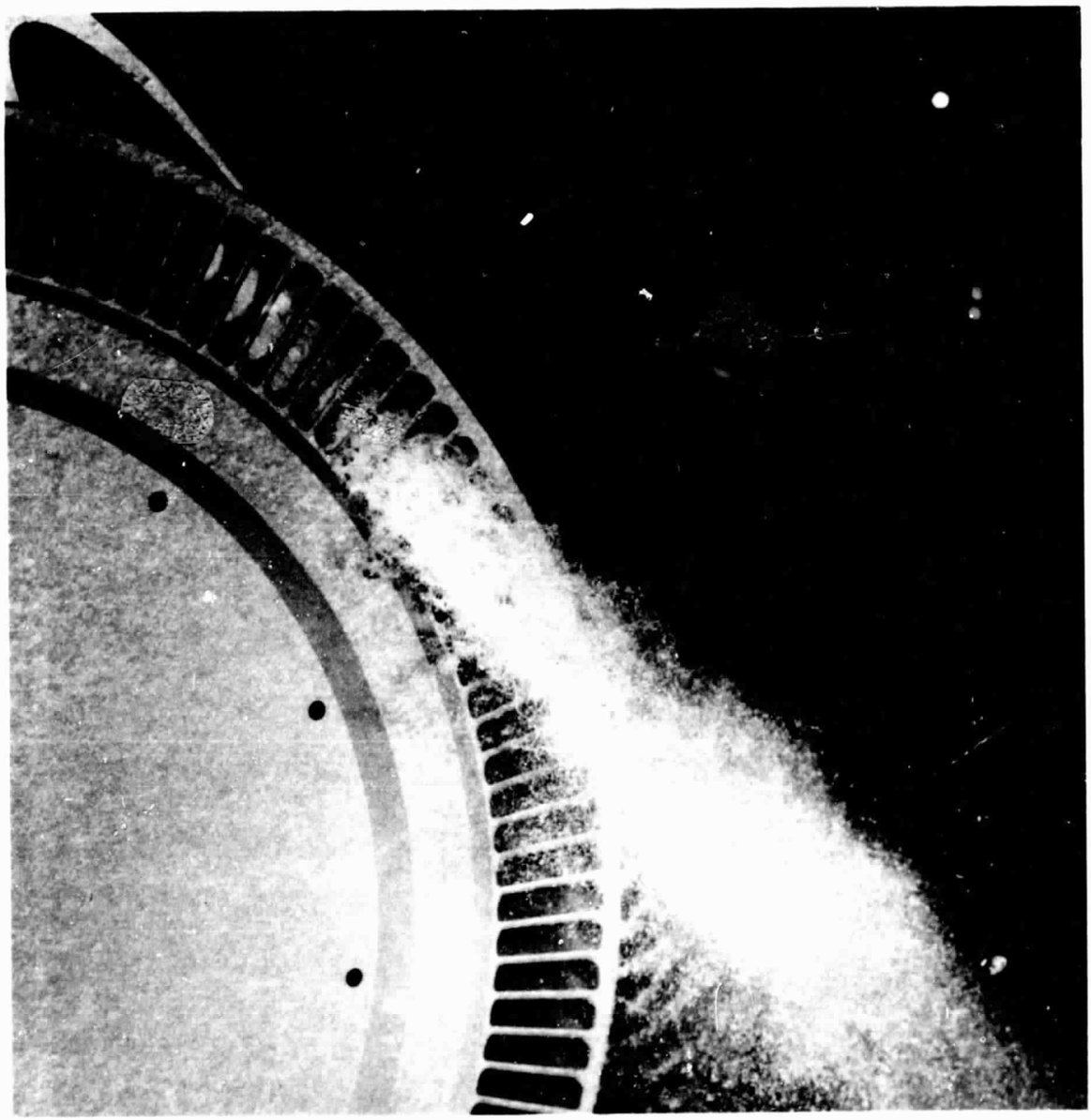

Fig. 31. Axial view of exit flow from Rotor 2

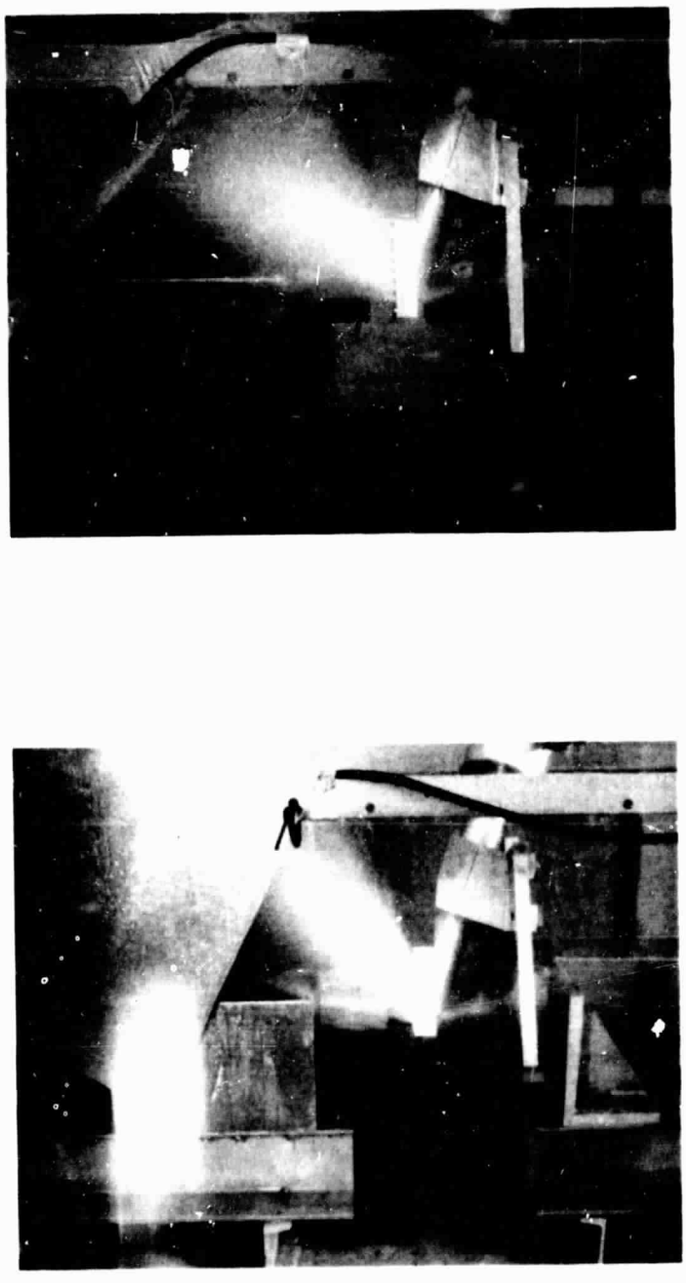

Fig. 32. Comparison of exit flow from flat and curved blades (zero blade speed): (a) flat contour; (b) curved contour

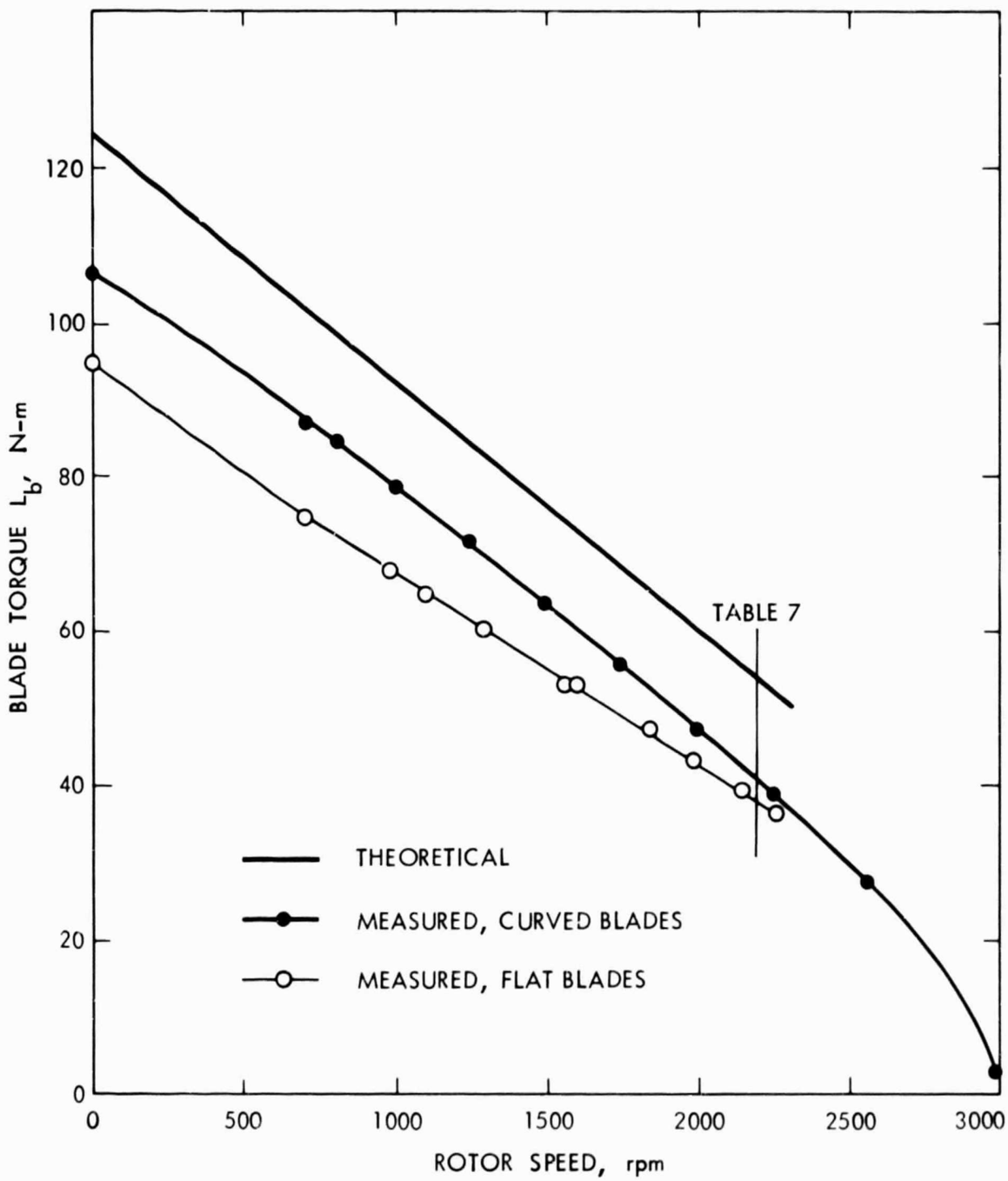

Fig. 33. Comparison of theoretical and experimental blade torques of Rotor 2

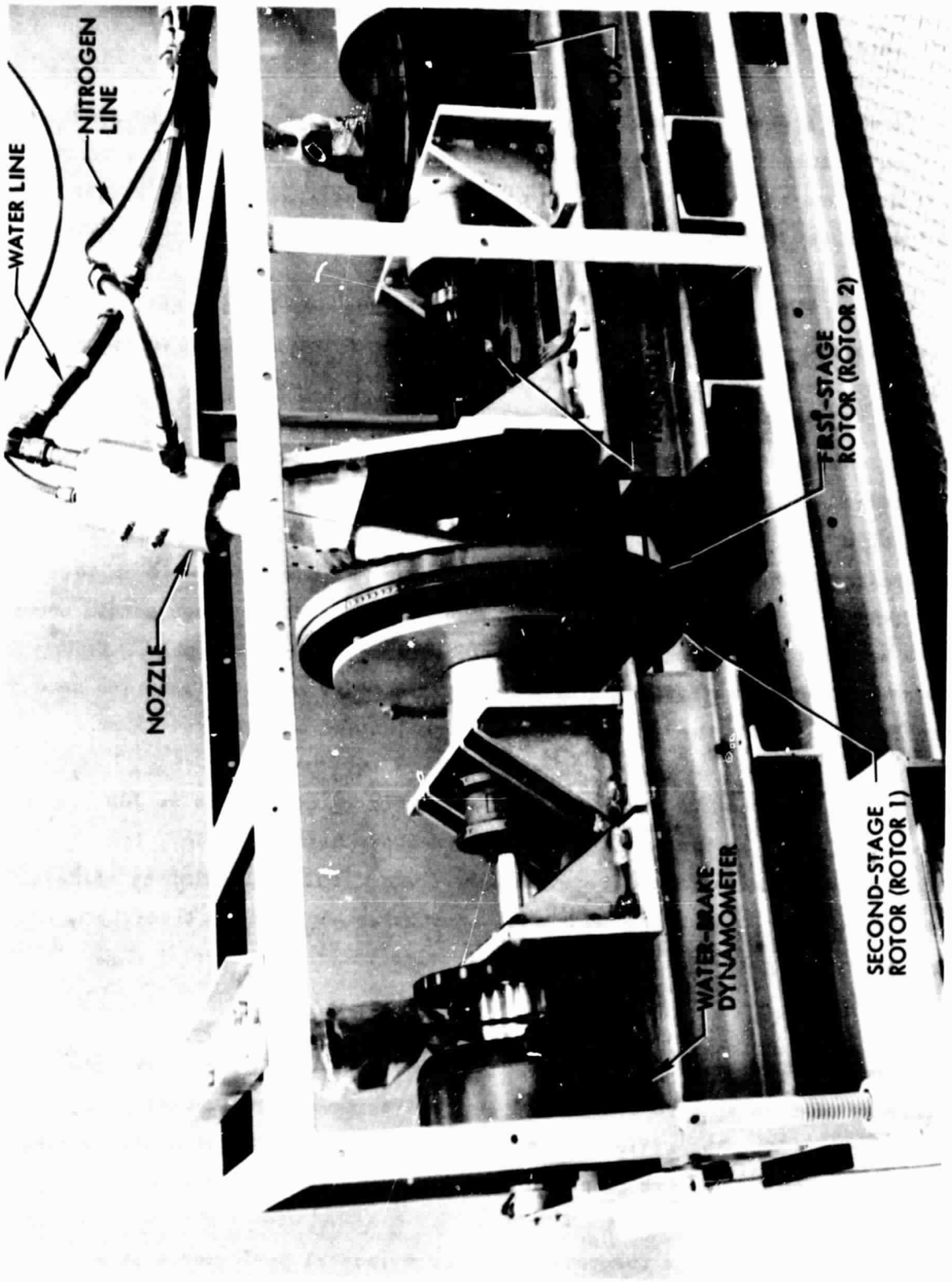

Fig. 34. Two-stage turbine

drive. The second stage (Rotor 1) is connected to a water-brake dynamometer. The right side of Rotor 1, as drawn in Fig. 17, faces the exit of Rotor 2. There is a gap of 0.5 mm between the rotors.

To make a test run, the first-stage rotor is set at the desired speed. The flow is turned on and the dynamometer water flow is adjusted to give the desired second-stage speed. The torque of the first stage and the torque on the dynamometer are recorded, together with the rotor speeds.

Windage torque is measured separately with the nozzle flow off. The windage torque exerted on the second stage by the first stage is sufficient to rotate the second stage for these measurements.

The nozzle position can be adjusted radially and tangentially, and there is an optimum position for maximum total shaft power. Figure 35 shows the effect of moving the nozzle. The best radial position is R_b = 261 mm, at which position the nozzle exit ellipse is tangent to the outer wall of the blade passages, as shown in the sketch. The maximum second-stage torque occurs with a nozzle displacement 8 mm to the right of center (x = -8 mm), but the first-stage torque is low. The highest-power combination of first- and second-stage torque is with the nozzle located 25 mm left of center (x = 25 mm).

In Fig. 36, the theoretical second-stage torque curve ends at 700 rpm where impingement on the backs of the second-stage blades begins. The theoretical torque is calculated using the theoretical exit velocity of the first-stage rotor. Because the measured torque is higher than theoretical, the absolute exit velocity from the first-stage rotor is evidently higher than theoretical.

Figure 37 presents the efficiency of the two-stage turbine. The blade efficiency of 0.56 at zero second-stage speed represents the output of the first-stage rotor. The efficiency reaches a maximum of 0.70 at a second-stage speed of 750 rpm. The peak theoretical efficiency is 0.85.

Table 7 compares the theoretical and experimental performance at a second-stage rotor speed of 678 rpm. The experimental windage torques are several times higher than theoretical but have the right sign (positive, or

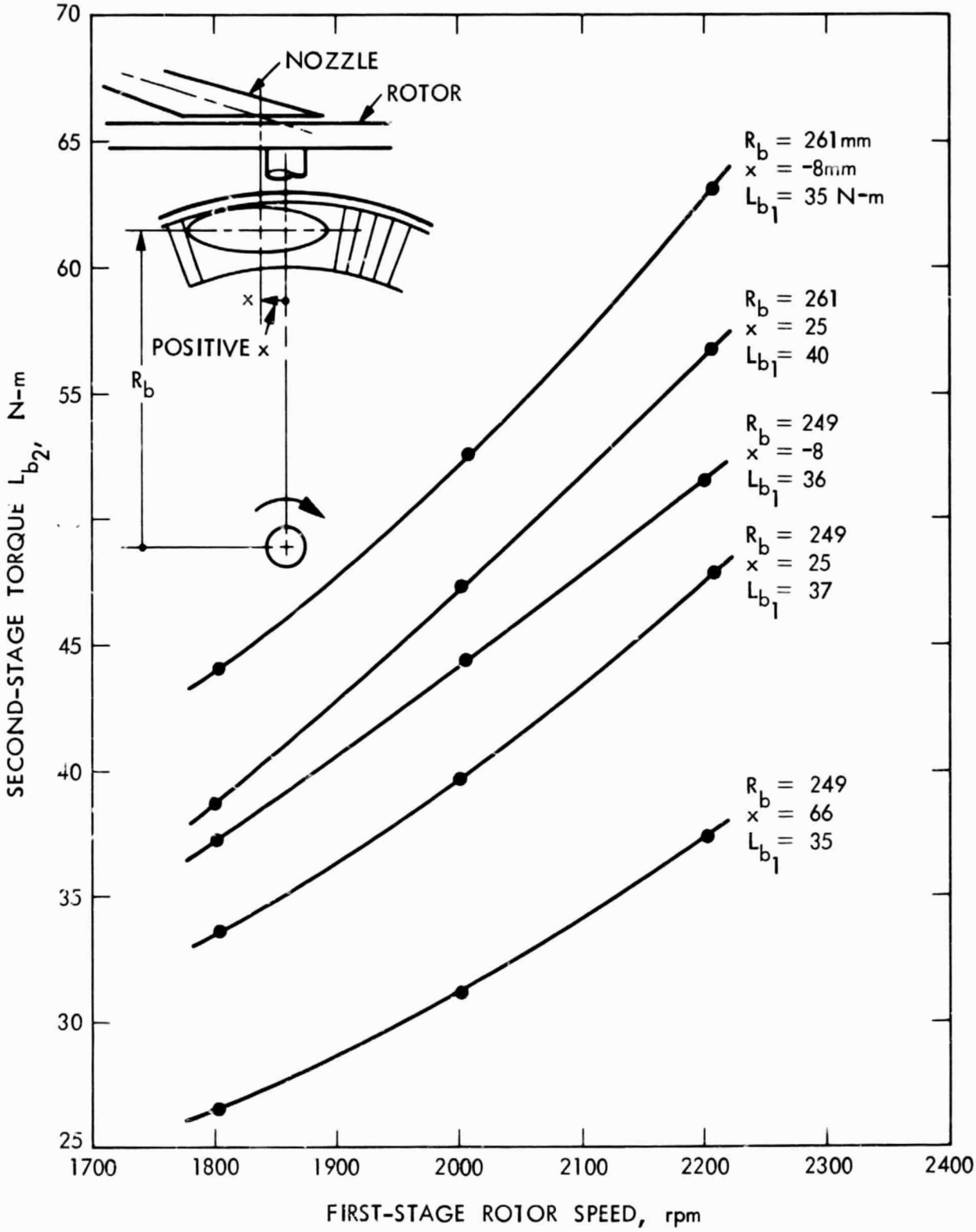

Fig. 35. Effect of nozzle position on second-stage zero-speed torque at 2200-rpm first-stage speed

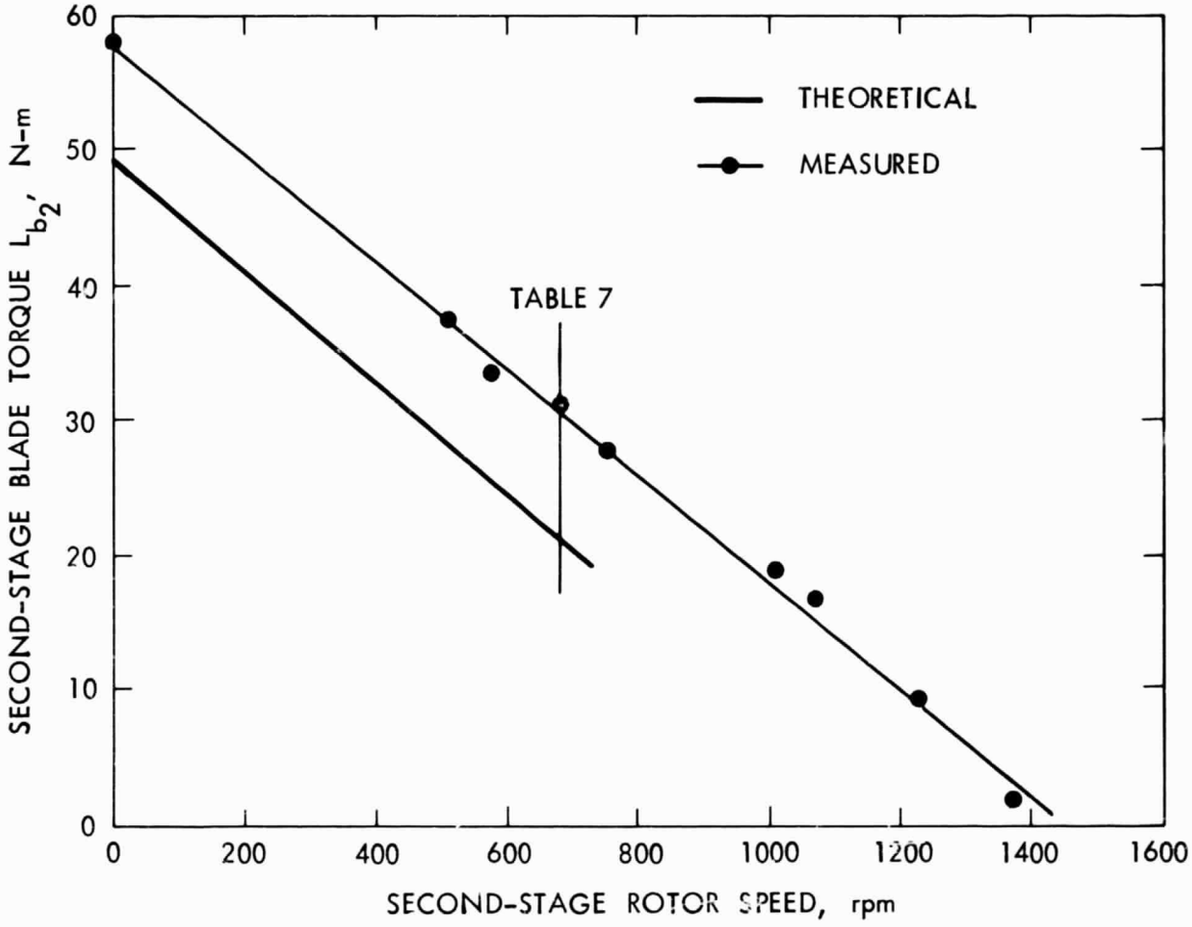

Fig. 36. Comparison of theoretical and experimental second-stage torques of two-stage turbine at 2200-rpm first-stage speed

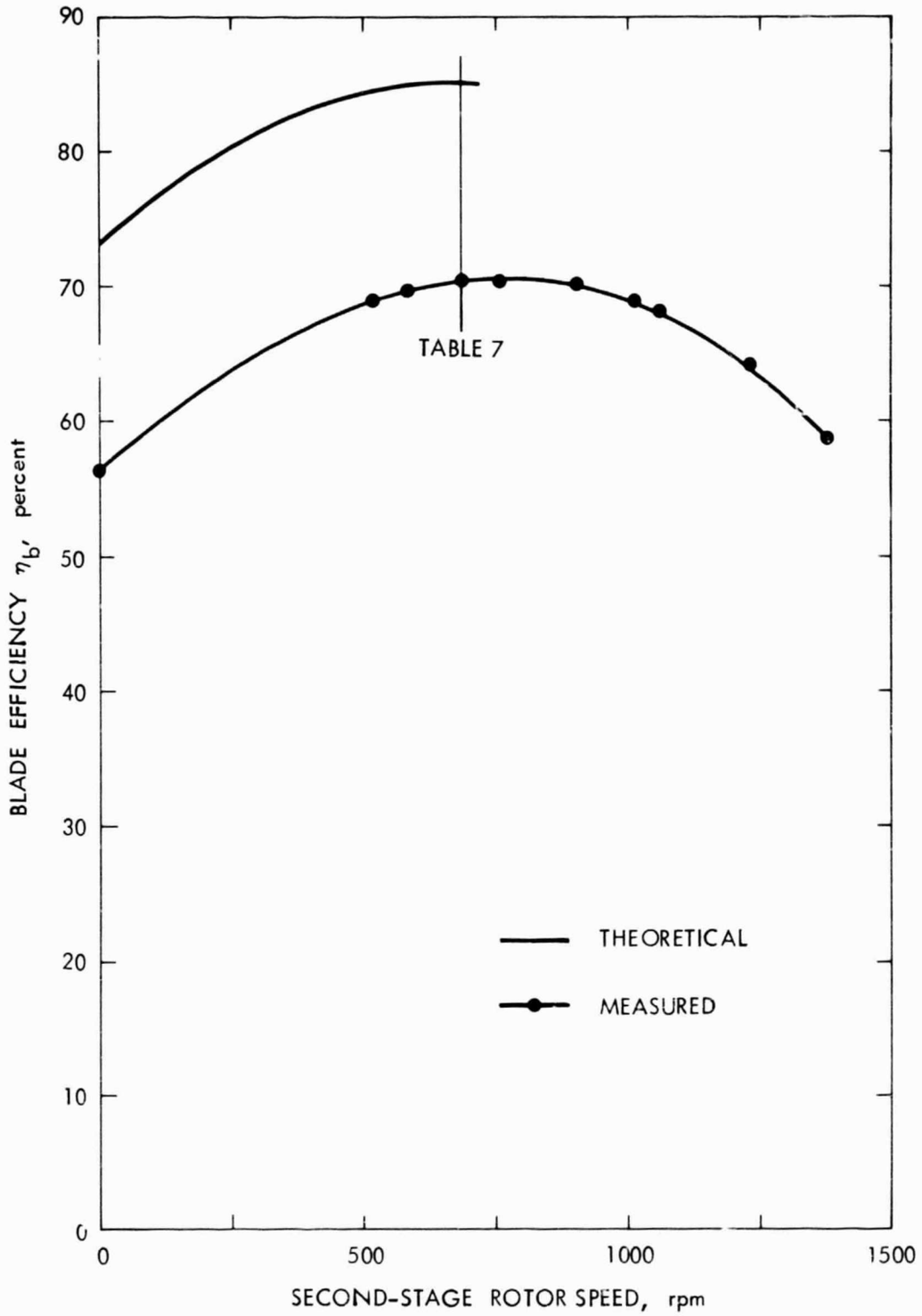

Fig. 37. Comparison of theoretical and experimental efficiencies of two-stage turbine at 2200-rpm first-stage speed

Table 7. Comparison of theoretical and experimental two-stage turbine performance (Table 1 nozzle conditions)

Item	Experimental			Theoretical		
	First stage	Second stage	Total	First stage	Second stage	Total
Nozzle angle, A_n, deg	20			20		
Rotor radius, R_b, mm	261	261		261	261	
Rotor speed, N, rpm	2200	678		2200	678	
Rotor torque, L_r, N-m	35.5	33.6		53.0	21.4	
Windage torque, L_w, N-m	4.5	-2.4		0.5	-0.2	
Blade torque, L_b, N-m	40.0	31.2		53.5	21.2	
Rotor power, P_r, kW	8.18	2.39	10.57	12.21	1.52	13.73
Blade power, P_b, kW	9.22	2.22	11.44	12.33	1.51	13.84
Rotor efficiency, η_r			0.648			0.841
Blade efficiency, η_b			0.701			0.848
Nozzle-blade efficiency, η_{nb}			0.549			0.664
Turbine efficiency, η_t			0.507			0.659
Relative inlet velocity, V_1, m/s				42.5	21.3	
Relative exit velocity, V_3, m/s				31.3	8.8	

retarding, for the first stage and negative, or accelerating, for the second stage). The turbine efficiency is 0.51 experimentally and 0.66 theoretically. Although the measured turbine efficiency is not as high as that for the single-stage Refrigerant-22 turbine because of the lower nozzle efficiency, the blade and rotor efficiencies are the highest that have been achieved so far with a two-phase turbine.

L. Divergence and Stagnation Losses

An additional source of loss not included in the theoretical torques and efficiencies is the radial spreading of the flow leaving the blades. To see the spreading better, a single blade was tested in the apparatus shown in Fig. 38. Sheet-metal blades similar in shape to those of Rotor 2 (flat contour) were held in a frame. A scoop collected the flow leaving all but the last blade. The flow passing behind the last blade continued on undisturbed except where it hit the support frame.

Figure 38(b) shows the spreading of the liquid sheet leaving the test blade. The exit flow consisted of a central sheet of small divergence angle and an outer fan on each side having about a 45-deg divergence angle.

The effect of the spreading exit flow is to reduce the circumferential component of the exit velocity by the cosine of some average divergence angle. In the rotor program, the relative exit velocity is denoted V_3. A corrected exit velocity V_3' can be obtained by specifying a divergence angle A_{div} such that

$$V_3' = V_3 \cos A_{div} \tag{25}$$

The theoretical zero-speed torque of Rotor 1 in the single-stage tests (Fig. 24) can be brought down to the measured torque by using a divergence angle A_{div} of 30 deg. For Rotor 2 (Fig. 33), a divergence angle of 30 deg lowers the theoretical zero-speed torque from 124 N-m to 119 N-m, whereas the measured zero-speed torque is only 108 N-m. However, as was seen from Fig. 32, the angle of discharge of the liquid is less than the 60-deg exit angle of the blades. A line drawn through the estimated center of the exit flow in

(a)

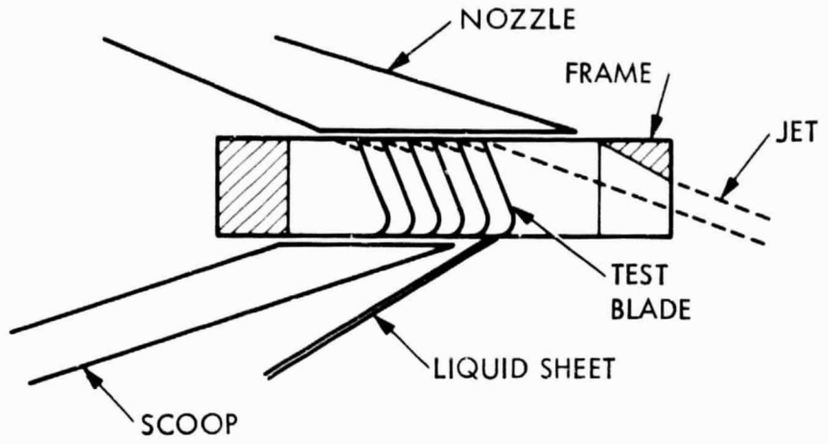

(b)

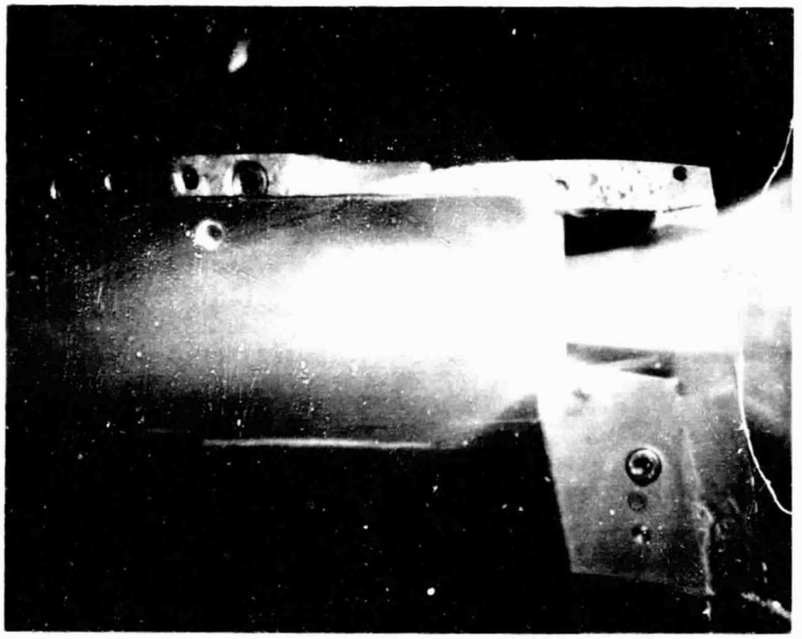

Fig. 38. Exit flow from a single blade: (a) apparatus; (b) flow test

Fig. 32(b) has an angle of only 40 deg above horizontal. If it is assumed that the liquid is leaving at 40 deg instead of 60 deg and is also spreading at an average divergence angle of 30 deg, then the theoretical zero-speed torque is reduced to 111 N-m, close to the measured value.

A second loss not included in the theory is the stagnation and trapping of a portion of the liquid in the rotor. Observing a rotor in operation, it can be seen that some liquid continues to leave the rotor long after the rotor has passed through the jet. This effect can be seen in Fig. 39, which is a 1-μs flash photograph of the flow leaving Rotor 2 at 2250 rpm. Streamers of water leave the outer wall of each blade passage after the rotor passes the jet. These streamers persist for about 90 deg of rotation.

Further details of the main flow and the delayed stagnated flow can be seen in Fig. 40. An arm with four blades machined in the shape of those in Rotor 2 (flat blade contour) was rotated through the jet at 2200 rpm and photographed at seven successive positions. At the top position, the blades are just starting to enter the flow. In position 2, the liquid sheets are starting to emerge. In positions 3 and 4, the behavior of the flow that passes straight through the rotor can be seen most clearly: liquid is scooped out of the jet, moved to the near side of the rotor, and released to continue on in its original direction at reduced speed.

In position 5, it can be seen that some liquid has remained with the rotor. In positions 6 and 7, this stagnated liquid continues to drain toward the outer walls of the blade passages and spin off, leaving the rotor at full rotor speed.

The amount of liquid leaving the rotor in the main jet was measured by placing a scoop over the exit jet leaving Rotor 2. The outline of the scoop is shown in Fig. 41. The scoop collected 1.2 kg/s of water when the nozzle water flow rate was 1.7 kg/s. The collected flow rate was constant for rotor speeds from 1250 rpm to 2200 rpm. Thus, 0.5 kg/s of water, or 30 percent of the flow, was missing from the main exit jet. Further measurements, obtained by moving the scoop, showed that, of this 0.5 kg/s, 0.24 kg/s was thrown off the rotor in the first 30 deg of rotation beyond the jet, 0.07 kg/s was

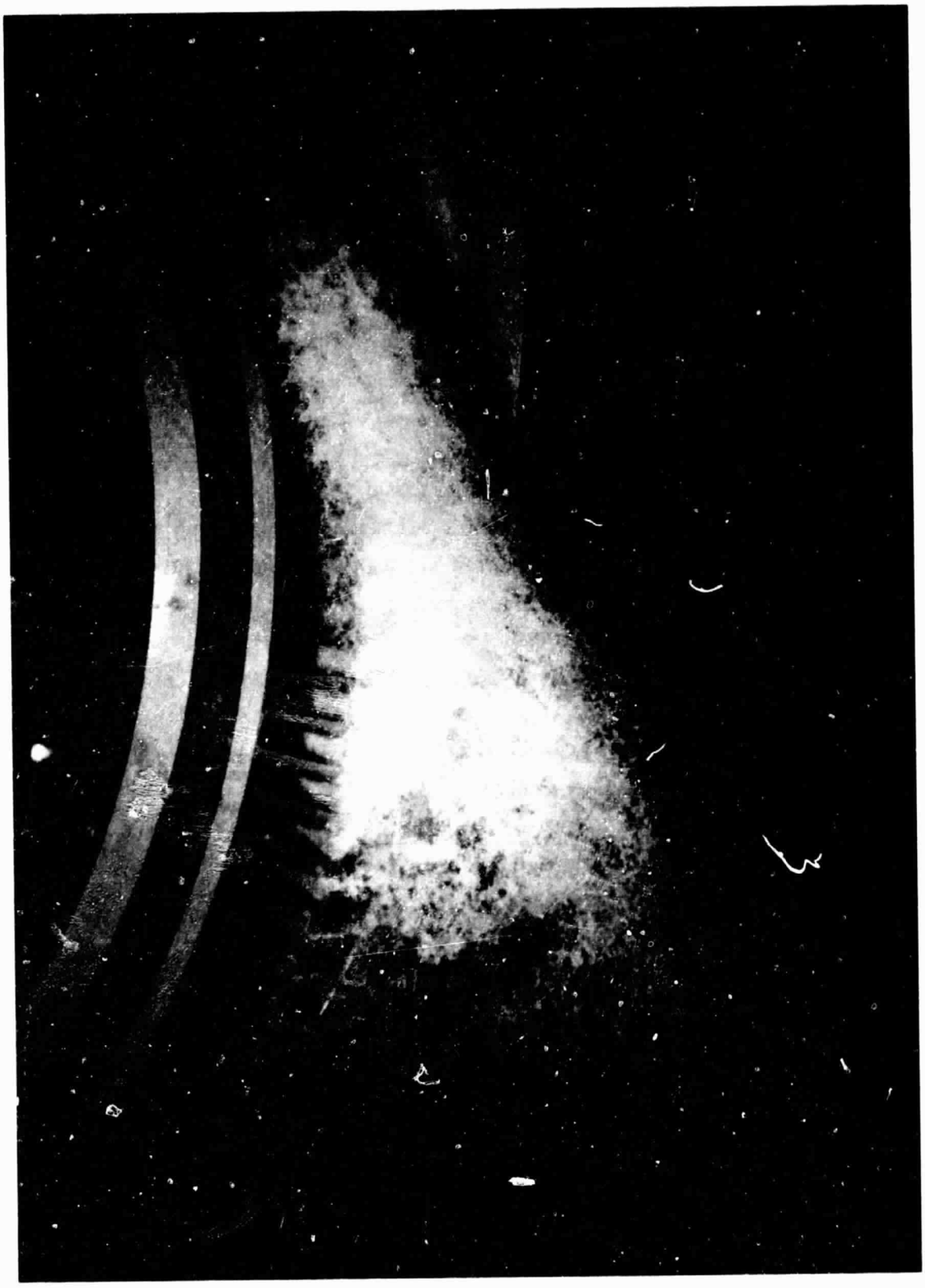

Fig. 39. Exit jet and delayed drainage flow from Rotor 2

ORIGINAL PAGE
BLACK AND WHITE PHOTOGRAPH

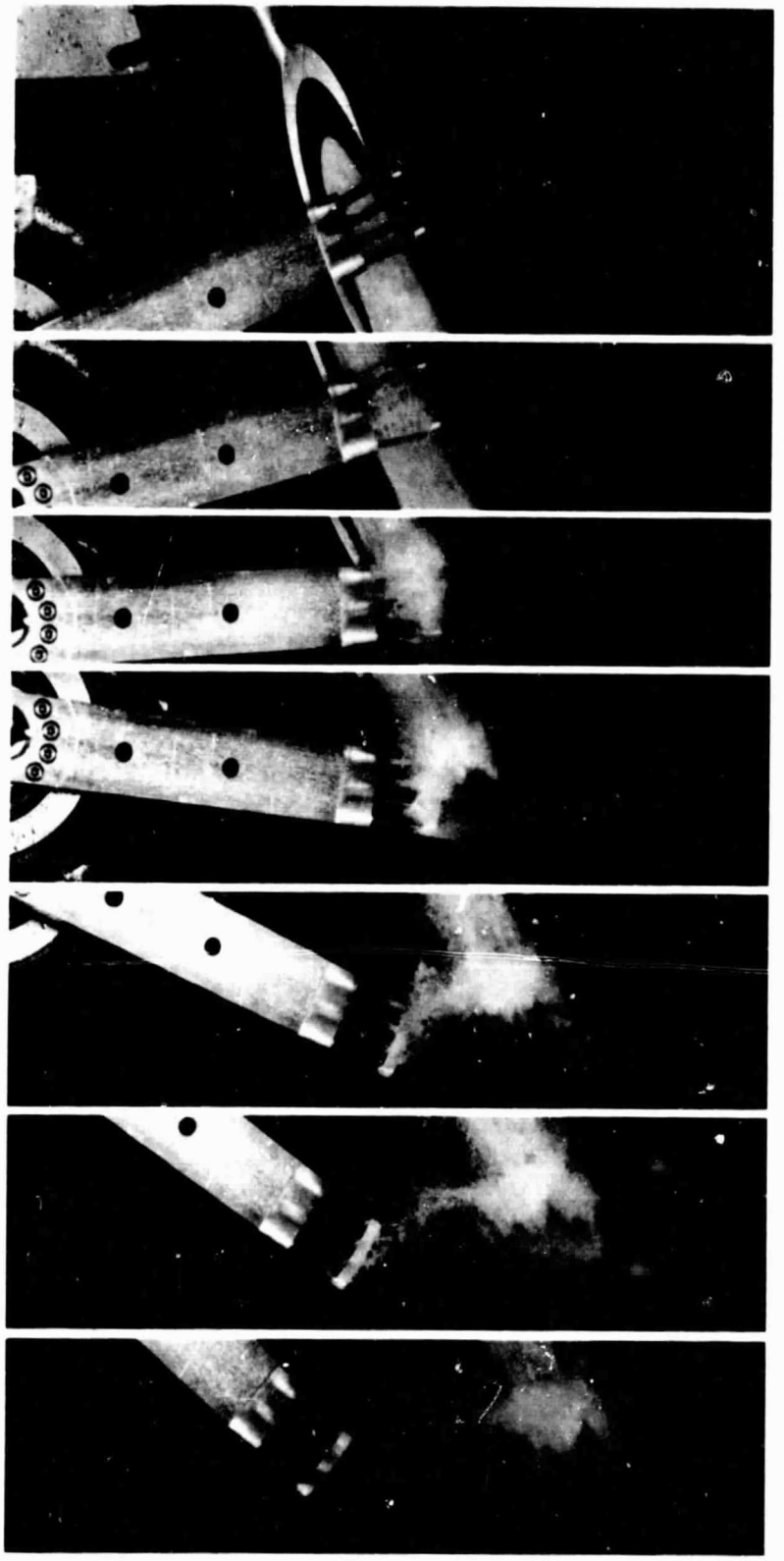

1 - BLADES ENTER JET.

2 - FLOW REACHES BLADE EXIT.

3 - MAIN FLOW LEAVES BLADES.

4 - MAIN FLOW CLEARS BLADES

5 - MAIN FLOW CONTINUES IN DIRECTION OF JET. STAGNATED FLOW STARTS TO DRAIN FROM ROTOR

6 - STAGNATED FLOW IS THROWN OFF AT ROTOR SPEED

7 - STAGNATED FLOW CONTINUES TO DRAIN FOR 90 DEG OF ROTATATION

Fig. 40. Exit flow from bladed arm

Fig. 41. Rotor 2 exit scoop for flow measurement

thrown off in the next 90 deg, 0.05 kg/s was thrown off the rotor on the nozzle side near the nozzle, and 0.14 kg/s was thrown off the rotor around the remaining circumference.

If, in addition to the exit divergence effect, 25 percent of the flow is considered to be stagnated in the rotor and thrown off at rotor speed, the theoretical torque of Rotor 2 at 2200 rpm is decreased from 54 N-m to 40 N-m, in agreement with the data. Thus, the flow stagnation effect, combined with the exit flow divergence effect, is sufficient to account for the difference between theoretical and experimental torques.

A major improvement in blade efficiency (from 0.70 to 0.85 for the two-stage water-and-nitrogen turbine) would be possible if the stagnation and divergence effects could be eliminated. This might be possible with more complex blade shapes. On the other hand, the undesired effects might reflect fundamental secondary-flow phenomena that cannot be avoided. Further study of these effects should be the next direction of research.

M. Separator Turbine Concept

The separator turbine (Refs. 3, 6, 7) is an alternative to the multistage impulse turbine for overcoming the friction problem of two-phase flow. The problem, in essence, is that the large flow area required by the gas phase requires large blade areas that are subjected to the large shear of the liquid phase. The multistage impulse turbine attacks this problem by reducing the relative velocity between the liquid and the blades, thus reducing the shear. The separator turbine attacks the problem by separating out the gas phase, thus reducing the required blade area.

Figure 42 shows the basic arrangement of a separator turbine. The two-phase jet impinges on the inside wall of a rotary separator, causing the liquid to separate out as a liquid layer inside the separator drum. Ideally, the separator drum has the same speed as the jet.

A second rotor, the liquid turbine, is positioned concentrically within the rotary separator. The liquid turbine carries one or more U-tube scoops

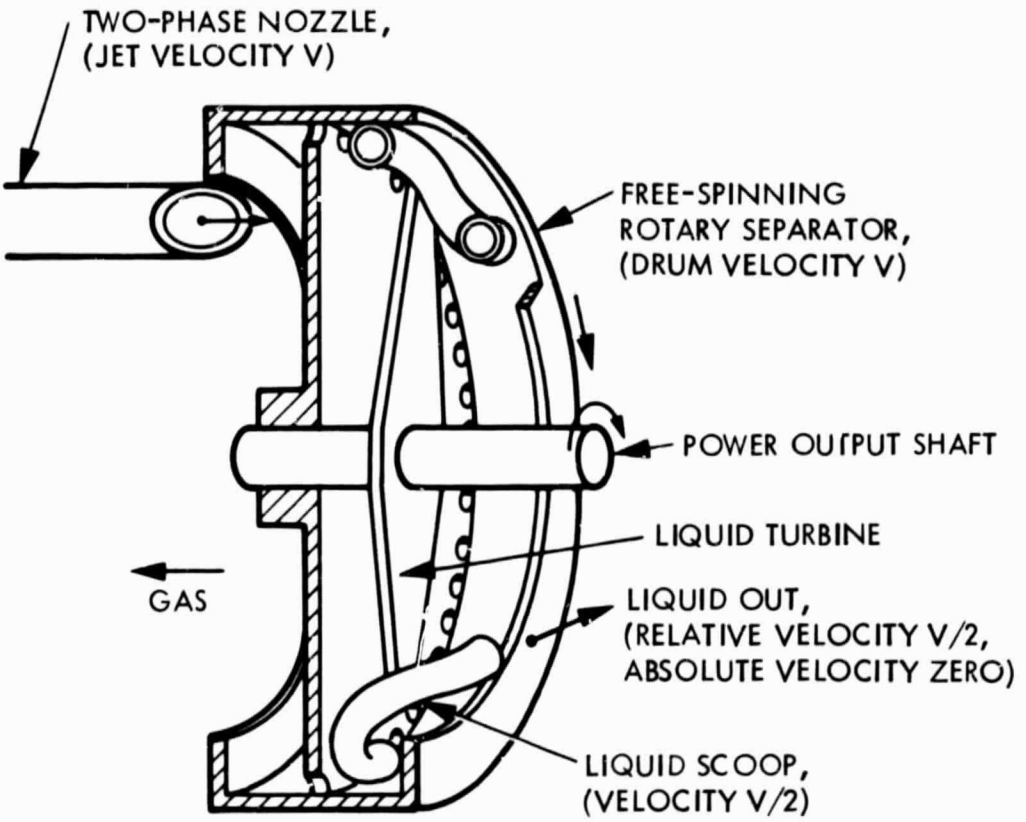

Fig. 42. Separator turbine

with their inlets immersed in the liquid layer. The liquid enters the U-tubes and is discharged in the opposite direction.

If the U-tubes travel at half the speed of the separator drum, the absolute velocity of the liquid leaving the U-tubes is zero. All of the kinetic energy of the liquid has been converted to shaft power of the liquid turbine. The gas leaving the rotary separator can, in principle, be sent through a gas turbine to recover the gas kinetic energy.

In another variation of the separator turbine, the U-tubes can be replaced by diffusers that feed the liquid to a hollow shaft in the liquid turbine. If the liquid turbine is run at a speed less than half that of the separator drum, the liquid leaving the shaft will be pressurized. At the proper speed, the liquid can be returned to the two-phase nozzle, and the shaft power output will have been reduced by an amount equal to the pumping power for the liquid return.

In principle, the only fluid friction in the separator turbine is in the U-tubes. Since the U-tubes carry only liquid, not two-phase flow, the wall area is small and the friction loss is reduced accordingly.

In practice, there is also impact loss of the two-phase jet entering the separator; this loss consists of radial impact on the separator drum and axial impact on the rear wall. There is also external drag on the U-tubes immersed in the liquid layer, and windage loss. Appendix B presents the theory of separator turbines, taking these losses into account.

When the separator turbine theory is applied to specific cases, the theoretical efficiency of a separator turbine is no greater than the theoretical efficiency of a single-stage bladed turbine. Figure 43 compares the rotor efficiencies of separator turbines and bladed turbines for a particular steam-and-water mixture. The efficiency of the two-stage impulse turbine is plotted as a function of first-stage rotor speed. The efficiency of the separator turbine is plotted against liquid turbine speed; the separator speed is about twice as great. The efficiency of the liquid turbine is assumed to be very high: 0.9.

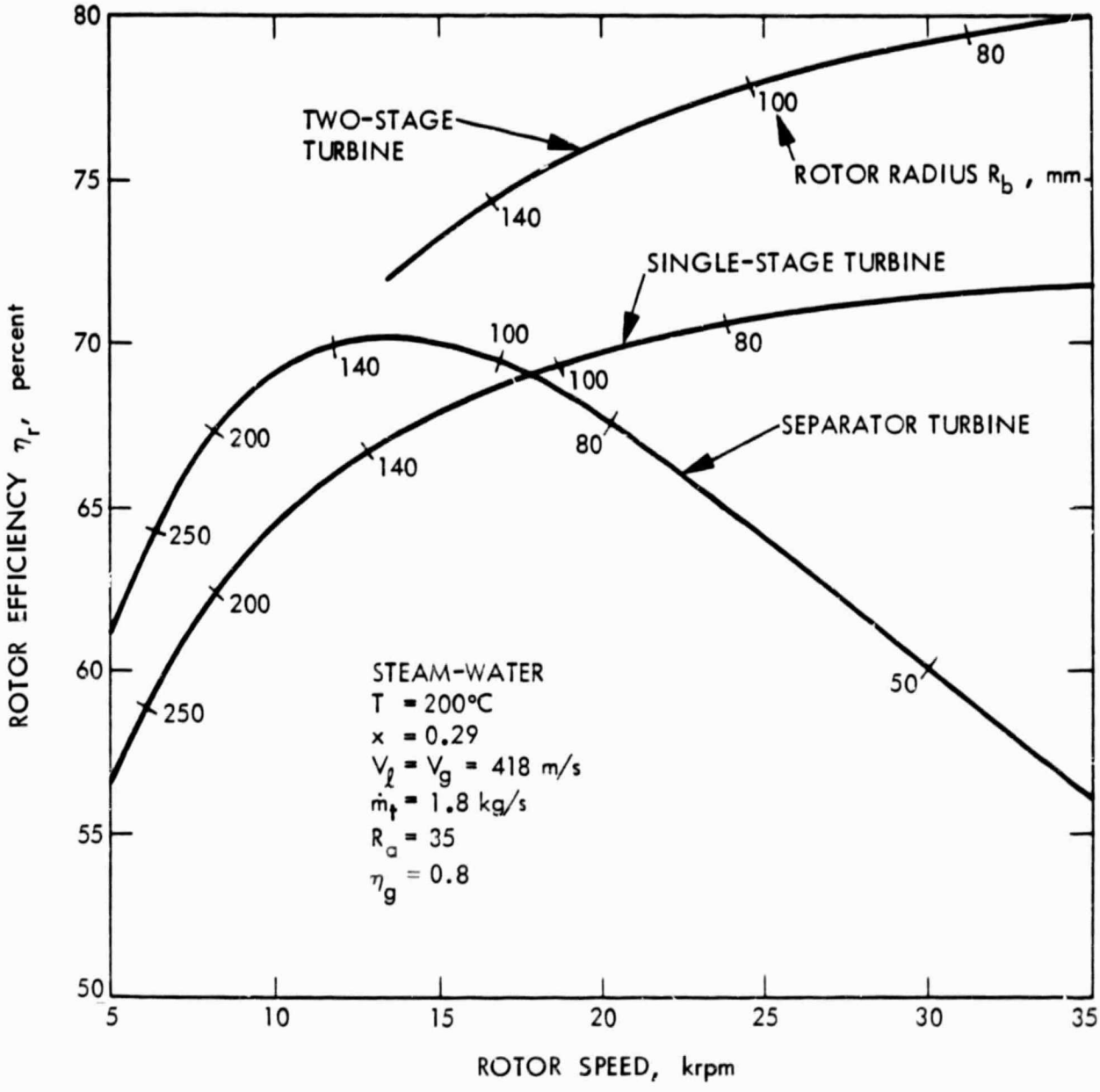

Fig. 43. Comparison of efficiencies of impulse turbine and separator turbine

At large diameters, the separator turbine is superior to the single-stage impulse turbine because the jet enters the separator with relatively small impact loss, and the assumed U-tube turbine efficiency is higher than the efficiency of the bladed turbine. However, at these large diameters, the windage loss is large. At the other end of the curve, at small diameters, the windage loss of the separator turbine is small, but the impact losses in the separator are large. The peak efficiency of the separator turbine is achieved at a liquid turbine speed of 14,000 rpm (separator speed of 23,000 rpm).

The basic concept of reducing friction by reducing liquid shear area is a valid approach, but it is not clear how to build a low-loss separator to implement the concept.

N. Turbine Performance Examples

The nozzle program, coupled with the rotor program, gives a reasonable prediction of two-phase turbine efficiency. The nozzle program gives nozzle efficiencies that are slightly too low, but the rotor program errs in the other direction. It is of interest to see what these programs predict in practical cases.

A geothermal steam-water or "total-flow" turbine has been one of the applications of interest. The theoretical performance of a 5-MW turbine at the flow conditions studied by LLL is presented in Table 8. The flow conditions are taken from Table 1 of Ref. 13.

The nozzle program predicts a nozzle efficiency of 0.89 for nozzles of 1.0-m length. For full admission, 15 nozzles are mounted around the circumference of a rotor of 0.7-m radius and 0.1-m blade height. A single-stage turbine operates at 3600 rpm and has a rotor efficiency of 0.65; the turbine efficiency is 0.58. The turbine efficiency increases to 0.63 with two stages and to 0.66 with three stages.

C - 2

Table 8. Theoretical performance of 5-MW steam-and-water turbine (LLL design conditions)

Item	Value
Nozzle inlet	
Temperature, T_1, ^{o}C	223.5
Pressure, p_1, kPa	2482
Flow rate, $\dot{m}_t$, kg/s	30.0
Quality, x_1	0.189
Nozzle exit	
Pressure, p_2, kPa	12.4
Temperature, T_2, ^{o}C	50.1
Drop diameter, d_2, μm	28
Gas density, ρ_g, kg/m^3	0.084
Area, A_2, m^2	0.144
Quality, x_2	0.357
Isentropic velocity, V_i, m/s	742
Isentropic power, P_i, MW	8.258
Mean velocity, $\bar{V}$, m/s	681
Liquid velocity, V_ℓ, m/s	564
Gas velocity, V_g, m/s	891
Jet power, P_{jet}, MW	7.319
Nozzle efficiency, η_n	0.886
Flow area ratio, R_a	4150
Rotors	
Radius, R_b, m	0.70
Blade height, H_b, m	0.10
Gas-phase torque factor, η_g	0.80

Table 8 (contd)

Item	Value
Single-stage turbine	
Rotor speed, N, rpm	3600
Relative inlet velocity, V_1, m/s	329
Rotor power, P_r, MW	4.776
Rotor efficiency, η_r	0.653
Turbine efficiency, η_t	0.579
Two-stage turbine	
First-stage rotor speed, N_1, rpm	4770
Second-stage rotor speed, N_2, rpm	2320
First-stage relative inlet velocity, V_1, m/s	264
Rotor power, P_r, MW	5.209
Rotor efficiency, η_r	0.712
Turbine efficiency, η_t	0.631
Three-stage turbine	
First-stage rotor speed, N_1, rpm	5390
Second-stage rotor speed, N_2, rpm	3530
Third-stage rotor speed, N_3, rpm	1770
First-stage relative inlet velocity, V_1, m/s	235
Rotor power, P_r, MW	5.426
Rotor efficiency, η_r	0.741
Turbine efficiency, η_t	0.657

The goal of the LLL program was a turbine efficiency of 0.70; this does not appear to be attainable with steam-and-water mixtures.

A higher efficiency can be achieved by using an organic working fluid and transferring the heat from the geothermal fluid in a binary cycle. Table 9 presents the theoretical performance of a turbine using Refrigerant 113 (at conditions that correspond to a geothermal fluid of lower temperature and quality than those for the steam-and-water turbine of Table 8).

The turbine efficiency is 0.67 with one stage, 0.71 with two stages, and 0.72 with three stages. Part of the improvement in efficiency with Refrigerant 113 is due to the larger nozzle exit quality (0.64 instead of 0.36), giving higher weight tc the assumed gas-phase torque factor of 0.8. However, the liquid-phase blade efficiency is also improved.

The results of the comparison shown in Fig. 44 are typical of what might be achieved ultimately with two-phase turbines. Single-stage turbines with unfavorable working fluids such as water and steam will have efficiencies limited to the mid-50-percent range. Multistage turbines with more favorable working fluids might achieve efficiencies in the 70-percent range. Depending on the thermodynamic and practical gains offered by two-phase cycles in a particular case, such turbine efficiencies may be sufficient for useful applications.

Table 9. Theoretical performance of 5-MW Refrigerant-113 turbine

Item	Value
Nozzle inlet	
Temperature, T_1, ^{o}C	149
Pressure, p_1, kPa	1196
Flow rate, m_t, kg/s	460
Quality, x_1	0.01
Nozzle exit	
Pressure, p_2, kPa	97
Temperature, T_2, ^{o}C	46
Drop diameter, d_2, μm	23
Gas density, ρ_g, kg/m^3	7.18
Area, A_2, m^2	0.237
Quality, x_2	0.641
Isentropic velocity, V_i, m/s	174.2
Isentropic power P_i, MW	6.979
Mean velocity, $\bar{V}$, m/s	168.6
Liquid velocity, V_ℓ, m/s	158.0
Gas velocity, V_g, m/s	174.5
Jet power, P_{jet}, MW	6.551
Nozzle efficiency, η_n	0.939
Flow area ratio, R_a	340
Rotors	
Radius, R_b, m	0.89
Blade height, H_b, m	0.13
Gas-phase torque factor, η_g	0.80

Table 9 (contd)

Item	Value
Single-stage turbine	
Rotor speed, N, rpm	830
Relative inlet velocity, V_1, m/s	89
Rotor power, P_r, MW	4.686
Rotor efficiency, η_r	0.715
Turbine efficiency, η_t	0.671
Two-stage turbine	
First-stage rotor speed, N_1, rpm	1090
Second-stage rotor speed, N_2, rpm	435
First-stage relative inlet velocity, V_1, m/s	72
Rotor power, P_1, MW	4.947
Rotor efficiency, η_r	0.755
Turbine efficiency, η_t	0.709
Three-stage turbine	
First-stage rotor speed, N_1, rpm	1237
Second-stage rotor speed, N_2, rpm	638
Third-stage rotor speed, N_3, rpm	302
First-stage relative inlet velocity, V_1, m/s	63
Rotor power, P_r, MW	5.055
Rotor efficiency, η_r	0.772
Turbine efficiency, η_t	0.725

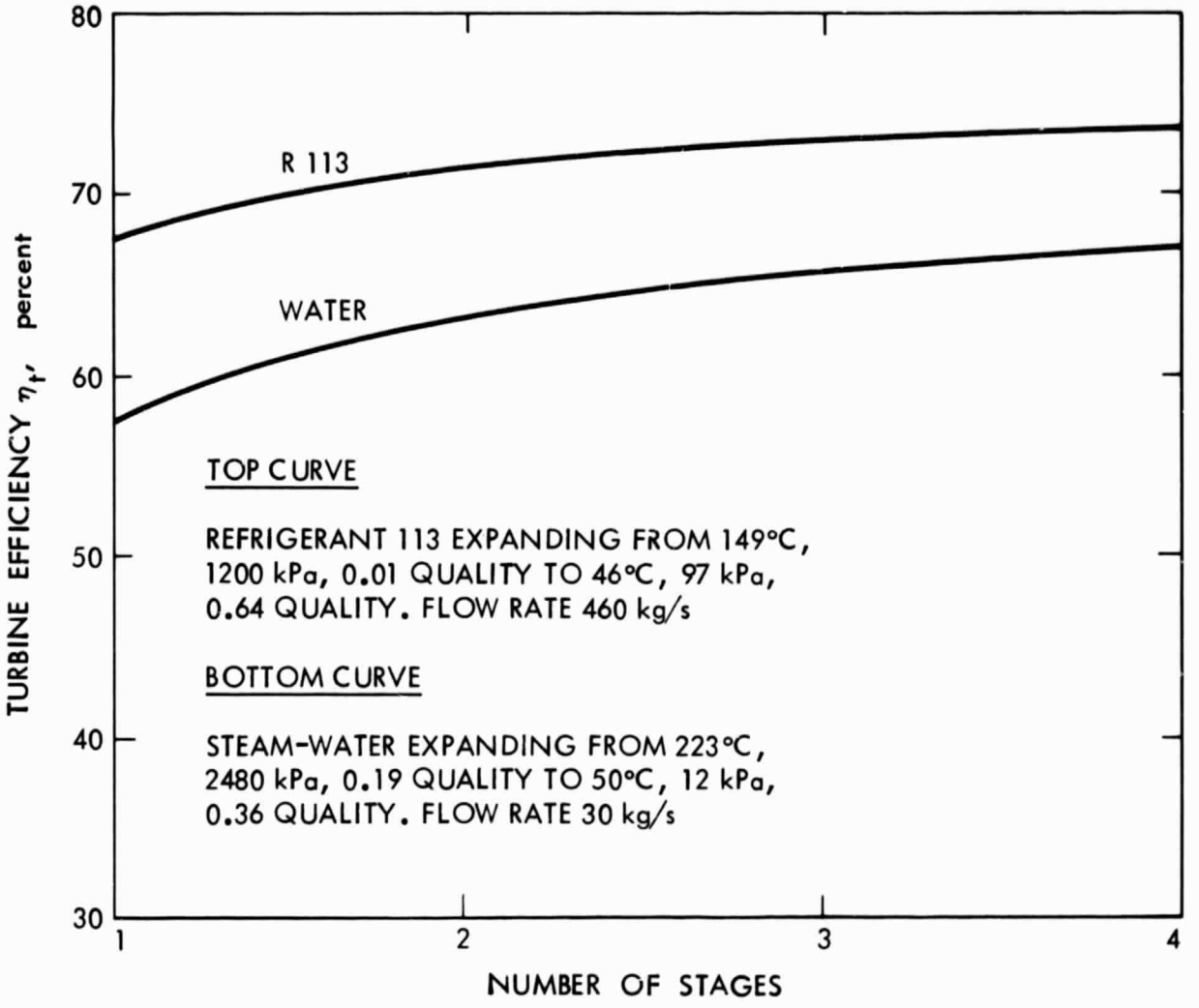

Fig. 44. Theoretical efficiences of 5-MW steam-and-water and Refrigerant-113 turbines

VI. CONCLUSION

Conclusions can be drawn in two areas: analysis capability for two-phase turbines and, to a lesser extent, practical usefulness of two-phase turbines.

A. Analysis Capability

The JPL two-phase nozzle program calculates velocities that are within 2 to 4 percent of measurements, but the corresponding efficiency error is 4 to 8 percent. The predicted velocities are lower than measured, probably due to overestimation of drop size. A more sophisticated drop size routine is needed. As an expedient, the critical Weber number could be reduced to a lower number, such as 3, that would fit existing data.

The rotor program derived in Appendix A gives an upper performance limit. Combined with the nozzle program, it probably shows the best that can be achieved with any given working fluid and operating condition.

The measured rotor efficiencies have been 10 to 15 percent below the calculated values. The cause appears to be flow stagnation and divergence effects. It is not known if these losses can be reduced or if they are fundamental limitations.

B. Application Prospects

The efficiency of single-stage two-phase turbines will be only about 50 percent, but this is sufficient for replacing the throttling steps in geothermal plants, refrigeration systems, and other systems that use irreversible flashing processes. A two-phase turbine would add power in these applications no matter how inefficient the turbine. However, the value of the added energy output must at least equal the cost of the turbine and associated equipment for the turbine to be economic. This requirement keeps many new energy devices from use, and is a stumbling block for two-phase turbines as well.

For applications where the two-phase turbine must compete with vapor turbines, there is a difficult efficiency requirement. The efficiency advantage of a two-phase cycle, say for waste-heat recovery or geothermal power where the two-phase cycle improves the matching to the heat source, is only about 15 percent. The efficiency of vapor turbines is about 80 percent. Therefore, a two-phase turbine must have an efficiency of more than 65 percent to give a net gain in cycle efficiency. This is about the upper limit of efficiency for two-phase turbines, and is probably attainable only with organic working fluids. The picture that emerges is that two-phase turbines look promising in organic-fluid waste-heat or geothermal binary cycles where there is a significant thermodynamic advantage in using saturated liquid expansion and where the flow conditions are conducive to the best two-phase turbine efficiency. Two-phase turbines using steam and water expanding to the low pressures required in most applications such as geothermal may be ruled out by low efficiency and possibly erosion.

Perhaps the most attractive prospect for early use of two-phase turbines is the WD cycle where two-phase flow is used only in the nozzle and dry vapor is used in the rotor.

APPENDIX A.

ROTOR MODEL

A. Turbine Geometry

The behavior of the flow in a two-phase turbine rotor will be analyzed for the geometry shown in Fig. A-1.

A two-phase nozzle of width W_n and height H_n (equal if nozzle is circular) delivers flow at angle A_{noz} to rotor blades traveling at velocity V_b. The jet contains liquid of flow rate $\dot{m}_\ell$ traveling at velocity V_ℓ and gas of flow rate $\dot{m}_g$ traveling at velocity V_g.

The blades have an inlet section of shallow curvature where the flow impinges and an exit section of sharper curvature where the flow is turned. The inlet radius of curvature is R_1 and the exit radius of curvature is R_2. The blade ends with an optional straight extension of length L_{ext}.

A center plane can be drawn through the point where the blade surfaces pass through the axial direction. The blade inlet angle is A_1 and the blade exit angle is A_2, measured from the center plane. The inlet curvature R_1 ends at angle A_3 past the center plane.

The radius of the rotor at the center of the nozzle is R_b, and the outside radius of the rotor is R_w. The blade spacing at radius R_b is S_b.

The flow parameter that has the dominating effect on liquid friction loss is the ratio of gas flow area to liquid flow area R_a, which is found as follows: The flow area occupied by liquid at the nozzle exit is $\dot{m}_\ell/\rho_\ell V_\ell$, where ρ_ℓ is the liquid density. The gas flow area is R_a times the liquid area, and the total flow area is $(1 + R_a)$ times the liquid area. Equating the product of $(1 + R_a)$ and liquid flow area to the nozzle exit area $W_n H_n$ (treating the nozzle as rectangular), the gas/liquid area ratio is given by

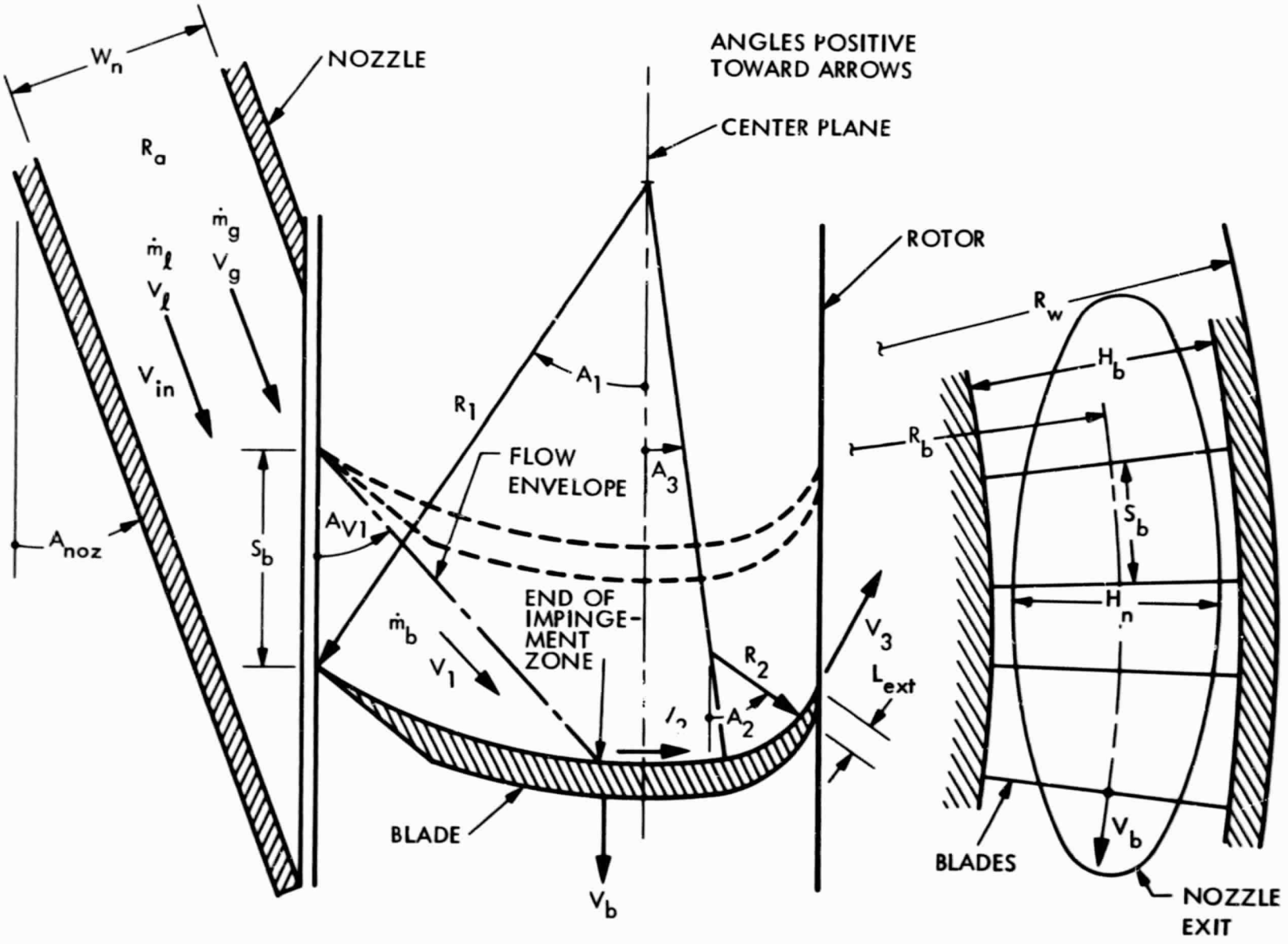

Fig. A-1. Two-phase turbine geometry

$$R_a = \frac{W_n H_n \rho_\ell V_\ell}{\dot{m}_\ell} - 1 \qquad \text{(A-1)}$$

The liquid flow rate $\dot{m}_b$ impinging on each blade is equal to the total liquid flow rate $\dot{m}_\ell$ times the fraction of the nozzle area intercepted by one blade passage. The nozzle has a projected width in the plane of the rotor equal to $W_n/\sin A_{noz}$. The fraction of the nozzle occupied by one blade passage is equal to the blade spacing S_b divided by this projected nozzle width. Hence, the liquid flow rate per blade is

$$\dot{m}_b = \frac{\dot{m}_\ell S_b \sin A_{noz}}{W_n} \qquad \text{(A-2)}$$

B. Inlet Velocity Vectors

Figure A-2 shows the velocity vectors for the liquid flow. Vectors are conveniently handled in the computer as complex numbers. A velocity V at angle A from the positive x axis forms a vector velocity $\vec{V}$. If the magnitude V and angle A are given, the vector can be computed as $\vec{V}$ = POLAR(V, A), where POLAR is a function that constructs a complex number having real part V cos A and imaginary part V sin A. Conversely, given a complex number $\vec{V}$, the magnitude and angle of $\vec{V}$ are given by V = ABS($\vec{V}$) and A = PHASE($\vec{V}$), respectively, where ABS and PHASE are functions that operate appropriately on the complex number $\vec{V}$. (Angles are in degrees in the computer program and will be written in degrees here.)

The two-phase jet is directed at angle 90 - A_{noz} (degrees) below the x axis (A_{noz} - 90 above the x-axis). The vector inlet velocity is thus

$$\vec{V}_{in} = \text{POLAR}\ (V_\ell,\ A_{noz} - 90) \qquad \text{(A-3)}$$

The vector blade velocity is

$$\vec{V}_b = \text{POLAR}\ (V_b,\ -90) \qquad \text{(A-4)}$$

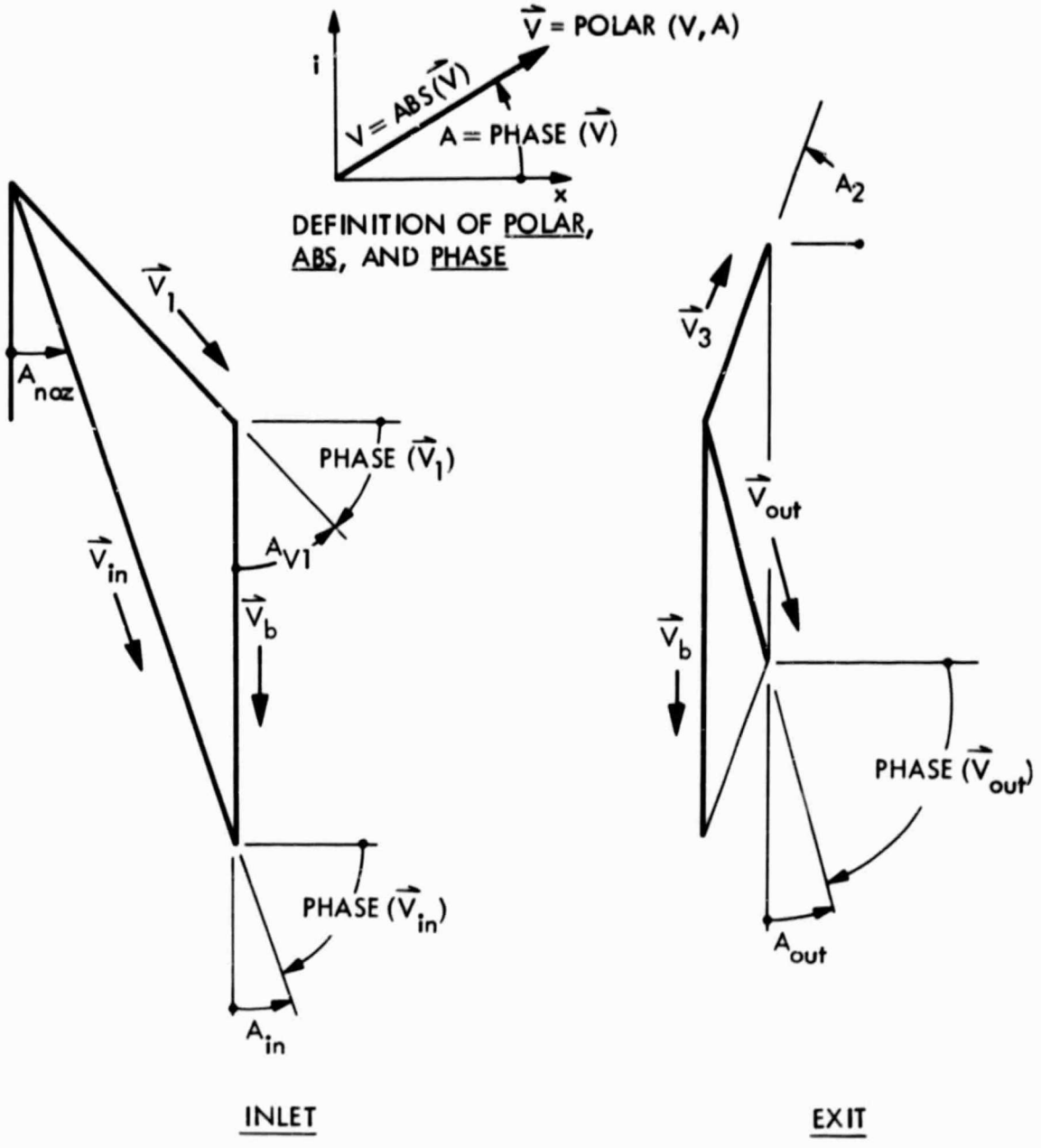

Fig. A-2. Definitions of velocity vectors

The velocity of the incoming liquid relative to the rotor is the difference between the jet and blade velocities:

$$\vec{V}_1 = \vec{V}_{in} - \vec{V}_b \tag{A-5}$$

The magnitude of the relative velocity is

$$V_1 = \text{ABS}\ (\vec{V}_1) \tag{A-6}$$

and the angle of the relative velocity from vertical is

$$A_{V1} = \text{PHASE}\ (\vec{V}_1) + 90 \tag{A-7}$$

noting that PHASE $(\vec{V}_1)$ is negative.

C. Impingement Geometry

Figure A-3 shows the impingement geometry of a flow stream entering at distance Y_{st} above the blade inlet. The flow intersects the blade at angle A_x from the center plane. From Fig. A-3 it can be seen that angle A_x is given by

$$R_1 \sin A_1 = R_1 \sin A_x + (R_1 \cos A_x - R_1 \cos A_1 + Y_{st}) \tan A_{V1} \tag{A-8}$$

Equation (A-8) can be rearranged for iterative solution as follows:

$$A_x = \sin^{-1} (C_1 - \tan A_{V1} \cos A_x) \tag{A-9}$$

where

$$C_1 = \sin A_1 + (\cos A_1 - Y_{st}/R_1) \tan A_{V1} \tag{A-10}$$

The impingment angle of the streamline crossing at Y_{st} is then given by

$$\theta = 90 - A_{V1} - A_x \tag{A-11}$$

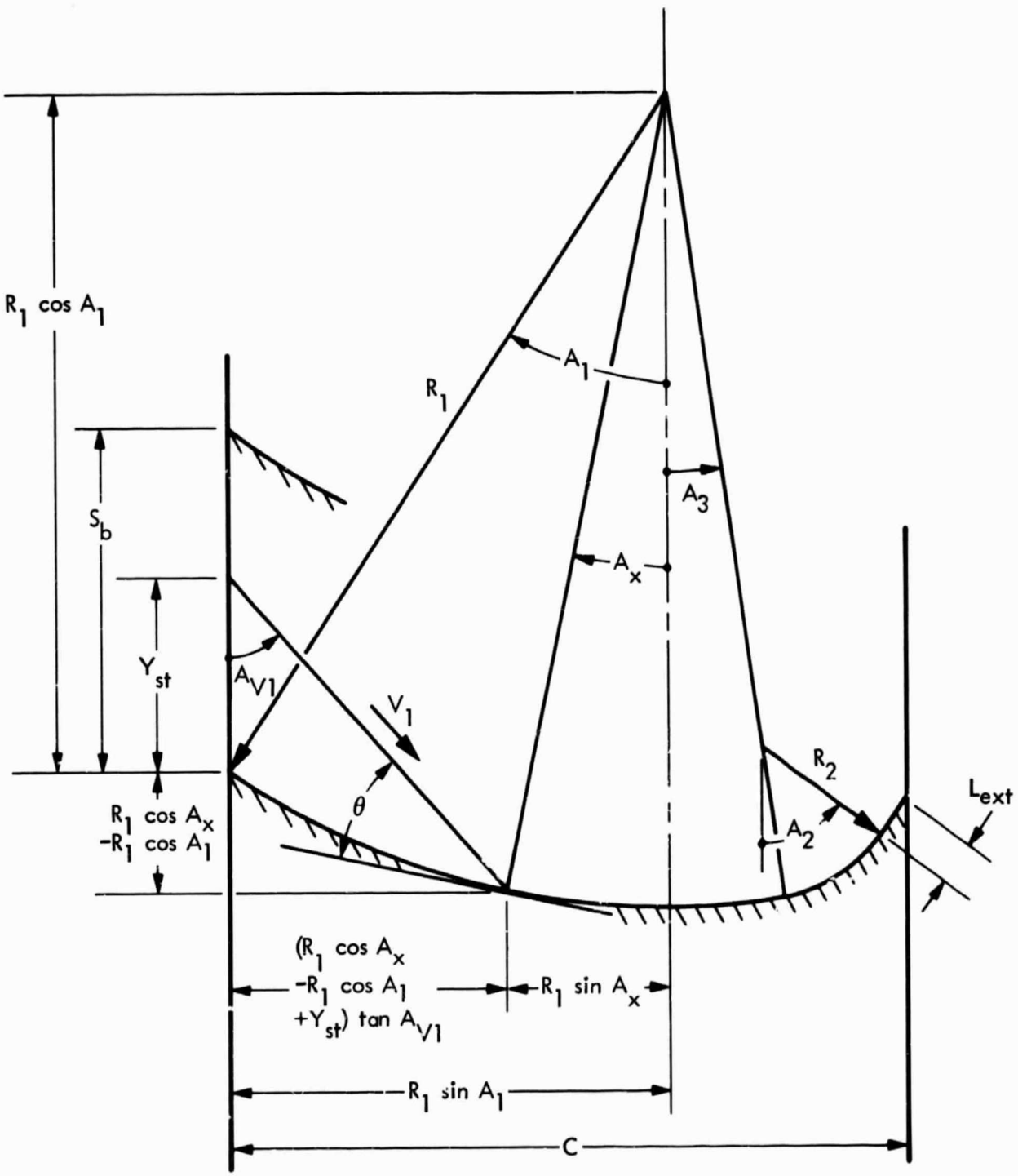

Fig. A-3. Impingement geometry

D. Impact Behavior

When a single liquid jet strikes a surface, both momentum and energy are conserved. The jet splits into two streams that travel away from the point of impact in opposite directions at full velocity (conserving energy) and at differing flow rates (conserving momentum).

When multiple jets or drops strike a surface, only momentum is conserved, because adjacent streams collide with each other and lose kinetic energy through inelastic impact. This effect is familiar from the household water faucets that use screens to divide the flow into multiple streams that dissipate their energy on impact and thus do not splash back.

For two-phase flow striking a turbine blade, the process for the liquid phase can be described as shown in Fig. A-4. The liquid drops strike the blade at angle θ and velocity V_1. The row of drops striking the inlet edge of the blade (idealized as a sheet of liquid) splits into a forward flow and a smaller back flow, both flows traveling at velocity V_1. The second row of drops also splits into a forward flow and a back flow, but the back flow collides with the larger forward flow from the first row of drops and is swept back into the forward direction. Each succeeding row of drops has its back flow swept into the forward direction, and the only back flow from the entire impinging stream is that from the first row of drops.

For a large array of jets, the back flow thus carries a negligible fraction of the total momentum, and the stream leaving the impingement zone has a momentum $\dot{m} V_2$ that is essentially equal to the entire forward component of momentum of the incoming jet $\dot{m} V_1 \cos \theta$. Thus, the equation for liquid velocity recovery in an impinging two-phase jet, considering impact only, is

$$V_2 = V_1 \cos \theta \qquad \text{(A-12)}$$

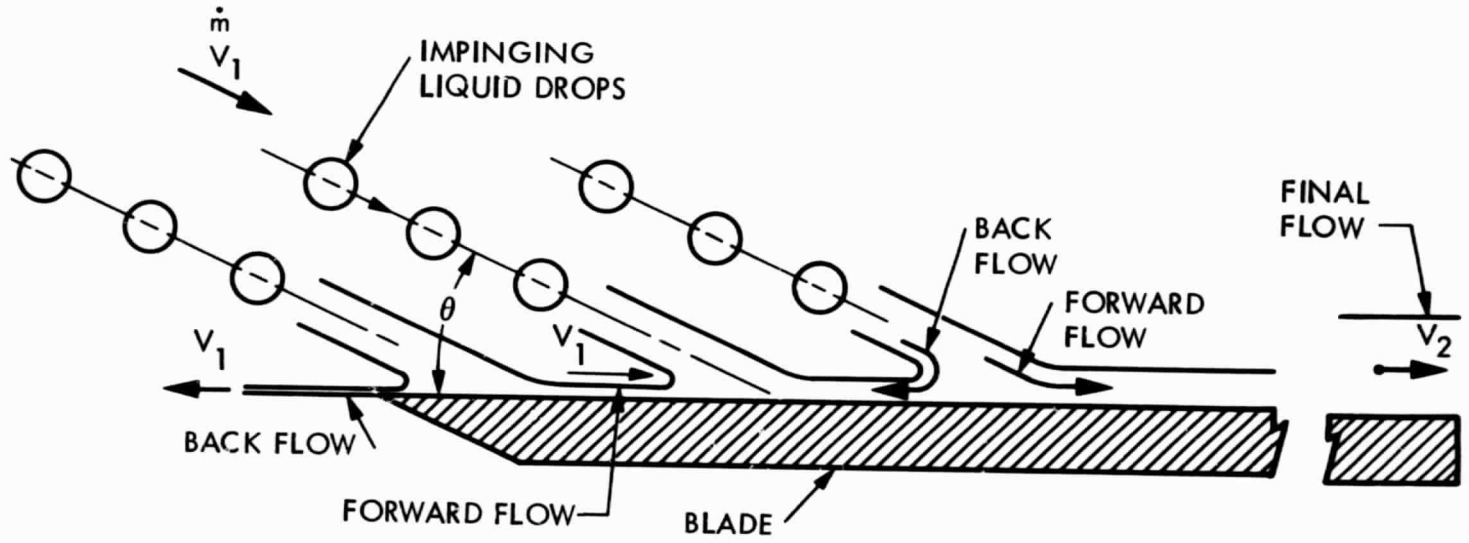

Fig. A-4. Impact behavior

E. Combined Impact and Friction Loss

Figure A-5 shows a short section of blade having width H_n (that dimension perpendicular to the plane of the figure) and area dA on which the flow is impinging at angle θ. The liquid flow rate impinging on the blade section is $d\dot{m}$. The flow rate previously collected is $\dot{m}_0$, entering at velocity V_0.

The flow rate in the film at the midpoint of the blade section is $\dot{m}_m = \dot{m}_0 + \frac{1}{2} d\dot{m}$. If the velocity of the film at the midpoint is V_m, then the film thickness is

$$t_m = \frac{\dot{m}_m}{\rho_\ell H_n V_m} \tag{A-13}$$

It can be assumed that the wall friction is the same as for flow in a rectangular channel of height $2t_m$ and width H_n, because the velocity gradient at the film surface is zero as it would be at the center of a rectangular channel. The hydraulic diameter of a rectangular channel is four times the area divided by the wetted perimeter. Thus the hydraulic diameter of the film is

$$D_h = \frac{4\,(2t_m H_n)}{2\,(2t_m + H_n)} \tag{A-14}$$

Since t_m is much smaller than H_b, the hydraulic diameter is approximately

$$D_h = 4t_m \tag{A-15}$$

The Reynolds number for pipe flow is

$$Re = \frac{\rho_\ell V_\ell D_h}{\mu_\ell} \tag{A-16}$$

where μ_ℓ is the viscosity of the liquid.

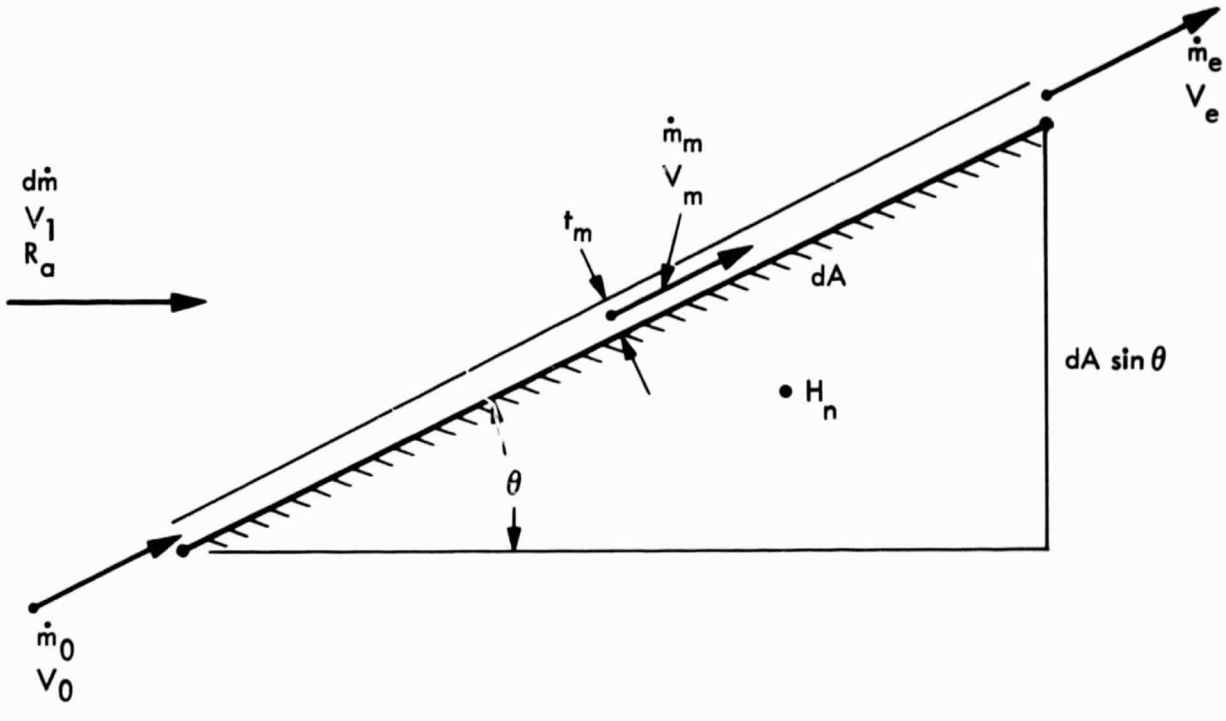

Fig. A-5. Impact and friction on a blade section

Substituting the hydraulic diameter from Eq. (A-15) and the film thickness from Eq. (A-13), the Reynolds number at the midpoint is

$$Re_m = \frac{4\,\dot{m}_m}{H_n\,\mu_\ell} \tag{A-17}$$

For very low Reynolds numbers the flow is laminar and the friction coefficient is given by

$$C_f = \frac{16}{Re} \tag{A-18}$$

For turbulent flow a convenient expression for friction coefficient, valid over a wide range of Reynolds numbers, is the Von Kármán equation:

$$C_f = \frac{1}{[4\,\log_{10}\,(2\,Re\sqrt{C_f}) - 1.6]^2} \tag{A-19}$$

The Reynolds number at which Eqs. (A-18) and (A-19) give the same C_f is 1034.8, and this Reynolds number is used as the dividing line between the two equations.

The retarding force on the liquid film in the blade section of Fig. (A-5) is the product of dynamic pressure, friction coefficient, and wall area. Any mean velocity V_m between inlet velocity V_0 and exit velocity V_e can be used for calculating dynamic pressure since the two velocities approach each other in the limit of small section lengths; exit velocity V_e is used for V here. The friction retarding force can then be written

$$F = \tfrac{1}{2}\,\rho_\ell V_e^2\,C_{fm}\,dA \tag{A-20}$$

where C_{fm} is the friction coefficient at the middle of the section.

The flow area of the two-phase stream impinging on the blade section is dA sin θ. For unit liquid flow area the gas flow area is R_a and the total flow area is $1 + R_a$, where R_a is the gas/liquid area ratio. Hence, the liquid flow rate impinging on the blade section is

$$d\dot{m} = \frac{\rho_\ell V_1 \, dA \sin \theta}{1 + R_a} \tag{A-21}$$

Solving Eq. (A-21) for area dA and substituting into Eq.(A-20), the retarding force on the liquid film in the blade section is

$$F = \frac{V_e^2 C_{fm} (1 + R_a) \, d\dot{m}}{2 V_1 \sin \theta} \tag{A-22}$$

The momentum dM added to the film by the impinging flow $d\dot{m}$, according to Eq.(A-12), is the momentum of the impinging stream times cos θ, or

$$dM = d\dot{m} \, V_1 \cos \theta \tag{A-23}$$

The momentum of the previously-collected flow entering the section along the surface is

$$M_0 = \dot{m}_0 V_0 \tag{A-24}$$

The momentum of the flow leaving the section is

$$M_e = \dot{m}_e V_e \tag{A-25}$$

The exit momentum is equal to the sum of the inlet momentum and the momentum added by the impinging flow, less the friction force:

$$M_e = M_0 + dM - F \tag{A-26}$$

Substituting the friction force F from Eq.(A-22) and the momentums from Eqs. (A-23, A-24, and A-25), the momentum equation becomes

$$\frac{C_{fm}(1 + R_a)}{2 \sin\theta} \frac{d\dot{m}}{\dot{m}_e} \left(\frac{V_e}{V_1}\right)^2 + \frac{V_e}{V_1} - \left(\frac{d\dot{m}}{\dot{m}_e}\right)\left(1 + \frac{\dot{m}_0 V_0}{d\dot{m}\, V_1 \cos\theta}\right) \cos\theta = 0 \qquad \text{(A-27)}$$

Using the quadratic equation to solve for the ratio V_e/V_1, the result is

$$\frac{V_e}{V_1} = \frac{\sin\theta}{C_{fm}(1 + R_a)} \frac{\dot{m}_e}{d\dot{m}} \left[\sqrt{1 + \frac{2\, C_{fm}(1 + R_a)}{\tan\theta}\left(\frac{d\dot{m}}{\dot{m}_e}\right)^2 \left(1 + \frac{\dot{m}_0 V_0}{d\dot{m}\, V_1 \cos\theta}\right)} - 1\right] \qquad \text{(A-28)}$$

This equation gives the liquid film velocity V_e leaving a blade section on which two-phase flow of liquid flow rate $d\dot{m}$ is impinging at angle θ with liquid velocity V_1 and gas/liquid flow area ratio R_a, when the incoming film flow rate is $\dot{m}_0$ at velocity V_0 and the outgoing liquid flow rate is $\dot{m}_e = \dot{m}_0 + d\dot{m}$.

Equation (A-28) reduces to the equation used in past work (Reference 2, Figure 6, substituting $A_2/A_s = \sin\theta$ and $r_v = R_a$ there) for the velocity leaving a flat plate with no initial surface flow. In that case $\dot{m}_0 = 0$, $d\dot{m} = \dot{m}_e$, and the exit velocity is given by

$$\frac{V_e}{V_1} = \frac{\sin\theta}{C_{fm}(1 + R_a)} \left[\sqrt{1 + \frac{2\, C_{fm}(1 + R_a)}{\tan\theta}} - 1\right] \qquad \text{(A-29)}$$

F. Film Friction Loss

Following the impingement zone there is additional blade surface to complete the turning of the flow. The Reynolds number for this "film-flow" zone, from Eq.(A-17), is

$$Re_f = \frac{4\, \dot{m}_b}{H_n \mu_\ell} \qquad \text{(A-30)}$$

where $\dot{m}_b$ is the blade flow. The friction coefficient for this Reynolds number as designated C_{ff}.

Figure A-6 shows the definition of various surface lengths along the blade. The length to the end of the inlet radius of curvature is

$$L_1 = R_1(A_1 + A_3) \tag{A-31}$$

The length of the impingement zone is

$$L_{imp} = R_1(A_1 - A_x) \tag{A-32}$$

where A_x is the angle given by Eq. (A-9) for the last streamline of impinging flow (the flow envelope).

The total surface length is

$$L_{surf} = L_1 + R_2(A_2 - A_3) + L_{ext} \tag{A-33}$$

The length of the film-flow zone is

$$L_{film} = L_{surf} - L_{imp} \tag{A-34}$$

As the film decelerates, the friction force in any length dx is equal to the momentum decrease in that length. The momentum change is

$$\dot{m}_b \, dV = - \tfrac{1}{2} \rho_\ell V^2 C_{ff} H_n \, dx \tag{A-35}$$

Integrating Eq. (A-35) over the length L_{film}, the velocity decreases from V_2 to V_3 according to

$$V_3 = \frac{1}{\frac{1}{V_2} + \frac{\rho_\ell C_{ff} H_n L_{film}}{2\dot{m}_b}} \tag{A-36}$$

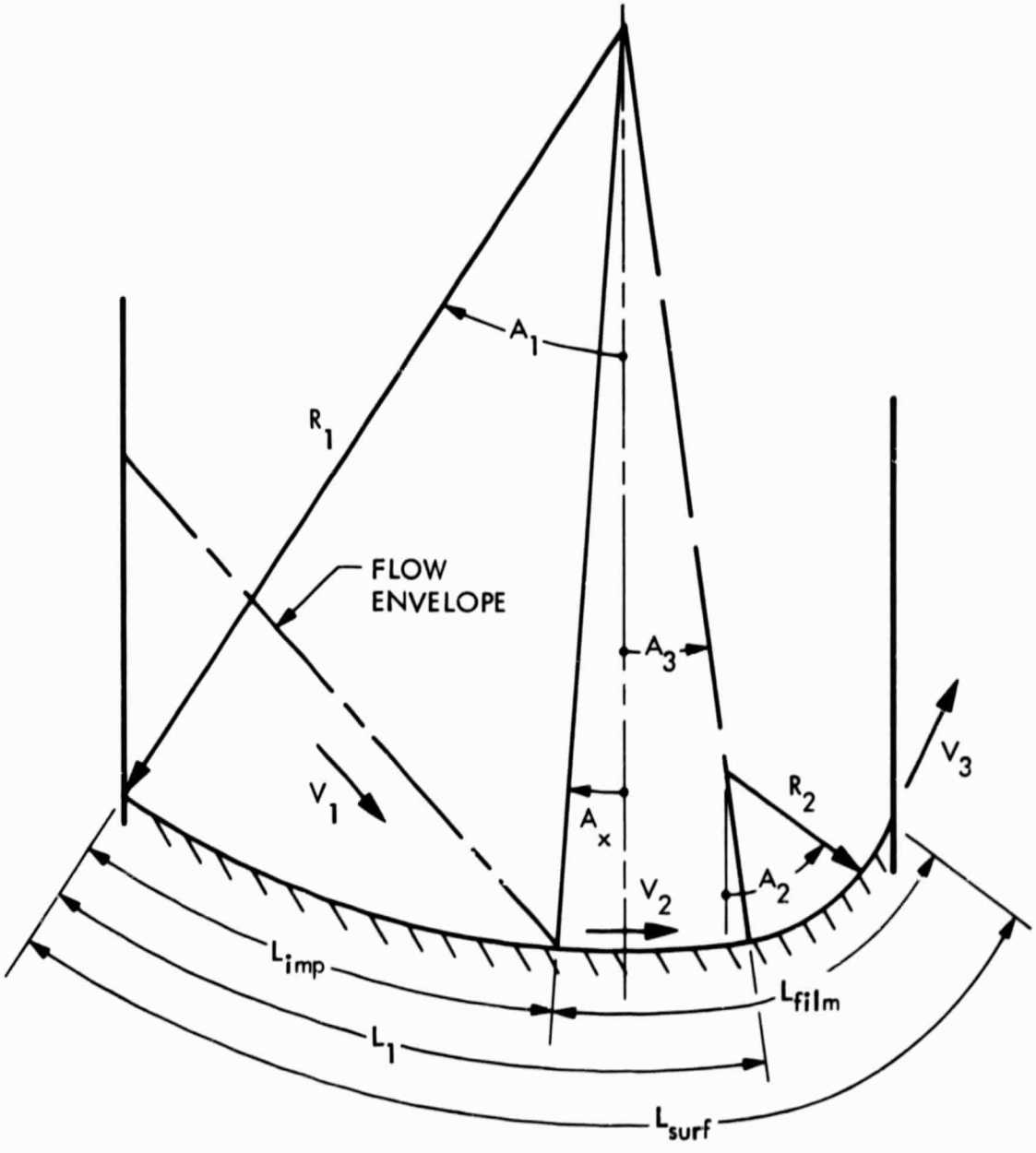

Fig. A-6. Blade lengths

G. Exit Velocity Vectors

The exit velocity vectors are shown in Fig. A-2. The vector exit velocity of the liquid relative to the blade is

$$\vec{V}_3 = \text{POLAR}\ (V_3, A_2) \tag{A-37}$$

Adding the blade speed, the vector absolute exit velocity is

$$\vec{V}_{out} = \vec{V}_3 + \vec{V}_b \tag{A-38}$$

The magnitude of the absolute exit velocity is

$$V_{out} = \text{ABS}\ (\vec{V}_{out}) \tag{A-39}$$

and the angle of the absolute exit flow from vertical is

$$A_{out} = 90 + \text{PHASE}\ (\vec{V}_{out}) \tag{A-40}$$

noting that PHASE $(\vec{V}_{out})$ is negative.

For multistage turbines the exit velocity $\vec{V}_{out}$ becomes the inlet velocity $\vec{V}_{in}$ to the next stage.

H. Windage

Mann and Marston (Ref. 16) present correlations for predicting the windage, or disc friction torque, on a bladed rotor.

The Reynolds number of the flow on a disc of radius R_w rotating at angular velocity ω is defined as

$$Re = \frac{\rho_g \omega R_w^2}{\mu_g} \tag{A-41}$$

where ρ_g is the gas density and μ_g is the gas viscosity.

If the rotor is one of several stages, then separate Reynolds numbers Re_1 and Re_2 are calculated for the upstream and downstream sides of each rotor, using the angular velocities relative to the adjacent rotors or to the atmosphere.

The windage torque depends on the thickness of the rotor, which is equal to the blade chord. From Fig. A-3 it can be seen that the blade chord is given by

$$C = R_1(\sin A_1 + \sin A_3) + R_2(\sin A_2 - \sin A_3) + L_{ext} \cos A_2 \qquad \text{(A-42)}$$

The aspect ratio of the blades is $AR = H_b/C$, where H_b is the blade height (Fig. A-1). Table 3 of Ref. 16 gives moment coefficients C_m as a function of aspect ratio for a Reynolds number of 10^6 and a chord/radius ratio C/R_w of 0.14. These coefficients are denoted C_m^*. The table can be fitted by

$$C_m^* = 0.0067 + 0.007\ AR^{0.6} \qquad \text{(A-43)}$$

The exponent γ of the Reynolds number dependence (C_m proportional to $Re^{-\gamma}$) is given in the same table, and the values can be fitted by

$$\gamma = 0.21 - 0.086\ AR \qquad \text{(A-44)}$$

up to AR = 0.7, beyond which the extrapolation is uncertain and γ is held constant at 0.15.

The moment coefficient C_m for a disc of finite thickness is related to the moment coefficient C_{m_0} for a disc of zero thickness by Eq. (5) of Ref. 16:

$$C_m = C_{m_0}\left(1 + 2.3\ \frac{C}{R_w}\right) \qquad \text{(A-45)}$$

Using the exponent γ to correct from Re = 10^6, and factoring out the thickness/radius ratio $C/R_w = 0.14$ for which Table 3 applies, the zero-thickness moment coefficient as a function of Reynolds number is

$$C_{m_0} = \frac{C_m^* (10^6/Re)^\gamma}{1 + (2.3)(0.14)} \qquad \text{(A-46)}$$

Equation (A-45) can then be applied to find the moment coefficient for the actual thickness/radius ratio C/R_w.

The windage torque M on one side of the disc is found from Eq. (2) of Ref. 16:

$$M = 0.25\, C_m \rho_g \omega^2 R_w^5 \qquad \text{(A-47)}$$

For a single-stage turbine, ω is the rotor speed and M is doubled to give the total windage torque L_w. For multiple stages the relative ω values on each side of the disc are calculated and used with the proper signs to give the windage torques M_1 and M_2 on the inlet and exit sides, respectively (positive for a retarding torque and negative for an accelerating torque).

I. Torque, Power, and Efficiency

The force exerted by the liquid on the blades is equal to the change in liquid momentum in the direction of blade motion. For the angles as defined in Fig. A-2,

$$F_\ell = \dot{m}_\ell \, (V_{in} \cos A_{in} - V_{out} \cos A_{out}) \qquad \text{(A-48)}$$

The torque of the liquid phase is the product of the liquid force and the rotor radius:

$$L_\ell = F_\ell R_b \qquad \text{(A-49)}$$

The gas phase acts independently of the liquid phase, and the gas-phase torque can be calculated by conventional methods. The present program uses the approximation that the gas-phase torque varies linearly from maximum at zero speed to zero at synchronous speed (equal blade and gas speed), with a specified fraction of ideal torque denoted by η_g. The factor η_g is also the gas-phase efficiency at half synchronous speed. This assumption gives the following gas-phase torque equation

$$L_g = 2 \eta_g \dot{m}_g V_g R_b (1 - V_b/V_g) \tag{A-50}$$

The total blade torque is the sum of the liquid and gas torques, $L_b = L_\ell + L_g$, and the net rotor torque is the blade torque less the windage torque, $L_r = L_b - L_w$. The blade output power is

$$P_b = L_b \omega \tag{A-51}$$

and the net rotor power is

$$P_r = L_r \omega \tag{A-52}$$

These powers are summed over each stage for a multistage turbine.

The power in the incoming jet is

$$P_{jet} = \tfrac{1}{2}(\dot{m}_\ell V_\ell^2 + \dot{m}_g V_g^2) \tag{A-53}$$

The blade efficiency is the ratio of blade power to jet power:

$$\eta_b = \frac{P_b}{P_{jet}} \tag{A-54}$$

The rotor efficiency is the ratio of rotor power to jet power:

$$\eta_r = \frac{P_r}{P_{jet}} \tag{A-55}$$

The turbine efficiency is

$$\eta_t = \eta_r \eta_n \tag{A-56}$$

where η_n is the nozzle efficiency.

J. Divergence and Stagnation Losses

Equations (A-1) through (A-56) define what is meant by "theoretical" in this report. The losses modeled are impact and friction for the liquid, the specified torque factor η_g for the gas, and the Ref. 16 moment coefficients for windage.

Two additional losses can be calculated in the program. The effect on torque of the spreading of the liquid leaving the blades is calculated by specifying a mean divergence angle A_{div} for the exit liquid flow. The relative exit velocity V_3 is then corrected to

$$V_3' = V_3 \cos A_{div} \tag{A-57}$$

A fraction f_{stag} of the liquid can be specified as stagnating in the rotor and leaving at rotor speed. The force exerted by this liquid is

$$F_{\ell_{stag}} = \dot{m}_\ell f_{stag} (V_{in} \cos A_{in} - V_b) \tag{A-58}$$

The force of the main flow is $(1 - f_{stag})$ times the force given by Eq. (A-48). The total liquid force is that force plus $F_{\ell_{stag}}$. The result is

$$F_\ell = \dot{m}_\ell \left[V_{in} \cos A_{in} - (1 - f_{stag}) V_{out} \cos A_{out} - f_{stag} V_b \right] \quad \text{(A-59)}$$

The inlet velocity to the next stage is assumed to be the weighted average of the main-flow and stagnated-flow velocities:

$$\vec{V}_{in_{k+1}} = (1 - f_{stag}) \vec{V}_{out_k} + f_{stag} \vec{V}_{b_k} \quad \text{(A-60)}$$

K. Optimization

The program can be used in an optimization search mode. In this mode the program varies the rotor speeds and (optionally) the blade inlet angles for each stage until the maximum rotor efficiency η_r is found.

L. Program Listing

A listing of the computer program follows. The subroutine ZPMIN referenced is a library routine for minimization. Decks of the rotor program including ZPMIN are available from JPL.

The nomenclature used in the program is defined in Table A-1.

```
C  * * * * * * * * * * * * * * * * * * * * * * * * * * * * * * * * * * * *
C
C  * * * * * * * * * * *  TWO-PHASE ROTOR PROGRAM  * * * * * * * * * * *
C
C  * * * * * * * * * * D. G. ELLIOTT, MARCH 31, 1980 * * * * * * * * * *
C
C  * * * * * * * * * *  LAST REVISION NOV. 30, 1981  * * * * * * * * * *
C
C  * * * * * * * * * * * * * * * ASCII FORTRAN * * * * * * * * * * * * * *
C
C  * * * * * * * * * EQUATION NUMBERS REFER TO APPENDIX A  * * * * * * * *
C
C
      PARAMETER MXSTG=2, MXSTEP=20 @ MAX STAGES AND IMPINGEMENT STEPS
      PARAMETER N=MXSTG, N1=2*N, N2=N1*(N1+3), N3=MXSTEP+1
C
      IMPLICIT REAL(L,M)
      REAL A1(N),A2(N),A3(N),R1(N),R2(N),RPM(N),LEXT(N) @ INPUT ARRAYS
      REAL AIN(N),AOUT(N),AV1(N),CFF(N),FL(N),L1(N),LB(N)
      REAL LG(N),LIMP(N),LL(N),LSURF(N),LR(N),LW(N),REF(N)
      REAL V1(N),V2(N),V3(N),VB(N),VIN(N),VOUT(N),WW(N)
      REAL THETA(N3),X(N1),XBEST(N1),WA(N2),EPSX(10)
C
      COMPLEX CV1(N),CV3(N),CVB(N),CVIN(N),CVOUT(N),POLAR
C
      NAMELIST   /IN/WN,HN,HB,ANOZ,RPM,ML,VL,MG,VG,R1,R2,LEXT,A1,A2,A3,
     &              SB,RB,RW,RHOL,RHOG,VISCL,VISCG,NSTG,NSTEP,
     &              ADIV,NR1,ETAG,ETAN,FSTAG,NINPT,NDET,NOPT,NMON
      NAMELIST /OUT1/LB,PB,ETAB,RPM
      NAMELIST /OUT2/LR,PR,ETAR,ETAT
      NAMELIST /OUT3/LL,LG,LW
      NAMELIST /OUT4/A1,VB,VIN,AIN,V1,AV1,V2,L1,LIMP,LSURF,V3,
     &              AOUT,VOUT,WW,RAP1,MB,REF,CFF,TFILM
      NAMELIST /OUT5/CV1,CV3,CVB,CVIN,CVOUT
      NAMELIST /OUT6/M0,MM,ME,REM,CFM,TERM2,V0,VE
C
C  ***** FUNCTIONS *****
C
      XSIN(A)=SIN(PX*A) @ SINE OF ANGLE 'A' IN DEGREES
      XCOS(A)=COS(PX*A) @ COSINE OF ANGLE 'A' IN DEGREES
      XTAN(A)=TAN(PX*A) @ TANGENT OF ANGLE 'A' IN DEGREES
      PHASE(C)=180/PI*ATAN2(AIMAG(C),
     &SIGN(MAX(ABS(REAL(C)),1E-38),REAL(C))) @ANGLE OF C,DEG CCW FROM X-AXIS
      POLAR(AMP,ANG)=CMPLX(AMP*XCOS(ANG),AMP*XSIN(ANG)) @ VECTOR(AMPL,ANGLE)
C
C  ***** CONSTANTS AND DEFAULT INPUTS *****
C
      DATA EPSF/1E-4/,EPSX/10*1E9/,ITMAX/100/ @ CONSTANTS FOR SEARCH ROUTINE
      DATA A1/N*20./,A2/N*60./,NSTEP/20/ @DEFAULT INPUTS
      PI=4.0*ATAN(1.0)
      PX=PI/180
      PXX=180/PI
```

```
C
C ***** INPUT *****
C
10    PRINT *,' ENTER'
      READ (5,IN,ERR=10,END=100)
      IF (NSTEP.GT.MXSTEP) PRINT *,' NSTEP TOO LARGE'
      IF (NSTEP.GT.MXSTEP) GO TO 10
C     DEFINE FILE 6(APRINT,,72) @ TO PRINT NAMELIST ON TERMINAL
C
      IF (NINPT.EQ.1) WRITE (6,IN)
C
C  ***** INITIALIZATION *****
C
      RAP1=WN*HN*RHOL*VL/ML @ GAS/LIQ AREA RATIO + 1 (1)
      MB=ML*SB*XSIN(ANOZ)/WN @ LIQUID FLOW PER BLADE (2)
      DM=MB/NSTEP @ LIQUID FLOW PER BLADE SECTION
      CVIN(1)=POLAR(VL,ANOZ-90) @ VCTR LIQUID VELOCITY FROM NOZZLE (3)
      PJET=0.5*(ML*VL**2 + MG*VG**2) @ JET POWER (53)
C
           DO 20 K=1,NSTG @ SET RPM GUESSES IF SEARCH USED AND SET VB'S
           IF (NOPT.GT.0) RPM(K)=30/(PI*RB)*VL*(NSTG+1-K)/(NSTG+1.)
20         VB(K)=RPM(K)*PI*RB/30 @ INITIAL GUESS AT BLADE SPEEDS
C
      IF (NOPT.EQ.0) GO TO 40 @ NO OPTIMIZATION
C
C ***** OPTIONAL OPTIMIZATION OF RPM(S) AND BLADE INLET ANGLE(S) *****
C
           DO 25 K=1,NSTG @ SEARCH INITIALIZATION
           X(K)=VB(K) @ FIRST NSTG ELEMENTS IN X-VECTOR
25         X(NSTG+K)=A1(K) @ SECOND NSTG ELEMENTS IN X-VECTOR
C
      KGO=0
      NX=NOPT*NSTG @ NUMBER OF VARIABLES IN X-VECTOR
30    CALL ZPMIN(NX,X,Y,EPSX,EPSF,ITMAX,WA,KGO,XBEST,YBEST) @ RESET X
C
      IF (KGO.GT.1) GO TO 90 @ CONVERGED OR ERROR
C
           DO 35 J=1,NSTG @ COPY NEW X-VECTOR TO VARIABLES
           VB(J)=X(J) @ NEW BLADE VELOCITIES
35         A1(J)=X(NSTG+J) @ NEW BLADE ANGLES
C
C  ***** STAGE CALCULATIONS *****
C
40         DO 70 K=1,NSTG
           VIN(K)=ABS(CVIN(K)) @ ABSOLUTE INLET VELOCITY
           AIN(K)=PHASE(CVIN(K)) +90 @ ANGLE OF ABSOLUTE INLET VELOCITY
           CVB(K)=POLAR(VB(K),-90) @ VECTOR BLADE VELOCITY (4)
           WW(K)=VB(K)/RB @ ANGULAR SPEED
           RPM(K)=30*WW(K)/PI @ RPM
C
C  ***** BLADE INLET CONDITIONS *****
C
```

```
          CV1(K)=CVIN(K)-CVB(K) @ VECTOR RELATIVE INLET VELOCITY (5)
          V1(K)=ABS(CV1(K)) @ ABSOLUTE RELATIVE INLET VELOCITY (6)
          AV1(K)=PHASE(CV1(K))+90 @ ANGLE OF RELATIVE INLET VEL (7)
C
C  ***** IMPINGEMENT ANGLES *****
C
          AIO=A1(K)+AV1(K)-90 @ INLET IMPINGEMENT ANGLE (BELOW SURFACE)
          IF (AIO.GE.0) THEN
          IF (NOPT.EQ.0) PRINT *,' IMP',AIO,' BELOW SURFACE IN STG',K
          IF (NOPT.EQ.0) GO TO 10 @ ASK FOR NEW INPUTS
          ETAR=0 @ LOW VALUE TO TELL SEARCH THIS IS A BAD ANGLE
          GO TO 83 @ RETURN TO SEARCH DRIVER
          END IF
C
          NSTEP1=NSTEP+1
          AX1=A1(K) @ INITIAL GUESS AT ANGLE FROM CNTR BACK TO IMP PT
C
               DO 55 J=1,NSTEP1 @ FOR EACH STREAM TUBE PLUS LAST STREAMLINE
               YST=SB*(J-0.5)/NSTEP @ CENTER DISTANCE OF STREAM TUBE
               IF (J.EQ.NSTEP1) YST=SB @ LAST STREAMLINE
               C1=XSIN(A1(K))+(XCOS(A1(K))-YST/R1(K))*XTAN(AV1(K))  @ (10)
C
                    DO 50 JJ=1,100 @ ITERATE EQ.(9) UP TO 100 TIMES FOR AX
                    AX=PXX*ASIN(C1 -XTAN(AV1(K))*XCOS(AX1)) @ NEW AX (9)
                    IF (ABS(AX-AX1).LT.0.01) GO TO 55 @ CONV TO 0.01 DEG
50                  CALL RGLFSI (AX1,AX,JJ) @ CALL REGULA-FALSI ITERATION
C
               PRINT *,' DID NOT CONVERGE ON AX IN STAGE',K @ AFTER 100 TIMES
C
55             THETA(J)=90-AV1(K)-AX @ IMPINGEMENT ANGLE (11)
C
C  **** IMPACT AND FRICTION LOSS *****
C
     V0=0 @ DUMMY VALUE OF INLET VELOCITY FOR FIRST SECTION
C
          DO 60 J=1,NSTEP @ CALCULATE VELOCITY LEAVING EACH SECTION
          M0=(J-1)*DM @ FLOW RATE AT INLET OF SECTION
          MM=M0+DM/2 @ FLOW RATE AT MIDDLE OF SECTION
          ME=J*DM @ FLOW RATE AT END OF SECTION
C
          REM=4*MM/(HN*VISCL) @ REYNOLDS NUMBER (17)
          CALL FRIC(REM,CFM) @ CALCULATE FRICTION COEFFICIENT
C
          Z1=( 1.0 + M0*V0/(DM*V1(K)*XCOS(THETA(J))) ) *(DM/ME)**2
          Z2=XSIN(THETA(J))*ME/(CFM*RAP1*DM)
          TERM2=2*CFM*RAP1*Z1/XTAN(THETA(J)) @ 2ND TERM IN SQRT
          IF (TERM2.LT.1E-12) THEN
          IF (NOPT.EQ.0) PRINT *,' TERM2 TOO SMALL'
          IF (NOPT.EQ.0) GO TO 10 @ ASK FOR NEW INPUTS
          ETAR=0 @ LOW VALUE TO TELL SEARCH THIS IS A BAD ANGLE
          GO TO 83 @ RETURN TO SEARCH DRIVER
          END IF
```

```
C
      VE=V1(K)*Z2*( DSQRT(1.0D0+TERM2) -1.0D0) @ SECTION EXIT VEL (28)
C
      IF (NDET.GE.7) PRINT OUT6
60    VO=VE @ INLET VELOCITY FOR NEXT SECTION
C
   V2(K)=VE @ LIQUID VELOCITY LEAVING IMPINGEMENT ZONE
C
C  ***** FRICTION LOSS IN FILM FLOW ZONE *****
C
      REF(K)=4*MB/(HN*VISCL) @ REYNOLDS NUMBER IN FILM ZONE (30)
      CALL FRIC( REF(K),CFF(K) ) @ FRICTION COEFF IN FILM ZONE
C
      IF(NOPT.EQ.0.AND.-AX.GT.A3(K)) PRINT*,' IMP BEYOND R1, STG',K
      IF (NOPT.GT.1.OR.NR1.EQ.1) A3(K)=-AX @ SET END OF R1 AT LAST STRMLN
      L1(K)=R1(K)*(A1(K)+A3(K))*PX @ LENGTH TO END OF INLET RADIUS (31)
      LIMP(K)=R1(K)*(A1(K)-AX)*PX @ LENGTH TO END OF IMPINGEMENT ZONE (32)
      LSURF(K)=L1(K)+R2(K)*(A2(K)-A3(K))*PX+LEXT(K) @ TTL SURF LENGTH (33)
      LFILM=LSURF(K)-LIMP(K) @ LENGTH OF FILM-FLOW ZONE (34)
C
      V3(K)=1/( 1/V2(K)+0.5*RHOL*CFF(K)*HN*LFILM/MB ) @ REL EXIT VEL (36)
      TFILM=MB/(RHOL*HN*V3(K)) @ FILM THICKNESS LEAVING BLADE
      V3(K)=V3(K)*XCOS(ADIV) @ CORR FOR FLOW DIVERGENCE IF ADIV>0 (57)
C
C  ***** BLADE EXIT CONDITIONS *****
C
      CV3(K)=POLAR(V3(K),A2(K)) @ VCTR RELATIVE EXIT VELOCITY (37)
      CVOUT(K)=CV3(K)+CVB(K) @ VCTR ABSOLUTE EXIT VELOCITY (38)
      VOUT(K)=ABS(CVOUT(K)) @ ABSOLUTE EXIT VELOCITY (39)
      AOUT(K)=90+PHASE(CVOUT(K)) @ ANGLE OF ABSOLUTE EXIT VELOCITY (40)
C
C  ***** WINDAGE TORQUE *****
C
      IF (K.EQ.1) WREL1=VB(K)/RB @ REL INLET ANG VEL FIRST STAGE
      IF (K.GT.1) WREL1=(VB(K)-VB(K-1))/RB @ STAGES AFTER FIRST
      IF (K.LT.NSTG) WREL2=(VB(K)-VB(K+1))/RB @ STAGES BEFORE LAST
      IF (K.EQ.NSTG) WREL2=VB(K)/RB @ REL EXIT ANG VEL LAST STAGE
C
      RE1=RHOG*ABS(WREL1)*RW**2 /VISCG @ REYNOLDS NO., INLET SIDE (41)
      RE2=RHOG*ABS(WREL2)*RW**2 /VISCG @ REYNOLDS NO., EXIT SIDE (41)
      RE1=MAX(RE1,100) @ TO PREVENT OVERFLOW IN CM01 AT ZERO SPEED
      RE2=MAX(RE2,100) @ TO PREVENT OVERFLOW IN CM02 AT ZERO SPEED
      CC=R1(K)*( XSIN(A1(K))+XSIN(A3(K)) ) + R2(K)*( XSIN(A2(K))
     &     - XSIN(A3(K)) ) + LEXT(K)*XCOS(A2(K)) @ BLADE CHORD (42)
      AR=HB/CC @ ASPECT RATIO OF BLADES
      CMSTAR=0.0067+0.007*AR**0.6 @ FIT TO MANN & MARSTON TABLE 3 (43)
      GAMMA=MAX(0.21-0.086*AR,0.15) @FIT TO MANN & MARSTON TABLE 3 (44)
C
      CM01=CMSTAR*((1E6/RE1)**GAMMA)/(1+2.3*0.14) @ AT RE1, CC=0 (46)
      CM02=CMSTAR*((1E6/RE2)**GAMMA)/(1+2.3*0.14) @ AT RE2, CC=0 (46)
      CM1=CM01*(1+2.3*CC/RW) @ BLADED MOMENT COEFF, INLET SIDE (45)
      CM2=CM02*(1+2.3*CC/RW) @ BLADED MOMENT COEFF, EXIT SIDE (45)
```

```
C
          M1=SIGN(1.0,WREL1)*0.25*CM1*RHOG*WREL1**2 *RW**5 @ INLET WINDG (47)
          M2=SIGN(1.0,WREL2)*0.25*CM2*RHOG*WREL2**2 *RW**5 @ EXIT WINDG (47)
C
          LW(K)=M1+M2 @ TOTAL WINDAGE TORQUE ON STAGE K
C
C  ***** LIQUID TORQUE *****
C
          FL(K)=ML*(VIN(K)*XCOS(AIN(K))-(1-FSTAG)*VOUT(K)*XCOS(AOUT(K))
     &           -FSTAG*VB(K)) @ LIQUID FORCE (59)
C
          LL(K)=FL(K)*RB @ LIQUID TORQUE (49)
70        IF (K.LT.NSTG) CVIN(K+1)=(1-FSTAG)*CVOUT(K)
     &     + FSTAG*CVB(K) @ VECTOR ABSOLUTE INLET VEL TO NEXT STAGE (60)
C
C  ***** GAS-PHASE TORQUE *****
C
          DO 75 K=1,NSTG @ CALCULATE GAS-PHASE TORQUE
          IF (K.EQ.1) VGK=VG @ INLET GAS VELOCITY TO FIRST STAGE
          IF (K.GT.1) VGK=VIN(K) @ USE GAS VEL EQUAL LIQ VEL AFTER FIRST STAGE
          LG(K)=2*ETAG*MG*VGK*RB*(1.0-VB(K)/VGK) @ GAS-PHASE TORQUE (50)
          LB(K)=LL(K)+LG(K)  @ NET BLADE TORQUE
75        LR(K)=LB(K)-LW(K) @ NET ROTOR TORQUE
C
C  ***** POWER *****
C
      PB=0.0 @ INITIALIZE TOTAL BLADE POWER TO ZERO
      PR=0.0 @ INITIALIZE TOTAL ROTOR POWER TO ZERO
C
          DO 80 K=1,NSTG @ SUM POWERS OVER STAGES
          PBK=LB(K)*WW(K) @ BLADE POWER IN STAGE K (51)
          PRK=LR(K)*WW(K) @ ROTOR POWER IN STAGE K (52)
          PB=PB+PBK @ TOTAL BLADE POWER
80        PR=PR+PRK @ TOTAL ROTOR POWER
C
C  ***** EFFICIENCY *****
C
      ETAB=PB/PJET @ BLADE EFFICIENCY (54)
      ETAR=PR/PJET @ ROTOR EFFICIENCY (55)
      ETAT=ETAR*ETAN @ TURBINE EFFICIENCY (56)
C
83    IF (NMON.EQ.1) PRINT 85,ETAR
      IF (NMON.EQ.2) PRINT 85,ETAR,(X(J),J=1,NX)
85    FORMAT (F11.8,6(F10.5))
      Y=1-ETAR @ QUANTITY TO BE MINIMIZED IN SEARCH
      IF (NOPT.GT.0) GO TO 30 @ FORM NEW X-VECTOR
C
90    IF (KGO.GT.2) PRINT *,' KGO=',KGO @ ERROR
C
      PRINT OUT1
C
      IF (NDET.GE.2) PRINT OUT2
```

```
      IF (NDET.GE.3) PRINT OUT3
      IF (NDET.GE.4) PRINT OUT4
      IF (NDET.GE.5) PRINT OUT5
C
95    GO TO 10 @ ASK FOR NEW INPUTS
C
100   STOP
C
C  * * * * * * * * * FRICTION COEFFICIENT SUBROUTINE * * * * * * * * *
C
      SUBROUTINE FRIC(RE,CF)
C
      IF (RE.LT.1034.8) CF=16/RE @ LAMINAR FLOW (18)
      IF (RE.LT.1034.8) RETURN @ LAMINAR FLOW
C
      CFGS=0.001525+0.1375/CBRT(RE) @ APPROXIMATE CF
C
           DO 10 KK=1,100
           CF=1/(4*LOG10(2*RE*SQRT(CFGS))-1.6)**2 @ VON KARMAN EQ. (19)
           IF (ABS(CF-CFGS).LT.1E-7) RETURN @ CONVERGED
10         CFGS=CF @ NEXT CF GUESS
C
      PRINT ' DID NOT CONVERGE ON CF'
      RETURN
C
C  * * * * * * * * * REGULA-FALSI ITERATION SUBROUTINE * * * * * * * * *
C
      SUBROUTINE RGLFSI(X1,X2,KOUNT)
C
      IF (KOUNT.EQ.1) SLOPE=0.0 @ SLOPE FOR FIRST PASS
      IF (KOUNT.GT.1) SLOPE=(X2-X2OLD)/(X1-X1OLD) @ SLOPE FROM PREV POINT
C
      X1OLD=X1 @ NEW ABSCISSA BECOMES OLD ABSCISSA
      X2OLD=X2 @ NEW ORDINATE BECOMES OLD ORDINATE
C
      X1=(X2-SLOPE*X1)/(1D0-SLOPE) @ ABSCISSA CROSSING 45-DEG LINE
C
      IF (NMON.EQ.3.AND.KOUNT.EQ.1) PRINT 10
10    FORMAT(/5X,'X1',11X,'X2',9X,'SLOPE'/)
      IF (NMON.EQ.3) PRINT 15,X1,X2,SLOPE
15    FORMAT(3(E13.6))
C
      RETURN
C
      END
```

Table A-1. Rotor model nomenclature

Program	Text	Definition
A1	A_1	blade inlet angle (Fig. A-1)
A2	A_2	blade exit angle (Fig. A-1)
A3	A_3	angle to end of inlet radius (Fig. A-1)
ADIV	A_{div}	average divergence angle of exit flow
AIO		impingement angle at blade inlet
AIN	A_{in}	angle of absolute inlet velocity (Fig. A-2)
ANOZ	A_{noz}	nozzle angle (Fig. A-1)
AOUT	A_{out}	angle of absolute exit velocity (Fig. A-2)
AR	AR	blade aspect ratio H_b/C
AV1	A_{V1}	angle of relative inlet velocity (Figs. A-1, A-2)
AX	A_x	angle to impingement point (Fig. A-3)
AX1		guess at AX
C1	C_1	constant term in Eq. (A-9)
CC	C	blade chord (Fig. A-3)
CF	C_f	friction coefficient
CFF	C_{ff}	friction coefficient in film-flow zone
CFGS		guess at C_f
CFM	C_{fm}	friction coefficient in middle of blade section
CM01	C_{m_0}	windage moment coefficient at zero thickness, inlet side
CM02	C_{m_0}	windage moment coefficient at zero thickness, exit side

Program	Text	Definition
CM1	C_m	windage moment coefficient on inlet side
CM2	C_m	windage moment coefficient on exit side
CMSTAR	C_m^*	windage moment coefficient for $R_e = 10^6$ and $C/R_w = 0.14$
CV1	$\vec{V}_1$	vector relative inlet velocity (Fig. A-2)
CV3	$\vec{V}_3$	vector relative exit velocity (Fig. A-2)
CVB	$\vec{V}_b$	vector blade velocity (Fig. A-2)
CVIN	$\vec{V}_{in}$	vector absolute inlet velocity (Fig. A-2)
CVOUT	$\vec{V}_{out}$	vector absolute exit velocity (Fig. A-2)
DM	$d\dot{m}$	liquid flow rate impinging on blade section (Fig. A-5)
	D_h	hydraulic diameter
EPSF		convergence criterion on dependent variable in search routine
EPSX		convergence criterion on independent variable in search routine
ETAB	η_b	blade efficiency P_b/P_{jet}
ETAG	η_g	gas torque factor (peak gas-phase efficiency)
ETAN	η_n	nozzle efficiency
ETAR	η_r	rotor efficiency P_r/P_{jet}
ETAT	η_t	turbine efficiency $\eta_r\eta_n$
FL	F_ℓ	force of liquid phase
FSTAG	f_{stag}	specified fraction of liquid flow stagnated in the rotor

END

Table A-1 (contd)

Program	Text	Definition
GAMMA	γ	exponent of Reynolds number in moment coefficient
HB	H_b	blade height (Fig. A-1)
HN	H_n	nozzle height (Fig. A-1)
ITMAX		maximum number of iterations in search routine
KGO		flag used to control search routine
L1	L_1	length to end of inlet radius (Fig. A-6)
LB	L_b	blade torque
LEXT	L_{ext}	length of straight extension (Fig. A-1)
LFILM	L_{film}	length of film flow zone (Fig. A-6)
LG	L_g	gas-phase torque
LIMP	L_{imp}	length of impingement zone (Fig. A-6)
LL	L_ℓ	liquid-phase torque
LR	L_r	rotor torque
LSURF	L_{surf}	blade surface length (Fig. A-6)
LW	L_w	windage torque
M0	$\dot{m}_0$	liquid flow rate entering blade section (Fig. A-5)
M1	M_1	windage torque on inlet side
M2	M_2	windage torque on exit side
MB	$\dot{m}_b$	liquid flow rate on each blade
ME	$\dot{m}_e$	liquid flow rate leaving blade section (Fig. A-5)

Table A-1 (contd)

Program	Text	Definition
MG	$\dot{m}_g$	gas flow rate
ML	$\dot{m}_\ell$	liquid flow rate
MM	$\dot{m}_m$	liquid flow rate in middle of blade section (Fig. A-5)
MXSTEP		maximum number of steps for blade impact and friction calculation
NDET		selects level of detail of printout
NINPT		1 for printout of inputs
NMON		1 or 2 for monitoring of search
NOPT		1 for rpm optimization, 2 for rpm and blade angle optimization
NR1		selects matching of blade inlet length to impingement length
NSTEP		number of blade steps for impact and friction calculation
NSTEP1		NSTEP + 1
NSTG		number of rotor stages
NX		number of variables to be optimized
PB		total blade power $L_b\omega$
PBK	P_b	blade power in stage K
PI	π	pi
PJET	P_{jet}	jet power $\frac{1}{2}(\dot{m}_\ell V_\ell^2 + \dot{m}_g V_g^2)$
PR		total rotor power $L_r\omega$
PRK	P_r	rotor power in stage K

Table A-1 (contd)

Program	Text	Definition
PX		$\pi/180$
PXX		$180/\pi$
R1	R_1	blade inlet radius (Fig. A-1)
R2	R_2	blade exit radius (Fig. A-1)
	R_a	gas/liquid flow area ratio
RAP1		$R_a + 1$
RB	R_b	rotor radius at center of nozzle exit (Fig. A-1)
RE	Re	Reynolds number
RE1	Re_1	Reynolds number of windage flow on inlet side
RE2	Re_2	Reynolds number of windage flow on exit side
REF	Re_f	Reynolds number of film flow
REM	Re_m	Reynolds number in middle of blade section
RHOG	ρ_g	gas density
RHOL	ρ_ℓ	liquid density
RPM		rotor speed, revolutions per minute
RW	R_w	outside radius of rotor (Fig. A-1)
SB	S_b	blade spacing (Fig. A-1)
TERM2		second term under the square root in Eq. (A-28)
TFILM		thickness of liquid film leaving blade
	t_m	thickness of liquid film in middle of blade section (Fig. A-5)
THETA	θ	impingement angle (Fig. A-3)

Table A-1 (contd)

Program	Text	Definition
V0	V_0	velocity of liquid film entering blade section (Fig. A-5)
V1	V_1	relative inlet velocity (Fig. A-1)
V2	V_2	velocity of liquid leaving impingement zone (Fig. A-1)
V3	V_3	relative exit velocity (Fig. A-1)
VB	V_b	blade velocity (Fig. A-1)
VE	V_e	velocity of liquid leaving blade section (Fig. A-5)
VG	V_g	gas velocity
VGK		inlet gas velocity to stage K
VIN	V_{in}	absolute inlet velocity (Fig. A-2)
	V_m	velocity of liquid in middle of blade section (Fig. A-5)
VISCG	μ_g	gas viscosity
VISCL	μ_ℓ	liquid viscosity
VL	V_ℓ	liquid velocity
VOUT	V_{out}	absolute exit velocity (Fig. A-2)
WA		array used in search routine
WN	W_n	nozzle width (Fig. A-1)
WREL1		speed of rotor relative to previous stage or atmosphere
WREL2		speed of rotor relative to next stage or atmosphere

Table A-1 (contd)

Program	Text	Definition
WW	ω	rotor speed, radians per second
X		array used in search routine
XBEST		array used in search routine
Y		$1 - \eta_r$, quantity minimized in optimization search
YBEST		variable used in search
YST	Y_{st}	distance of streamline from blade inlet (Fig. A-3)
Z1		product of last two factors in second term under the square root in Eq. (A-28)
Z2		product of first two factors in Eq. (A-28)

APPENDIX B.

SEPARATOR TURBINE MODEL

Figure B-1 shows the geometry of the separator turbine. The two-phase flow enters at radius R_{noz} and angle A_{noz}. The liquid has flow rate $\dot{m}_\ell$ and velocity V_ℓ. The gas has flow rate $\dot{m}_g$ and velocity V_g. The jet power is

$$P_{jet} = \tfrac{1}{2}\left(\dot{m}_\ell V_\ell^2 + \dot{m}_g V_g^2\right) \tag{B-1}$$

A. Separator Flow

The liquid impinges on the inside wall of a rotary separator turning at angular velocity ω_1. The liquid forms a spinning liquid layer of radius R_{sep}. The liquid is removed from the separator by a liquid turbine with one or more U-tube scoops turning at angular velocity ω_2. The speed of the liquid layer is

$$V_{sep} = \omega_1 R_{sep} \tag{B-2}$$

B. Liquid Turbine Flow

The speed of the scoop is

$$V_{turb} = \omega_2 R_{sep} \tag{B-3}$$

The relative velocity of the liquid entering the scoop is

$$V_{rel} = V_{sep} - V_{turb} \tag{B-4}$$

The relative velocity of the liquid leaving the scoop is V_{rel_2}. The scoop efficiency can be defined as the square of the ratio of exit velocity to inlet velocity. Thus, if the scoop efficiency η_{scoop} is given, the relative exit velocity is

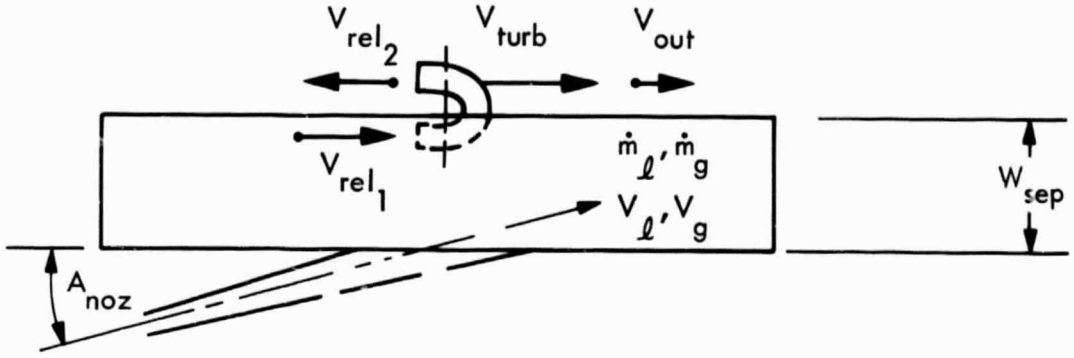

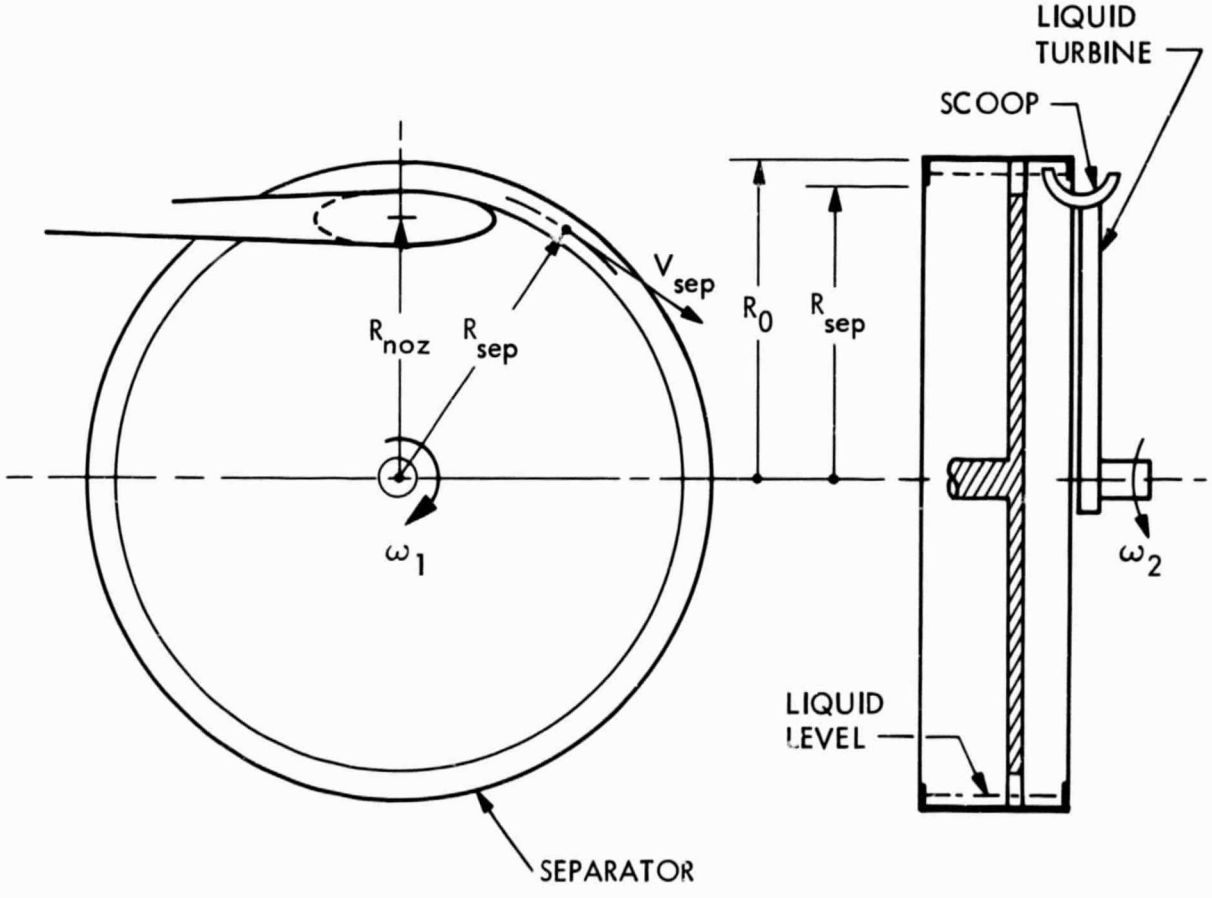

Fig. B-1. Separator turbine

$$V_{rel_2} = V_{rel_1}\sqrt{\eta_{scoop}} \tag{B-5}$$

The absolute forward exit velocity of the liquid leaving the liquid turbine is

$$V_{out} = V_{turb} - V_{rel_2} \tag{B-6}$$

The required inlet area of the scoop, or scoops, is

$$A_{scoop} = \frac{\dot{m}_\ell}{V_{rel_1}\rho_\ell} \tag{B-7}$$

where ρ_ℓ is the liquid density.

The torque exerted on the scoop by external liquid drag can be expressed as a drag coefficient C_d times the product of frontal area and dynamic pressure:

$$L_{ext} = \tfrac{1}{2}C_d A_{scoop}\rho_\ell V^2_{rel_1} R_{sep} \tag{B-8}$$

C. Liquid Torque

The angular momentum of the liquid leaving the nozzle is

$$M_1 = \dot{m}_\ell V_\ell R_{noz} \cos A_{noz} \tag{B-9}$$

The angular momentum of the liquid leaving the separator is

$$M_2 = \dot{m}_\ell V_{sep} R_{sep} \tag{B-10}$$

The angular momentum of the liquid leaving the liquid turbine is

$$M_3 = \dot{m}_\ell V_{out} R_{sep} \tag{B-11}$$

The separator torque due to the liquid flow is equal to the change in angular momentum of the liquid in the separator minus the external drag of the liquid turbine:

$$L_{liq} = M_1 - M_2 - L_{ext} \tag{B-12}$$

The liquid turbine torque is equal to the change in angular momentum of the liquid in the turbine, plus the external drag.

$$L_{turb} = M_2 - M_3 + L_{ext} \tag{B-13}$$

D. Windage

The windage torque of the separator can be calculated from the windage torque formulas of Appendix A, evaluated for a nonbladed disc. The Reynolds number is

$$Re = \frac{\rho_g \omega_1 R_0}{\mu_g} \tag{B-14}$$

where ρ_g is the gas density, R_o is the separator outside radius, and μ_g is the gas viscosity.

With no blades, the aspect ratio AR is zero. From Eq. (A-43), the moment coefficient for a disc of thickness/radius ratio = 0.14 at Re = 10^6 is $C_m^* = 0.0067$. From Eq. (A-44), the exponent of the Reynolds number dependence is $\gamma = 0.21$. From Eq. (A-46), the moment coefficient for a thin disc at Re = 10^6 is then

$$C_{m_0} = \frac{0.0067\ (10^6/Re)^{0.21}}{1 + (2.3)(0.14)} \tag{B-15}$$

From Eq. (A-45), the moment coefficient for the separator of width W_{sep} is

$$C_{m_0} = C_{m_0}\left(1 + 2.3\frac{W_{sep}}{R_0}\right) \tag{B-16}$$

From Eq. (A-47), the windage torque is

$$L_w = \tfrac{1}{2} C_m \rho_g \omega_1^2 R_0^5 \tag{B-17}$$

The windage torque of the liquid turbine is ignored because of its lower speed.

E. Gas Torque

The efficiency of power recovery from the gas phase at optimum gas turbine speed is a specified constant, η_g. If a separate gas turbine is used that runs at optimum speed, then the gas turbine power is

$$P_{gt} = \tfrac{1}{2}\eta_g \dot{m}_g V_g^2 \tag{B-18}$$

If the gas turbine consists of impulse blading attached to the separator at radius R_{gt}, then η_g is the fraction of ideal gas torque at the separator speed. The gas torque is thus

$$L_{gas} = 2\eta_g \dot{m}_g V_g R_{gt} \cos A_{noz}\left(1 - \frac{\omega_1}{\omega_{sync}}\right) \tag{B-19}$$

where ω_{sync} is the synchronous speed at which the blade speed equals the circumferential component of gas velocity.

$$\omega_{sync} = \frac{V_g \cos A_{noz}}{R_{gt}} \tag{B-20}$$

F. Power and Efficiency

The total separator torque is

$$L_{sep} = L_{liq} + L_{gas} - L_w \tag{B-21}$$

where L_{gas} is zero if a separate gas turbine is used.

In the calculation presented in Fig. 43, L_{gas} was zero and the separator speed was adjusted to make L_{sep} zero (free-spinning separator).

The separator power output is

$$P_{sep} = L_{sep}\,\omega_1 \tag{B-22}$$

The liquid turbine power output is

$$P_{turb} = L_{turb}\,\omega_2 \tag{B-23}$$

The total power output is

$$P_{tot} = P_{sep} + P_{turb} + P_{gt} \tag{B-24}$$

where P_{gt} is zero if the gas turbine is attached to the separator.

The rotor efficiency is

$$\eta_r = \frac{P_{tot}}{P_{jet}} \tag{B-25}$$

and the turbine efficiency is

$$\eta_t = \eta_r \eta_n \tag{B-26}$$

where η_n is the nozzle efficiency.

REFERENCES

1. Elliott, D. G., "Investigation of a Gas-Driven Jet Pump for Rocket Engines," Liquid Rockets and Propellants, Vol. 2, Academic Press, Inc., New York, 1960, pp. 497 - 541.

2. Elliott, D. G., L. G. Hays, D. J. Cerini, and D. W. Bogdanoff, "Investigation of a Liquid-Metal Magnetohydrodynamic Power System," 5th Intersociety Energy Conversion Engineering Conference, American Nuclear Society, La Grange, Illinois, 1970, pp. 2-64 - 2-73.

3. Elliott, D. G., and L. G. Hays, "Two-Phase Turbine Engines," 11th Intersociety Energy Conversion Engineering Conference, American Institute of Chemical Engineers, New York, 1976, pp. 222 - 228.

4. Austin, A. L., G. H. Higgins, and J. H. Howard, The Total Flow Concept for Recovery of Energy from Geothermal Hot Brine Deposits, Report No. UCRL-51366, Lawrence Livermore Laboratory, Livermore, California, April 3, 1973.

5. Austin, A. L., and A. W. Lundberg, The LLL Geothermal Energy Program, A Status Report on the Development of the Total-Flow Concept, Report No. UCRL-50046-77, Lawrence Livermore Laboratory, Livermore, Calif., October 2, 1978.

6. Cerini, D. J., "A Two-Phase Rotary Separator Demonstration System for Geothermal Energy Conversion," 12th Intersociety Energy Conversion Engineering Conference, American Nuclear Society, La Grange, Illinois, 1977, pp. 884 - 892.

7. Hays, L., and D. J. Cerini, "Progress Report on Rotary Separator Turbine Demonstration Program," Proceedings of the Third Annual Geothermal Conference and Workshop, Electric Power Research Institute, Palo Alto, Calif., October 1979, pp. 3-1 - 3-3.

8. Steidel, R. F., Jr., H. Weiss, and J. E. Flower, Performance Characteristics of the Lysholm Engine as Tested for Geothermal Power Applications in the Imperial Valley, Report No. UCRL-80151, Lawrence Livermore Laboratory, Livermore, Calif., August 22, 1977.

9. McKay, R. A., Helical Screw Expander Evaluation Project, Final Report, Jet Propulsion Laboratory, Pasadena, Calif. (to be published).

10. Elliott, D. G., and E. Weinberg, Acceleration of Liquids in Two-Phase Nozzles, Technical Report 32-987, Jet Propulsion Laboratory, Pasadena, Calif., July 1, 1968.

11. Alger, T. W., The Performance of Two-Phase Nozzles for Total Flow Geothermal Impulse Turbines, Report No. UCRL-76417, Lawrence Livermore Laboratory, Livermore, Calif., May 28, 1975.

12. Alger, T. W.,, Droplet Phase Characteristics in Liquid-Dominated Steam-Water Nozzle Flow, Report No. UCRL-52534, Lawrence Livermore Laboratory, Livermore, Calif., August 9, 1978.

13. Comfort, W. J., III, The Design and Evaluation of a Two-Phase Turbine for Low Quality Steam-Water Mixtures, Report No. UCRL-52281, Lawrence Livermore Laboratory, Livermore, Calif., May 16, 1977.

14. Comfort, W. J., III, "Performance of a Total Flow Impulse Turbine for Geothermal Applications," 12th Intersociety Energy Conversion Engineering Conference, American Nuclear Society, La Grange, Illinois, 1977, pp. 893-898.

15. Baker, D. W. C., K. H. Jolliffe, and D. Pearson, "The Resistance of Materials to Impact Erosion Damage," Philosophical Transactions of the Royal Society, Series A, 260, 1966.

16. Mann, R. ., and C. H. Marston, "Friction Drag on Bladed Disks in Housings", Journal of Basic Engineering, December, 1961, pp. 719 - 723.